Modelling Schottky Contact Surface Plasmon Nano-detector

by

Naema Mahmoud Othman

Thesis submitted to the
Faculty of Graduate and Postdoctoral Studies
In partial fulfillment of the requirements
For the M.Sc. degree in
Physics

Ottawa-Carleton Institute of Physics
Faculty of Science
University of Ottawa

Abstract

Over the past few years, surface plasmon photodetectors have been of renewed interest. This is due to their unique double functionality of combining an SPP waveguide structure with a photodetection structure. This thesis investigates the performance of a Schottky nano-photodetector integrated into a finite width metal stripe which is covered by air on top and supported by silicon at the bottom, supporting the propagation of bound SPP modes. Properties of surface plasmons, including the sub-wavelength confinement, were exploited to increase the efficiency of the detector. The detector performance was explored via applying end-fire coupling to the fundamental supported mode, then the results were used to calculate the devices responsivity, dark current, minimum detectable power, and photocurrent for various metal lengths. End fire coupling to a Schottky mode supported by a nano-structured metal was done for what is believed to be the first time.

Acknowledgements

Above all, I thank God for giving me the health, strength and patience in finishing this work despite many challenges.

I thank my husband, Bahi, for all the sacrifices he made for me. This work could not have been completed without your assistance and understanding, and I am very grateful to you for all your help.

I would love to thank my sweet daughter, Haneen, for bringing joy and happiness to me on stressful days.

I would like to thank my Father, Mother, sisters and brothers, whom I have not seen for 5 years, but I know they think of me everyday.

I also thank the Physics department for being like a family to me and providing all the resources I needed.

I thank all the people who contributed to this interesting area of research by sharing their knowledge.

I would like to thank my Supervisor, Pierre Berini, for allowing me to explore this area of research, and for his patience and support throughout my studies.

Finally, I thank my friends, Kholoud, Abeer, Madiha, Sally, Khawla, as well as my colleagues, Saba and Alex who did not hesitate to offer any help.

Contents

List of Tables

List of Figures

Chapter 1

Introduction and Literature Survey

1.1 Introduction

1.1.1 Thesis Motivation

Focusing light into small volumes beyond the diffraction limit has presented a major challenge in optics; however, the technique of exploiting the wavelength scalability of surface plasmon polaritons has been proven successful in overcoming this hurdle [1]. Nano-scale confinement of light or nano focusing has introduced a great enhancement of the electric field strength through coupling light to plasma oscillations at a metallic-dielectric surface (surface plasmon polaritons) [1] [2]. Although this optical confinement always results in energy dissipation, careful design of a plasmonic waveguide can lead to a great enhancement of light intensity and in turn, overpower the total power dissipation [1].

The SPP waves supported by metal/dielectric interfaces are known to exhibit larger in-plane wave vectors than light with the same frequency; thus, they are expected to focus light to length scales smaller than the diffraction limit of light in the surrounding dielectric [3]. The large field enhancement achieved in small volumes contributed to the development of many applications such as data storage, control of optical signals, nano-lithography, addressing signal quantum emitters, and sensing [3].

Waveguide structures with finite-width metallic stripes were shown to be of strong interest for several applications. Thus, various waveguide structures with symmetric and asymmetric finite-width metal stripes were theoretically studied and experimentally tested to date.

Surface plasmon photodetectors are of continuous interest due to their vigorous applications such as bio-chemical sensing, low-noise high speed detection, single plasmon detection, photovoltaic solar energy conversion, and near- and mid-infrared imaging [4]. Their unique properties, including resonating on tiny metallic structures and sub-wavelength confinement, and their waveguide-photodetector structure combination were the main reasons behind their broad diversity.

Many photodetector designs with different detection mechanisms have been reported to date. Some are based on absorption in organics and semiconductors with EHP (electron-hole-pair creation) detection mechanism or absorption in metals with IPE (internal photo-emission) which is the one studied in this research, while others use thermal and photo-assisted transport as well as tunnelling as the detection mechanisms [4]. A waveguide based Schottky photodetector can be designed by integrating a Schottky detector with a waveguide that supports the propagation of $SPPs$. The device exploits IPE as the detection mechanism via absorption in the metal to enable infrared detection below the bandgap of Si [4].

The internal photoemission detection mechanism is not very efficient, making the task of finding a photodetector design that produces usable responsivity at room temperature a priority in achieving success.

The implementation of SPP waveguides as SPP detectors has garnered significant attraction in recent years. That is because they can be integrated with other plasmonic or photonic waveguide structures [5]. Such devices were further enhanced with the use of silicon as the semiconductor medium. The technological importance of silicon and the applications like high speed photodetection at telecom wavelengths or clock distribution in CMOS electronics are the main motivating factors for the design of SPP waveguide detectors that are based on Si [4]. This material has also been used in other SPP waveguide structures.

Another attribute that underlines the importance of waveguide based detectors is the localized guided fields which can be further enhanced with the use of nano-structured waveguides. It holds promise for the design of new photodetectors with increased absorptance, enhanced detection processes, and shrunken waveguide dimensions [4]. Moreover, strongly confined $SPPs$ that are supported by a thin metal film could enhance phonon-

assisted transitions in Si. For example, it was reported that the wavevector of strongly confined $SPPs$ on a metal film could be large enough to support phonons in supplying the momentum needed for indirect transitions in Si [6].

1.1.2 Thesis Objectives

There are two main objectives behind this thesis work. The first goal is to examine the performance of this detector at the nano-scale level. Designing a nano-structured Schottky photodetector that operates with IPE and is capable of producing enhanced photoresponse, large photocurrent to dark current ratio, and increased minimum detectable power was the intention . The second goal was to test the ability of this detector as a near field scanner by calculating the amount of overlap that can be gained when overlapping the mode supported by this detector with a mode of an optical fiber.

A nano-structured waveguide based photodetector was studied theoretically in this research. Up to $12mA/W$ of responsivity is predicted for p-type Si at the wavelength $1550nm$. This was mainly because of an increase in the device quantum efficiency after multiple hot carrier reflections inside the metal film.

1.1.3 Thesis Organization

This document is set up as follows:

In Chapter 1, there is an introduction to the research topic, a literature review on SPP waveguides as well as modes, the use of nano-structured waveguides as well as detectors, and a review of Schottky contact photodetectors having different designs and composed of different materials.

Chapter 2 outlines the theory of infinite and finite SPP waveguides and introduces the asymmetric SPP modes in nanometer scale. The distribution, evolution, and phase of the fundamental mode as_b^0 supported by a gold stripe of varied thickness t and width w is discussed. The effective index of the highly confined asymmetric SPP modes is given along with the mode power attenuation as a function of change in stripe's thickness and width at two optical wavelengths.

Chapter 3 illustrates the trade-off of the coupling efficiency between the fundamental asymmetric SPP mode and a tapered PM optical fiber mode as a function of change in stripe's width and thickness at two optical wavelengths. Coupling between two identical photodetectors is presented in this chapter along with maps of overlap between a fundamental asymmetric Schottky mode and an optical fiber mode for two waveguide structures having different stripe thicknesses t and widths w and at two operating optical wavelengths.

In Chapter 4, the device's photocurrent, dark current, and responsivity, and minimum detectable power are calculated and results are discussed at two optical wavelengths.

Chapter 5 gathers conclusions, thesis contributions, and future work suggestions.

1.2 Background

1.2.1 Surface Plasmon Polaritons

SPP are known as quantized hybrid modes of light field and a collective electron oscillation that can be resonantly excited at a metal/dielectric interface [2]. At optical wavelengths, metals tend to have a negative dielectric constant which enables them to be modelled as a cold plasma or free electron gas [5, 7, 8]. In addition, the interface between two different materials having opposite signs of real part of permittivity supports the propagation of electromagnetic surface modes when proper excitation for the metal is made at optical operating wavelengths [5, 7, 9, 10]. Thus, when a metal is deposited on top of a dielectric at optical wavelengths, the interface between the metal and the dielectric supports the propagation of plasmon-polariton modes which are TM modes and propagate as electromagnetic fields in the metal [10]. Those modes are usually referred to as SPP_s [8, 11]. The name surface plasmon polaritons SPP_s is given to those modes because they are essentially light waves which are trapped on the metal's surface due to their interaction with the metal's free electrons [9, 7]. The electrons in the metal move to create electric field polarization, distributing positive and negative charges in a row, thus the word Polariton means a wave of polarization [7].

$SPPs$ are useful for guiding and channelling of optical radiation in integrated optical

devices [12]. Furthermore, they can be used to test the quality of a metal surface since they propagate at the metal/dielectric interface and are sensitive to surface roughness or irregularity [13]. The SPP intensity is maximum at the interface and decays exponentially within about $100nm$ in both perpendicular directions [2, 14].

The SPP modes which propagate along a metal-air interface have a finite propagation length depending on the Ohmic losses of the metal [15]. Their propagation length is of the order of $10\mu m$ for noble metals with visible or near-infrared light wavelengths [2]. The losses are due to radiation losses and sample defects like surface roughness. They can also be measured by the frequency dependent imaginary part of the dielectric constant[14]. Researchers have used some other methods to control the propagation of SPP as in [16].

1.2.2 Maxwell's Equations and $SPPs$

The following equations are Maxwell equations in MKS units [17]:

$$\begin{aligned} \nabla \times H &= J + \frac{\partial D}{\partial t} \quad ; \qquad \nabla \cdot B = 0 \\ \nabla \times E &= \frac{-\partial B}{\partial t} \quad ; \qquad \nabla \cdot D = \rho \end{aligned} \tag{1.1}$$

where ∇ is the vector operator in Cartesian coordinates which is defined as:

$$\nabla = a_x \frac{\partial}{\partial x} + a_y \frac{\partial}{\partial y} + a_z \frac{\partial}{\partial z} \tag{1.2}$$

A_x, a_y, and a_z represent the unit vectors that point in the directions x,y, and z respectively.

When solving Maxwell's equations with fields propagating along the interface and decaying exponentially as they move away from the interface, we get [4]:

$$H_x(y,z,t) = \begin{cases} \exp(-\gamma_d y + i\beta z - i\omega t & y > 0 \\ \exp(\gamma_m y + i\beta z - i\omega t & y < 0 \end{cases} \{ \tag{1.3}$$

where: H_x represents the x-component of the SPP magnetic field.

and,

$$\gamma_{d,m} = \frac{\omega}{c}\sqrt{\frac{-\varepsilon_{d,m}^2}{\varepsilon_d + \varepsilon_m}} \tag{1.4}$$

also,

$$\beta = \frac{\omega}{c}\sqrt{\frac{\varepsilon_d \varepsilon_m}{\varepsilon_d + \varepsilon_m}} \tag{1.5}$$

$\omega = 2\pi f$ which denotes the angular frequency of light, $i = \sqrt{-1}$.

The imaginary part of epsilon which represents the loss has been ignored. Equation 1.5 is known as the dispersion relation where: ε_d is the relative permittivity of the dielectric and ε_m is the relative permittivity of the metal.

The effective index of the SPP mode can be obtained from the following equation using the propagation constant β.

$$n_{eff} = \frac{c\beta}{\omega} \tag{1.6}$$

where: c represents the speed of light.

This effective index is larger than the dielectric's refractive index. Thus, the $SPPs$ wavelength is short compared to the plane waves in the dielectric, leading SPP modes to not couple to free space plane waves. A prism or a grating will be needed to make the coupling between the SPP waveguide mode and the free space plane waves to be effective. This is known as the phase matching process.

1.2.3 SPP waveguide structures and modes

Surface plasmon modes can be guided by a single interface, symmetric structures or asymmetric structures with the waveguide core preferably being a noble metal. Investigating the behaviour of SPP modes, guided by asymmetric structures, with stripe's thickness and width as well as testing the performance of the asymmetrically cladded Schottky photo-detectors with the use of the electrical properties of Schottky contact is discussed briefly in this thesis.

Single interface surface-plasmon waveguide structure is the simplest of all in which the SPP modes propagate along the interface between a metal and a semi-infinite dielectric [18]. The metal acquires a negative real part of permittivity at optical frequencies allowing for only one bound SPP mode along the interface [5], [9], [11], [13]. This mode, which is transverse magnetic(TM) and non-radiative, propagates at any angle in the plane of the interface [13]. The mode fields are confined in the direction perpendicular to the interface (y-direction); they reach maxima at the interface and decay into both media [13]. The confinement of the SPP mode occurs because the metal and the dielectric have opposite signs of real part of permittivity at optical wavelengths. The structure is sketched on figure 1.1 along with the transverse component of the electric field (E_y). From figure 1.1, it is clearly seen that the field penetrate more in the dielectric than the metal [13]. A study of the dispersion characteristics of surface plasmons that are supported by a single interface SPP waveguide is included in appendix A.

The electric field of the SPP modes has only one component perpendicular to the direction of wave propagation as well as the planar interface and it has an exponentially decaying distribution [5], [9], [10], [11]. When the waveguide structure is composed of a metal stripe as the core and two dielectrics as the claddings, the transverse field will be decaying exponentially in both the structure's upper and lower clads [8, 9]. Surface plasmons, which are exponentially bound within an optical wavelength of the surface, are mostly used for surface sensing.

The electric field component normal to the surface is out-of-phase by $\pi/2$ in regard to the electric field component that is parallel to the surface and gets its maximum at the interface [10]. Moreover, this electric field transverse component maintains a constant distribution as the wave propagates along the boundary because metals can satisfy the

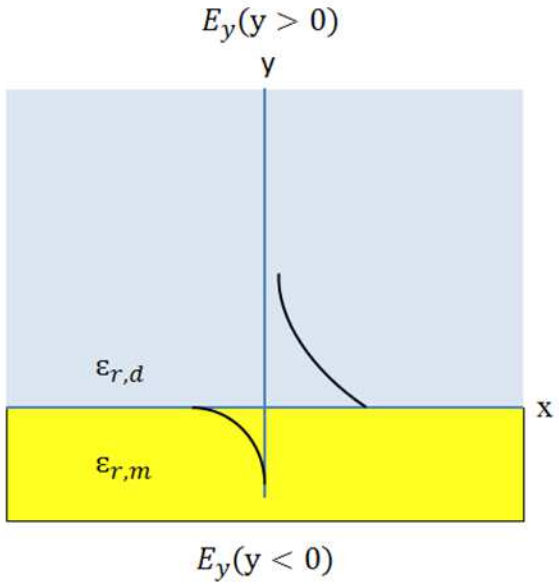

Figure 1.1: Transverse electric field component is sketched on a single-interface SPP waveguide where $\varepsilon_(r, d)$ and $\varepsilon_(r, m)$ represent the relative permittivity of the dielectric and metal, respectively.

self-consistency condition for the waveguide modes having only one-single interface [10]. This is mainly due to the negative real permittivity the metals have in the visible regime [9], [10]. However, when crossing the interface, the transverse electric field component changes sign and gets a phase shift of π. This phase-shift is 2π when crossing the interface twice which satisfies the self-consistency condition [10]. The self-consistency condition states that the round-trip phase of the mode is a multiple of 2π; this includes the phase-of-propagation and of reflection [10]. Figure 1.2 shows a schematic of this phase-shift.

For an asymmetric finite-width waveguide structure, different claddings above and under the metal, the bound modes supported are known as as_b modes. The electric field for those modes has an asymmetric spatial distribution across the metal where fields penetrate. Thus, the supported bound SPP modes are called lossy modes as they propagate along the metal/dielectric interface with absorption, they allow total absorption of the coupled input optical energy, leading to having a number of hot excited carriers in the metal which then can be collected as photocurrent after crossing the metal-semiconductor interface [5, 13, 19].

The first order short-range surface plasmon polariton mode is termed as_b^0 because the field is highly confined beneath the stripe [19]. The letters a and s refer to the asymmetric

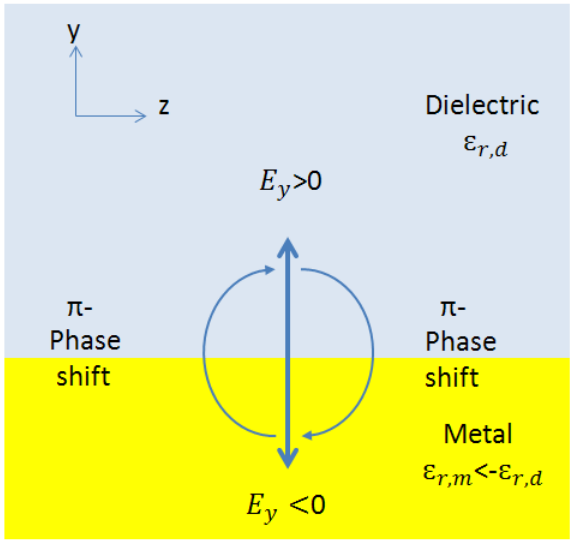

Figure 1.2: A schematic explains the self-consistency relation which is satisfied if the electromagnetic wave crosses the interface twice. The SPP waveguide mode can exist in this single interface waveguide structure because of the metal's negative real permittivity in the visible regime. E_y represents the transverse electric field component.

or symmetric nature of the main electric field component along the y and x confinement directions, respectively, while the superscript refers to the mode order or the number of times the fields switch sign in and along the width of the metal, and the subscript to the bound nature of the mode [5, 12]. If there is a sufficient asymmetry in the index of refraction between the top and bottom clads around the metal, then the bound modes of such waveguide can be cut off [20]. In other words, the cut-off thickness increases as the asymmetry in the index of refraction between the two clads increases [5]. Modes which are vertically asymmetric are not cut-off at low thicknesses and their fields expand in the cladding of higher refractive index more than the cladding of lower refractive index [5, 20].

Symmetric structures where the metal is cladded by the same material are very well known to support the propagation of symmetric bound SPP modes. Those modes which are long ranging surface plasmon polariton modes ($LRSPP$) are usually referred to as ss_b modes and they are propagating along the metal with low loss as well as low confinement. Figure 1.3a illustrates the difference between the symmetric bound ss_b and the asymmetric bound as_b SPP modes.

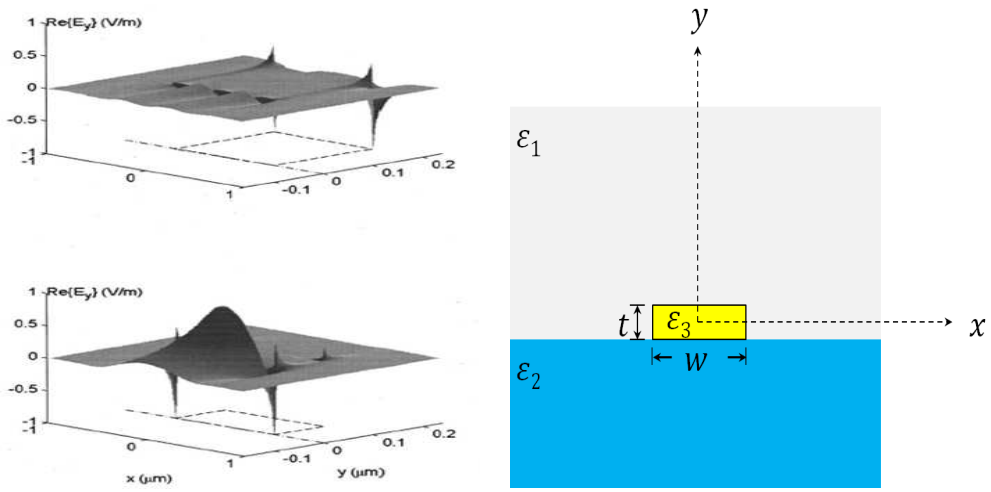

(a) (b)

Figure 1.3: (a)The spatial distribution of the real part of Ey for symmetric bound modes (ss_b) (on top) and asymmetric bound modes (as_b) (at the bottom). Figure is adopted from Ref [11]. (b) An Au stripe of thickness t and width w supported by a silicon substrate and covered by air.

A finite width metal stripe cladded asymmetrically by air on top and silicon on bottom, which constructs a Schottky contact photodetector and supports the propagation of short-range surface plasmon polariton modes is discussed briefly in this thesis and the waveguiding properties are described at infrared wavelengths, specifically at ($1310nm$ and $1550nm$).

The asymmetric bound SPP modes, which are symmetric along the width of the stripe but asymmetric along its thickness, have high confinement and high propagation loss [5, 11, 18]. This loss occurs due to damping of radiation in metal [13] . On the other hand, the finite width metal stripe which is cladded symmetrically was shown to guide bound SPP modes which are symmetric along the stripe width as well as the thickness and operate in the long range SPP with lower confinement and lower loss [5, 9, 18, 19].

1.2.4 Nano-Structures and SPP Enhancement

Nanostructuring the metal used in the waveguide can enhance the local field intensity and enhance some optical processes including Raman scattering (RS), Fluorescence, and Absorption [10]. For example, Raman scattering, which is 14 orders of magnitude weaker than fluorescence, can be enhanced to distinguish materials at the single-molecule level

[10]. The process is known as SERS in which the metal nanostructures enhance the local field by focusing light down to the nanoscale [10]. In addition, they provide double enhancement as they capture the Raman scattering photons and send them back to the detector [10]. This double enhancement occur because the Raman scattering photon and the incident photon have almost identical energies [10]. As a result of this double enhancement, the Raman scattering intensity can get increased by about the square of the near field intensity enhancement [10]. Due to the strong optical field enhancement for surface plasmons at the metal interface, weak optical processes like second harmonic generation can get enhanced as well.

The wide range of applications SPP_s have, including sensing, waveguiding, and integrated optics, are due to the $SPPs$ high field intensity at the interface, high surface and bulk sensitivities, and potential in sub-wavelength field confinement [5]. Nano-structuring the waveguide structure can help in reducing the group velocity and the SPP wavelength, thus field intensities can get enhanced as the light is concentrated at the subwavelength scale [10]. As a result, enhancement of weak optical processes, like second-harmonic generation can be observed from roughened metal surfaces [10]. Similarly, surface enhanced Raman scattering ($SERS$) at the single molecule level can be observed from arbitrary bumpy surfaces [10]. Surface plasmon nanophotonics have several applications including optical trapping and manipulation, surface enhanced Raman spectroscopy, surface plasmon resonant sensing, enhanced fluorescence, and near-field imaging [10].

1.2.5 Enhancement Of Schottky Photodetectors

Schottky barrier detectors can suffer from the low optical absorption of the incident optical power in the metal [5]. This is mainly due to the high reflectivity of metals at most frequencies and to the use of thin metals in Schottky waveguide structures [5]. For instance, thin Si-integrated-photodetectors allow for fast response but suffer from poor optical absorption and thus, decreased sensitivity [21]. This is because the indirect band gap in Silicon allow for lower absorption coefficients unlike $III-V$ materials [21]. Researchers focused on increasing the optical absorptance factor of metals through various schemes, including enhancement through the excitation of $SPPs$ or through the use of a resonant cavity [5]. For example, a greater absorptance and so responsivity were achieved using $SPPs$ on grating-coupled detectors. The responsivity increased by 30 percent when using a corrugated grating to excite $SPPs$ along the air/Au interface in

an $Au/p-InP$ Schottky detector [13].

Hole coupled photodetectors have also shown an improvement in the performance of the devices [13]. They introduced an improved signal-to-noise ratio through the grating/slit combination [13]. For instance, Ishi *et al.*[22] used a Schottky detector on n-doped Si in which the metal used for the Schottky contact was a circular corrugated grating surrounding a tiny hole [13]. The small detection volume of the structure allowed for high speed operation and better responsivity which was mainly due to the (grating/hole) combination's ability to collect light [13].

It was also observed that enhancing the resonating electric fields in photodetectors integrating nanoparticles led to enhancing the absorption in Silicon as well as enhancing the photocurrent [13].

1.3 Alternate Surface Plasmon Schottky Photodetector Technologies

Since the discovery of surface plasmons in 1957 by Rufus Ritchie, many photodetector structures that benefit from surface plasmon phenomena have been designed and tested by researchers over the world. Below is a review of different photodetector designs which involve SPP_s and appear to be very promising.

1.3.1 Hole-Coupled Photodetectors

In the middle of the seventeenth century, Grimaldi described the diffraction from a circular aperture for what is believed to be the first time [23]. The invention has been of a major importance in the field of classical optics [23]. After that, and even though the size of the aperture was very big compared to the wavelength of light, researchers spent centuries to investigate such apertures as it was very difficult to characterize their optics experimentally [23]. As interest raised on the use of subwavelength holes and longer wavelengths of the electromagnetic spectrum in the twentieth century, Beth studied and described the diffraction from a subwavelength hole located in a perfectly conducting metal screen of zero thickness [23]. He predicted that transmission of light through the

hole would be very weak [23]. However, Light transmission through the hole can be many orders of magnitude greater than what is expected from Beth's theory if arrays of subwavelength holes were placed in the metal film [23]. This enhancement is mainly caused by the combination of the subwavelength holes and surface waves as the arrays of holes couple the incident light to $SPPs$ [13, 23]. Then, the $SPPs$ can propagate through the inside walls of the holes and radiate on the other side of the structure [13]. Using such arrays in detector structures gives rise to polarization and wavelength selectivity as well as responsivity enhancement [24, 25].

If the metal film was structured into corrugations around the holes, the collection or transmission of light through those holes could get significantly increased [13, 23]. In other words, those periodic structures perform the role of optical antennas as they couple the incident light into SPs at a given λ. And, as a result, the electromagnetic fields become more concentrated above the holes leading to a very well defined spectrum and high transmission efficiencies [23].

Another Schottky detector on n-doped Si was proposed by Ishi,[22] which uses a metal formed into a circular corrugated grating surrounding a small aperture. This photodetector benefit from surface plasmons to enhance its speed at near infrared wavelengths. The device as shown on figure 1.4 is composed of three parts as follows:

1- The anode which acts as a SP antenna and as a Schottky electrode.

2-A small n-doped Si mesa structure that is located below the aperture.

3-The cathode

.

The scale of the tiny aperture measures the Schottky junction area.

The incident light excites SPs on the circular corrugated metal causing a great enhancement to the optical near-field on the other side of the aperture. Then, within the small Si mesa, carriers can be generated by the enhanced optical near-field. At this point, detection was reported.

Due to the small detection volume and through the enhancement of the optical near-

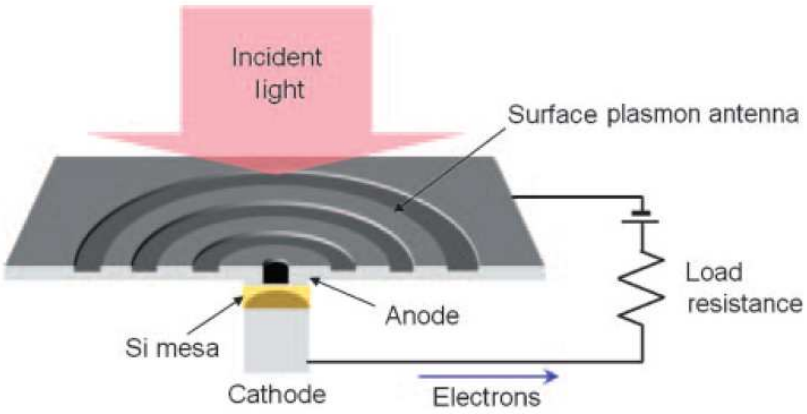

Figure 1.4: A schema showing a cross sectional view of the nano-photodiode. Adopted from [22].

field by SP resonance, this nano-photodiode added the advantage of high-speed response. Also, it was concluded that the enhancement of the optical near-field via SP resonance led to an enhancement in the photogeneration of carriers. This was clearly observed by the increase in photocurrent by several tenfold compared to that without a surface plasmon antenna. The great collection of light through the (grating/aperture) combination contributed to having a good responsivity of the device.

Yu. [26] proposed a midinfrared photodetector that uses a grating/slit combination to increase the signal-to-noise ratio. This is done due to the light being confined into a small active detection area. This photodetector consists of a slit in a metal slab that is filled with absorptive semiconductor material and surrounded by a linear grating structure. The whole structure is then placed on a substrate of an insulating oxide. The metal regions concentrate the light into the slit, whose width is much smaller than the operating wavelength, and work as electrical contacts. Figure 1.5 shows the device geometry. The device has a limited number of grooves but an infinitely long metal slab.

1.3.2 Photo-detectors Integrating Nano-particles

Integrating metal nano-particles into a detector structure is done by depositing them on the surface though which light enters the device [13].Metal nano-particles with different shapes, sizes, and dielectric environments surrounding them could support resonances if

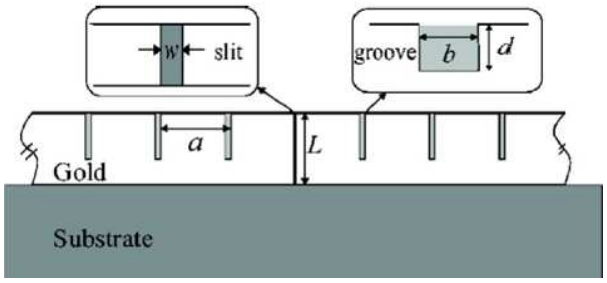

Figure 1.5: A geometry of a midinfrared photodetector. An infinitely long gold slab consists of a narrow slit of width (w) and equally distant grooves having an equal width (b). The whole structure is supported by an insulating oxide substrate. Figure is shown as published in[26].

they are illuminated by light [13, 27]. Those resonances vary depending on the wavelength of light and the different shapes, sizes, compositions, and dielectric environments of particles [13]. The resonance arises when a metal nano-particle is illuminated by light and the conduction electrons oscillate in coherence with the oscillating electric field [27]. Due to resonance, the electric field in the dielectric environment around the nano-particle gets enhanced and this enhancement can be shown in the particle's scattering spectra [13]. If the particle was a small spherical metallic nano-particle, which has a diameter much smaller than wavelength of light, as seen in Figure 1.6, then the resonance is called dipole particle plasmon resonance where the electron cloud becomes shifted relative to the nuclei and then attracted to the nuclei by the Coulomb attraction force [27]. As the diameter of the particle increases, the wavelength of the dipole plasmon resonance shifts towards the red [13].

Detectors operating at photon energies or those based on a thin absorption layer can suffer from low absorptance [13]. However, when incorporating metal nano-spheres, those detectors can have an improved absorptance due to the increased absorption on resonance within the detection volume and to the increased scattering into the detection volume [13]. For example, stuart et al. [28] demonstrated enhanced absorption in a thin film photodetector due to the use of a metal island film. By using different annealing and deposition conditions, they were able to control the size of the nano-particles. A significant increase in photocurrent was achieved as the size of silver-island particles, which are fabricated onto SOI photodetector, increases. This photocurrent enhancement was due to the radiative coupling to the waveguide modes supported by the SOI photodetector, which also led to change in resonance, and to the increased scattering of nano-particles with large sizes. Stuart and his colleagues deposited a mono-layer of metal nano-particles

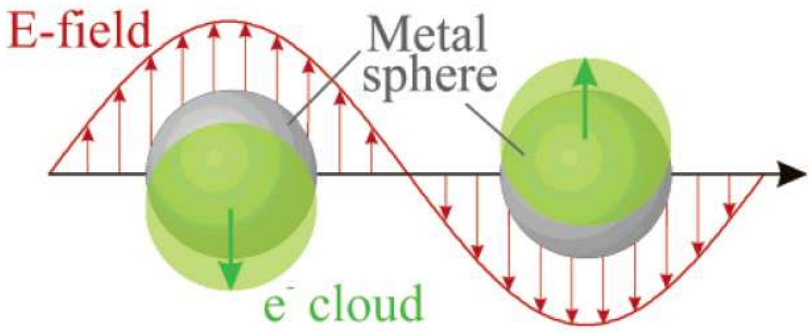

Figure 1.6: Schematic of electron charge cloud's displacement and oscillation relative to the nuclei. The dipolar plasmon resonance has opposite charge densities in the direction of polarization of the illuminating electric field. Figure is adopted from [27].

onto the device and used a thin lithium fluoride layer to separate the nano-particles layer from the detector layer. When light was incident on the device, the localized plasmon resonances in the nano-particles layer got excited causing dipole oscillations in the particles which in turn couple radiatively to the waveguide modes supported by the thin silicon layer. The plasmon resonances allow for radiative scattering and enhanced absorption near resonance.

A photodetector in which a thin Ag film was deposited and then annealed to produce islandization allows for a great enhancement in photocurrent compared to a detector without islands [13]. This significant enhancement in photocurrent was due to the huge scattering of the islands and to the enhanced absorption in the silicon area close to the nano-particles [13]. The structure produces nearly hemispherical particles that are not identical in shapes and sizes but of a regular average size [13].

1.3.3 Grating Coupled Photodetectors

Gratings are used in Schottky detector structures to couple the incident light to SPPs which can lead to enhanced photocurrent, greater absorptance, and increased responsivity of detectors [13, 29].

For example, and as shown in Figure 1.7, a grating was used to enhance the quantum efficiency of Au-InP internal photoemission detector through the coupling of TM-

polarized incident light into the $SPPs$ propagating along the air/Au interface [30]. The coupling to $SPPs$ occurs through phase matching between the incident light and the grating periods [5]. Different groove depths and film thicknesses were used to get the optimum coupling [30]. A significant increase in responsivity was observed due to most of the coupled incident energy gets absorbed in the metal at the resonance coupling angles with the maximum measured responsivity being at the peak of the m=1 resonance and is 30 times the responsivity of the same detector without the grating [30].

Another grating coupled detector was designed by *Jestle et al.*[29] in which a thin-

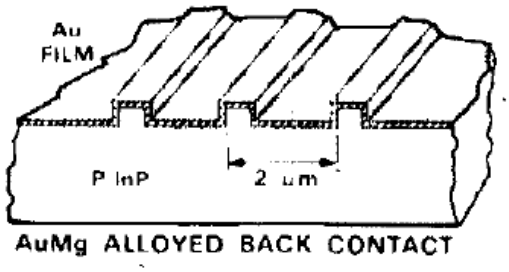

Figure 1.7: A grating with a period of $2\mu m$, film thickness $30nm$, and depth $50nm$ is fabricated on heavily doped $p-Inp$. Structure is shown as published in [30].

tunnel SiO_2 was cladded from below by a sinusoidal corrugated grating of P-Si and from top by Al layer. Exciting $SPPs$ on the metal surface(along the Al/air interface) by a p-polarized light leads to coupling and enhanced photocurrent of the device which is a polarization dependant photocurrent. Light must have the appropriate polarization for the SPP modes to get excited. The metal layer was chosen to be thin ($\sim 35nm$) in order to allow the excited SPP modes and the light that was not used to excite them to penetrate through and emerge into the $p-s$i layer where the modes generate $EHPs$ (detection mechanism) if their energy is larger than the band gap energy of the semiconductor. By the use of two detectors with one grating oriented at 45^0 from the other grating, Jestle, and his research group were able to explicitly determine the polarization angle of a linearly-polarized normally-incident light. This technique allowed for construction of integrated devices without using rotational parts or filters. Other experiments on grating coupled SPP detectors indicated the increased accuracy of the devices when using four and six detectors with different orientations of the gratings. The performance

of grating coupled photodetectors is greatly affected by the wavelength of the incident light, angle of incidence, and polarization [13].

1.3.4 Detectors based on Optical Antennas

Optical antennas are known as passive structures which produce oscillating near-fields at specific locations along its geometry by capturing part of an incident optical wave [4]. By combining this function with photodetection, integrated nano scale detectors with compelling characteristics can be produced as in [31, 32]. This is because antennas produce electric near-fields of much greater intensity than the incident electric fields, thus they allow for small detection volumes which enables the production of fast devices with good signal to noise characteristics as for the grating coupled nanohole detector shown on figure 1.4 as well as polarisation resolved spectroscopic nano-detectors [4].The antenna performance depends on the propagation characteristics of SPP_s which are excited on metal nanowires at optical wavelengths, thus the antenna performance is not only affected by the nanowire length but also by the nanowire cross section and the dielectric environment [4].

It is noteworthy that several factors must be considered when integrating the photodetection capabilities with an antenna. They include the effects of the detection medium on the antenna performance, location and strength of the near fields, and means for collecting the photocurrent [4].

Many photodetector designs that are based on optical antennas have been presented to date. The following is a detector that is based on a planar optical antenna:

In [33], Liang Tang *et al.* experimentally demonstrated a deeply subwavelength MSM photodetector which holds promise for high-speed detection at the nanoscale. Due to the antenna resonance, there was an enhancement by a factor of 20 in the relative photocurrent in the detector which could improve the sensitivity of subwavelength semiconductor photodetectors. The device consists of an Au dipole antenna aligned parallel to the y axis and two line electrodes are aligned parallel to the x axis [33, 4]. Under the two line electrodes and in the gap region between the two dipole arms, a Crystalline germanium nanowire lies [33]. Its high responsivity at near infrared wavelengths as well as its

compatibility with standard silicon technology were the main reasons behind its use as the active material of the detector [33]. A sketch of the device as well as cross sectional sketches through the contact and antenna regions are shown on figure 1.8 for a,b,and c, respectively. The dipole antenna collects light from a large area and concentrate it to the gap subwavelength region for photodetection within the germanium Ge volume while the two line electrodes collect the photocurrent generating therein without changing the antenna characteristics[4].

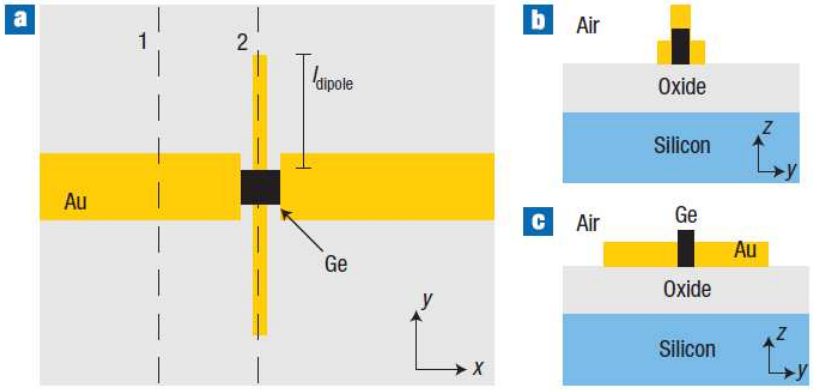

Figure 1.8: (a) Sketch of an Au dipole antenna parallel to the y axis with a germanium nanowire running through its gap and two line electrodes parallel to the x axis. (b) and (c) are cross sections through dashed lines 1 and 2, respectively, of panel (a). Adopted from [33].

1.3.5 Waveguide Based Photodetectors

Waveguide based photodetectors can be either based on slab waveguides Insulator-Metal-Insulator (IMI) and Metal-Insulator-Metal (MIM) or based on Symmetric and Asymmetric finite width metal stripes [13]. Both (IMI) and (MIM) can support supermodes which form due to the coupling of single-interface $SPPs$, which are supported on both upper and lower (metal/insulator) interfaces, through the thin intervening layer [4]. The supported supermodes are known to be of low loss and weak confinement in symmetric (IMI) structures, however, they are of high loss and strong confinement in (MIM) structures.

A waveguide based Schottky photodetector is basically a combination of a waveguide

structure and a semicoductor [13]. It can have two detection barriers if both insulator regions in (IMI) structures are replaced with semiconductors as in [19], and only one detection barrier if only one insulator region is replaced with a semiconductor as in [34]. Such detectors have been designed and tested using a metal stripe that is either deposited on p-Si and on n-Si and covered by air (asymmetric cladding configuration) as in [18, 34, 35, 36, 37] or buried in p-Si and n-Si (symmetric cladding configuration) as in [38, 39].

An example of MIMdetectors is a device designed by Pieter Nuetens *et al.* in 2009 [40]. The device combines a MIMwaveguide structure with a nano-slit metal-semiconductor-metal (MSM) photodetector and is formed on $GaAs$. The $SPPs$ propagating in the MIM structure can be electrically characterized and detected using the MSM photodetector. The structure is illustrated in Figure 1.9 in which two gold layers are surrounding a layer of HSQ (hydrogen silsesquioxane). A $300nm$ slit in the top gold layer is used to excite $SPPs$ propagating in the MIM and another $300nm$ wide slit in the bottom gold layer is used to excite the localized plasmonic modes in the slit. coupled SPP modes are then radiated towards the $GaAs$ for detection via the creation of $EHPs$ [13].

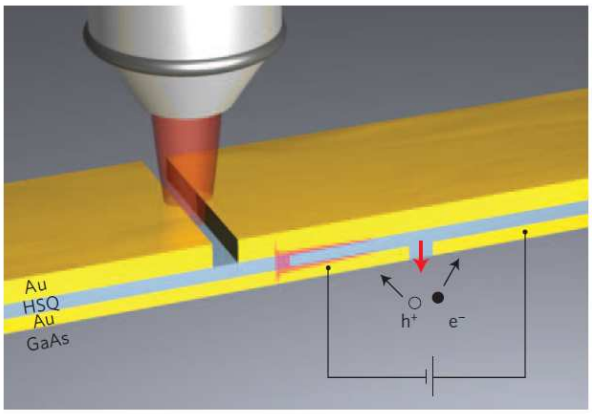

Figure 1.9: Schematic showing the MIM-MSM photodetector. Adopted from [40].

In 2006, another MIM detector which uses materials other than Si was designed by Ditlbacher *et al.* [41]. It is composed of a *pn* junction fabricated from organic polymers on a silver film and covered by another silver film forming a MIM like photodetector which is then attached to coupling slits through a single interface SPP waveguide.

The whole structure is supported with a glass substrate that is covered with a $100nm$ thick silver film. This film has slits that form local SPP sources after irradiating the structure with light. The film, which also serves as a single interface SPP waveguide, serves simultaneously as a bridge to connect the slits to the plasmon diode and as the bottom electrode of the organic plasmon diode. The slits are being illuminated with TM-polarized light at perpendicular incidence from the top which results in $SPPs$ being excited at the silver/air interface. $SPPs$ then propagate along the waveguide until they reach the detector section which is located $50\mu m$ away from the slits. After that, the $SPPs$ incident from the silver waveguide excite the $SPPs$ in the MIM detector structure which are absorbed by the pn junction leading to the creation of $EHPs$. The latter then gets collected as photocurrent. The largest photocurrent is observed where coupling to $SPPs$ is strongest. The structure is sketched on figure 1.10.

An SOI waveguide based silicide Schottcky barrier detector with metal-semiconductor-metal (MSM) configuration was proposed by Shiyang Zhu *et al.* for the first time using a simple low-temperature Si process [42]. Such detectors, in which light is absorbed in the silicide layer and the detection cutoff wavelength is determined by the Schottky barrier height (SBH) at the Silicide-Si interface are good alternatives to Ge photodetectors which are costly to integrate and have a very low absorption coefficient for Ge at wavelengths near or above the $L-band$ $(1561-1620nm)$ [42].

SOI waveguide-based silicide Schottky-barrier MSM PDs exhibit higher speed and responsivity when compared to similar Schottky barrier photodiodes with the same $NiSi_2$ absorber [42].The good performance beside the ease of fabrication made such detectors very promising for low-cost integrated Si-photonics, particularly near or above the $L-band$ [42].

Other MSM photodetectors are based on graphene which hold promise as a transparent and conductive electrode that can be integrated with current Silicon technologies. The Fermi level and thus, the workfunction of graphene can be tailored by chemical doping and electrostatic gating [43]. An example of graphene based MSM detectors is the device presented by Yanbin An *et al.* in [43] for a MSM photodetector based on graphene/p-type Schottky junction.

MSM graphene photodetectors were found to exhibit a larger photocurrent and pho-

tocurrent to dark current ratio than other MSM photodetectors that are based on carbon nanotubes [43].

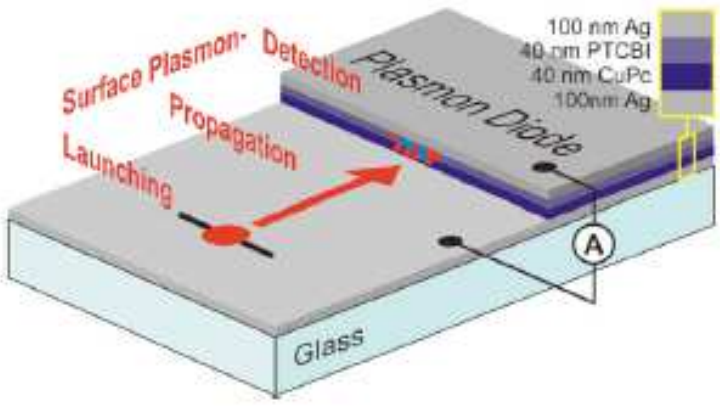

Figure 1.10: A sketch of an integrated plasmon diode device. The slits in the silver thin film are illuminated with a laser beam resulting in $SPPs$ that propagate towards the plasmon diode. They excite SPPs therein and generate charge carriers ($EHPs$) which are detectable as a direct current. Figure is adopted from [41].

A waveguide based Schottky photodetector which consist of symmetric metal slabs buried in Silicon is another important design of waveguide based photodetectors.

The use of symmetric metal stripes in waveguide based photodetectors was proposed by Scales and Berini [44]. They introduced a Schottky photodetector structure in which a metal stripe is buried in Silicon. This metal stripe is symmetrically cladded and supports the propagation of long-ranging SPP waves ($LRSPPs$). The structure is illuminated from the back as seen in Figure 1.11. In this case, the mode power attenuation decreases as well as the confinement. However, a great coupling efficiency into the SPP mode can be achieved due to the Gaussian-like distribution of the $LRSPP$ mode fields [5, 19]. To increase the mode power attenuation, a longer waveguide is required so that a total absorption of the coupled input optical energy is possible [5]. On the other hand, having a longer waveguide could result in the device being big in size which could contribute to an increase in the dark current [5]. The device supports two Schottky contacts along the upper and lower sides of the metal stripe leading to an increased opportunity for hot

carrier escape, thus increasing the responsivity [13].

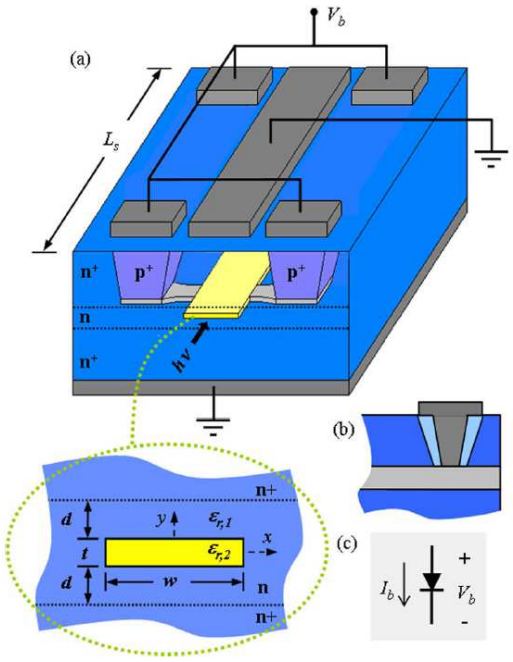

Figure 1.11: Surface-plasmon Schottky contact detector based on a metal stripe buried in Si. Adopted from [44]

.

Akbari and Berini adapted the model described by Scales and Berini [19] but, with an asymmetrically cladded metal stripe of finite width. This structure is useful for low-cost silicon based photonics as it does not uses a silicon upper cladding, which in fact increases the complexity of the fabrication process [18]. The device performance introduced an increase in the mode power attenuation as well as the field confinement relative to the structure presented by Scales. Also, the device structure was reduced in size which, in turn reduced the dark current. However, a large reduction in coupling efficiency into the SPP mode was achieved. The device was fabricated and tested experimentally by Akbari. The device as shown in Figure 1.12 consists of a gold stripe, with finite thickness and width, cladded asymmetrically by air on top and Silicon at the bottom and supports the propagation of short ranging SPP modes. The silicon substrate is composed of two layers, a lightly doped Silicon ($5\Omega cm$) on a highly doped Silicon layer ($0.005\Omega cm$).

Adapting the structure proposed by Akbari and Berini but with reducing the size of the structure even more could make this proposed photodetector to be of significant

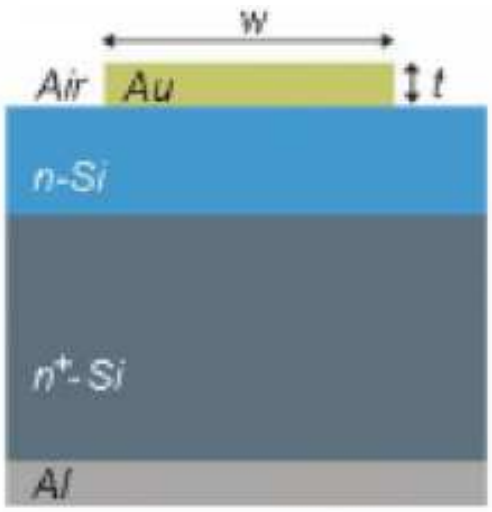

Figure 1.12: an asymmetric waveguide based photodetector. Figure is adopted from [18]

importance. The mode supported by a nano-structured metal stripe could hold promise for near-field scanning applications if it is supported by a tiny metallic structure.

In this thesis, the metal stripe was asymmetrically cladded by air on top and silicon at the bottom, similar to Akbari's structure but with the addition of using a tiny metal stripe. The metal used was not thicker than $50nm$ nor wider than $100nm$ with the smallest thickness and width being $10nm$.

The only mode investigated was the as_b^0 mode, known also as the fundamental mode, and it was very confined to the metal stripe especially at the wavelength $1310nm$. The mode power attenuation was high and increasing with decreasing stripe's thickness and width.

Although the device performance indicated the reduction in dark current compared to Akbari's results, the coupling efficiency into the SPP mode was also reduced to be around 6 times less than the coupling efficiency values produced by Akbari.

From the knowledge of Dirac delta function which gives a value only at zero on the real number line and everywhere else its value is zero, the SPP mode supported by a tiny metal was used to play the role of Dirac function when scanning a much larger mode field. As predicted, this tiny mode field can have the characteristics of a Dirac

delta function when multiplied by a much larger field distribution. In other words, when a function that is not a Dirac function is swept by a Dirac function, it gives the value of the function at the location of the Dirac delta function. As a result, when the Dirac delta is real, the coupling efficiency between the SPP mode field supported by the tiny metal stripe and a tapered fibre's mode field having a spot radius of $1.25m$ at an optical wavelength of $1550nm$ will give the fibre mode at the location of the tiny SPP mode. Further explanations are presented in Chapter 3. A definition of the Dirac delta function and its properties is included in Appendix C.

Chapter 2

Surface Plasmon Asymmetric Waveguides

This chapter describes and discusses the behaviour of the asymmetric bound SPP modes supported by a nano-structured metal film bound by different dielectrics. Both the metal's vertical and horizontal dimensions (t) and (w) are sub-wavelength $(t, w) < \lambda_0$ and waves can be guided along this nanowire. Au was the metal used as the waveguide core with dimensions ranging between $10-50nm$ thick and $10-100nm$ wide. The aspect ratio of the film is larger than one $(w/t > 1)$, so the transverse component of the electric field that is normal to the metal surface will dominate for all modes. Thus, they are mainly TM in nature [45].

An overview of some structures which support the propagation of SPP_S at metal/insulator interfaces is discussed at the beginning of this chapter.

2.1 Surface Plasmon Polaritons at metal/insulator interfaces

There are different metal/insulator structures which can support the propagation of SPP_S. The simplest example of a metal/insulator structure is the single interface metal/dielectric structure (discussed briefly in Appendix.A), in which the SPP_S propagate at the interface between the metal and the dielectric.

Another example is a metal with an infinite width that is sandwiched between two

thick dielectric claddings of permittivities ε_1 and ε_2. The propagation of SPP_S can be supported at both its upper and lower interfaces with the dielectric [46]. Such a structure is known as the slab waveguide structure in which the metal film with thickness (t), width (w), and permittivity (ε_3) guides the light through. If the metal is thin enough in such a waveguide structure, the SPP_S supported on both the upper and lower interfaces will interact forming coupled modes that exhibit dispersion with metal thickness [47, 9, 46]. This is due to tunnelling of light through the metal film [46]. The structure can be either symmetric (both upper and lower claddings have the same dielectric constant$(\varepsilon_1) = (\varepsilon_2)$) or asymmetric (upper and lower claddings have different dielectric constants$(\varepsilon_1) \neq (\varepsilon_2)$).

A structure similar, with the exception of a finite width thin metal, has been of a significant interest in the past decade due to its ability to provide $2D$ field confinement in the transverse plane whereas the slab waveguide structures provide only $1D$ field confinement. If the metal stripe is bound by two identical or similar dielectric claddings $(\varepsilon_1) = (\varepsilon_2)$, long ranging SPP modes ($LRSPP_S$) can be guided along the metal/dielectric interface which propagate with low confinement and loss, and are widely used for sensing [9]. However, if the metal stripe is bound by two different dielectric claddings $(\varepsilon_1) \neq (\varepsilon_2)$, short ranging SPP modes ($SRSPP_S$) which propagate with high confinement and loss can be guided along the metal/dielectric interface. SPP waveguide modes with low confinement radiates only if bent too aggressively while SPP modes with high confinement can be aggressively bent without radiating [48].

In this thesis, I simulated the asymmetric structure using a finite width gold stripe deposited on a silicon substrate and covered by air. The interface between the metal stripe and silicon, which is also a Schottky barrier, allows for the propagation of short-range asymmetric bound SPP modes that are known to have high confinement and loss.

Below is a description of the two aforementioned structures and the modes that can be supported by each of them.

2.1.1 SPP_S on Slab Waveguides

The slab waveguide structure or the optical slab only supports the propagation of two purely bound TM modes which are guided by the slab. Each mode has three field com-

ponents. The electric field of the mode consists of only one single component that is perpendicular to the interfaces and has either symmetric or asymmetric field distribution across the waveguide [9].

The fields related to the symmetric mode are known to have small attenuation and loss. On the other hand, fields that are related to the asymmetric mode are of high attenuation and loss. The latter penetrates further into the metal than the fields of the symmetric mode [11].

The structure mainly consists of an infinitely wide metal film bound by dielectrics with the metal film being the waveguide core. A sufficiently thin metal film can cause the plasmon polariton modes, which are guided by the upper and lower metal/dielectric interfaces, to couple, forming supermodes. Such modes are known to exhibit dispersion with metal thickness.

With the increase in the metal thickness, the supported symmetric or asymmetric modes will become degenerate and their propagation constants become similar to that of a single interface. They are expressed as follows [9]:

$$\frac{\beta}{\beta_0} = Re\{\sqrt{\frac{\varepsilon_{r,1}\varepsilon_{r,2}}{\varepsilon_{r,1}+\varepsilon_{r,2}}}\}, \tag{2.1}$$

$$\frac{\alpha}{\beta_0} = -Im\{\sqrt{\frac{\varepsilon_{r,1}\varepsilon_{r,2}}{\varepsilon_{r,1}+\varepsilon_{r,2}}}\}, \tag{2.2}$$

where:

$$\beta_0 = \frac{\omega}{c_0} \tag{2.3}$$

with $\varepsilon_{r,1}$ and $\varepsilon_{r,2}$ being the complex relative permittivities of the metal and dielectric used in the waveguide, c_0 being the velocity of light.

Slab waveguide structures offer only one dimensional field confinement in the direction perpendicular to the wave propagation direction which cause them to be of limited interest [9].

2.1.2 SPP_S on finite width Waveguides

More interesting properties are found in a metal film of finite width that is symmetrically or asymmetrically cladded. It is similar to the slab waveguide structure but differs in having a finite width metal film instead of infinite. This finite width metal film, the waveguide core, offers $2D$ field confinement in the transverse plane. The structure was studied and tested by Berini et al., using symmetric and asymmetric dielectric claddings [50, 11, 9, 12, 49]. The nature of the modes supported by the structure and their properties are highly dependent on the background (symmetric or asymmetric). The evolution of the modes supported by this structure with metal thickness is similar to the evolution of the modes supported by infinitely wide films [45]. In addition to a number of higher order modes, there were four fundamental modes identified ($aa_b^0, as_b^0, sa_b^0, ss_b^0$) [45].

2.1.2.1 SPP_S on Symmetric finite width Waveguides

The symmetric waveguide structure, composed of a thin lossy metal film of thickness t and finite width w embedded in an optically infinite homogeneous dielectric operating at optical wavelengths, was studied and tested experimentally by Berini et al. in [9], [50], [47], [51], and in [52]. The structure uses a thin, finite width metal film of a high aspect ratio ($w >> t$) [52]. When the aspect ratio of the film is larger than 1 ($w > t$), the E_y field dominates for all the supported modes which, in this case, are mainly (not purely) TM modes [52]. On the other hand, when the aspect ratio is less than 1 ($w < t$), the E_x field dominates for all modes [53]. A waveguide structure such as this is promising for integrated optics technology, especially due to its ability to confine light along both dimensions in the plane transverse to the direction of propagation [52].

The structure supports some higher order modes and four fundamental modes labelled $aa_b^0, as_b^0, sa_b^0, and ss_b^0$ [52]. The evolution of modes with metal thickness and width (t, w), material parameters $(\varepsilon_1, \varepsilon_2, \varepsilon_3)$, and operating free space wavelength (λ_0) is complex due to the fact that those modes are initially supermodes that were generated from the coupling of "edge" and "corner" surface waves and each supermode is formed by waves of close proximity in phase constant [52]. By decreasing the metal thickness and width (t, w), the fundamental mode (ss_b^0) evolves smoothly and experiences a significant decrease in attenuation, much more than the attenuation of modes supported by the corresponding slab waveguides. Furthermore, the E_y and H_x field components of the mode exhibit a symmetric Gaussian-like cross sectional distribution which makes this

mode suitable for efficient end-fire coupling with single mode optical fibres [52].

2.1.2.2 SPP_S on Asymmetric finite width Waveguides

A waveguide structure composed of a thin lossy metal film of thickness (t), finite width (w), and permittivity ε_3 supported by a semi-infinite homogeneous dielectric substrate of permittivity ε_2 and covered by a semi-infinite homogeneous dielectric superstrate of permittivity ε_1 is an important class of waveguides which was first introduced by Berini [49]. He described the waveguiding characteristics of such structures which are totally different from the waveguiding characteristics of the corresponding asymmetric slab waveguides or symmetric finite-width waveguides. This is the structure of interest in this thesis, where a thin Au film of finite width is deposited on Silicon substrate and covered by air. A sketch of the structure is shown on figure 2.1.

The propagation of modes is along the z axis (out of the page) along which the structure is invariant. Variation of mode fields along the z axis follow $e^{-\gamma z}$ where γ is the complex propagation constant of the mode, given by:

$$\gamma = \alpha + j\beta \tag{2.4}$$

where α and β, respectively, are the attenuation and phase constants.

Metals which are highly conductive and semiconductors or dielectrics are usually used to construct the waveguide. [13]. Au was chosen to be the stripe used in the structure as it has a good optical performance [12], [13]. Also, its interfacing properties with silicon are very well known [5]. In addition, it was theoretically predicted that Au waveguide structures exhibit low losses [12]. Moreover, the chemical stability of Au makes it an interesting metal to use for supporting $SPPs$ [13]. Metals that support $SPPs$ must satisfy $\varepsilon_R \gg \varepsilon_I$ [13].

The performance assessments of the asymmetric Au stripe were achieved by assuming the interpolated relative permitivities for Au to be $(-86.06 - 8.32 * i)$ and $(-131.9475 - 12.6500 * i)$ at $\lambda_0 = 1310mn$ and $\lambda_0 = 1550nm$, respectively [5] [54].

If the wavelength increases into the far-infrared region and beyond, the permittivity approaches that of a perfect electric conductor and the SPP confinement decreases [13].

Si, which is the material used for the substrate, has negligible absorption at the previously mentioned optical wavelengths and thus is characterized by its refractive index $n = 3.4764$ and 3.5029 at $\lambda_0 = 1550nm$ and $1310nm$, respectively [5].

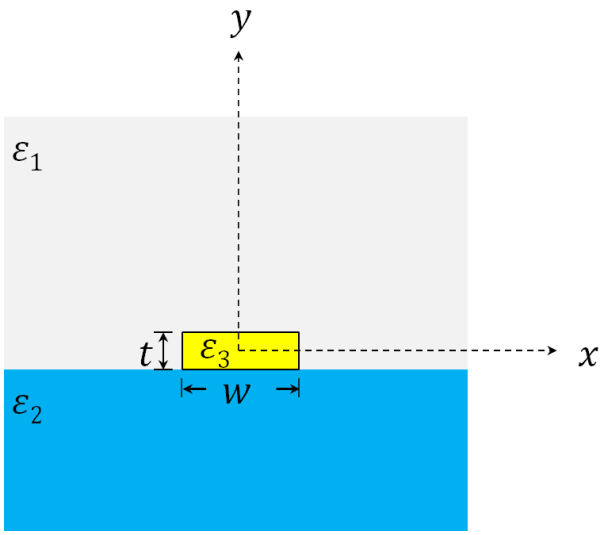

Figure 2.1: A cross-sectional view of an asymmetric stripe waveguide structure of thickness (t), width (w), and permittivity (ε_3) surrounded by two semi-infinite different dielectric claddings of permittivity ε_1 and ε_2. .

Modes supported by such a structure have a different spectrum than the modes supported by either the finite width symmetric waveguides or the asymmetric slab waveguides. They experience a switching of constituent interface modes as film dimensions change. The structure supports a long ranging mode above a certain cut-off thickness that is even larger than the cut off thickness of the long ranging mode in asymmetric slab waveguides. In addition, the long ranging mode supported by a metal film of finite width bound by different dielectrics experiences a rapid decrease in attenuation with decreasing film thickness much more than the decrease in attenuation experienced by symmetric structures when decreasing film thickness.

Solving for the modes that are supported by the structure was done numerically by solving a boundary value problem based on Maxwell's equations. Such a problem cannot be solved analytically. A finite element method (FEM) was used to solve for the modes

using Comsol Multiphysics [55]; by which the spatial distribution over the waveguide cross-section of the transverse field component E_y related to a supported mode and the propagation constant of the mode are computed.

In this study, I focused on the fundamental mode (as_b^0) supported by this structure and its unique electrical characteristics. The absolute field distribution of the transverse electric field component (E_y) of this mode is shown at the end of this chapter at a free space optical wavelength of $1310nm$ and $1550nm$, respectively.

The analysis of the structure shown on figure 2.1 in Comsol Multiphysics was done using the material parameters mentioned above for Au at two optical wavelengths 1310 and 1550, and for a range of different Au thicknesses and widths. The thickness of Au stripe ranges from $10nm$ to $50nm$ and the width ranges from $10nm$ to $100nm$.

The modes supported by a finite-width metal bound by different dielectrics are symmetric or asymmetric with respect to the vertical axis ($y - axis$); and, they can be symmetric (not in simple structures) or asymmetric with respect to the horizontal axis ($x - axis$) with the field being localized along the top or bottom metal/dielectric interface. If the field is localized along the metal/dielectric interface with the lowest dielectric constant, then the supported modes will be symmetric with respect to x-axis. If the field is localized at the metal/dielectric interface with the highest dielectric constant, then the supported modes will be asymmetric with respect to the x-axis [49]. In this study, the supported modes are localized at the metal/Si interface and since silicon has a higher refractive index than air, the modes will have an asymmetric-like nature with respect to the x-axis.

Metal films of limited thickness and width can have useful applications in optical signal transmission and routing over short distances. They can also be used to construct passive components like couplers and power splitters [49].

2.2 Metal Nanowires and Transverse Confinement Below the Diffraction Limit

It is very well known that metal waveguides whose crosssection is $\ll \lambda^2$(the square of the wavelength of the guided radiation) can have mode confinement below the diffraction limit in the surrounding dielectric [46]. This confinement occurs in the transverse dimension [46].

For propagation along the z-direction, the transverse components of the wavevector k_x, k_y and the frequency ω of the guided radiation in a general waveguide are related to the propagation constant β $(= k_z)$ as per the following relation [46]:

$$\beta^2 + k_x^2 + k_y^2 = \varepsilon_{core}\frac{\omega^2}{c^2} \tag{2.5}$$

knowing that k_x, k_y are real in a dielectric waveguide, the latter equation can be re-written as [46]:

$$\beta, k_x, k_y \leq \sqrt{\varepsilon_{core}}\frac{\omega}{c} = \frac{2\pi n_{core}}{\lambda_0} \tag{2.6}$$

Due to the uncertainty relation between wave vector and spatial coordinates, three dimensional optical waves have a mode size that is governed by the effective wavelength in the core medium [46]:

$$d_x, d_y \geq \frac{\lambda_0}{2n_{core}} \tag{2.7}$$

On the other hand, if the core medium of the waveguide was of metallic character and, if attenuation was ignored, then $\varepsilon_{core} < 0$. Equation 2.5 can not be satisfied unless one or both of the transverse vector components k_x, k_y is imaginary - the guided waves are two- or one-dimensional, respectively [46]. In this case, equation 2.7 does not apply, and the mode size can be substantially below the diffraction limit of a dielectric waveguide [46].

2.3 Modelling Of Asymmetric Bound SPP modes

2.3.1 Numerical Simulations

Unlike the slab waveguide structure and the single interface metal/dielectric structure whose mode solutions can be obtained analytically, two-dimensional surface plasmon-polariton waveguides can only have mode solutions via numerical methods. Accurate analysis is challenging as there are large permittivity contrasts between the metal and the dielectric, as well as strong localisation of mode fields, mainly near the corners of the metal [56]. Comsol Multiphysics, which is the finite element method (FEM) mode solver that was used to solve for the asymmetric bound SPP modes supported by this structure in the frequency domain, can provide spatial distributions over the waveguide cross section of all the field components of the supported mode and compute their propagation constant [57]. A good mesh that generates a solution with negligible errors was needed in order to gain confidence in the accuracy of the computed solution. A convergence study was conducted to test the quality of the solution produced and to make sure that the sequence of solution converged as expected.

The waveguide structure was built by having three rectangles stuck together. The rectangle in middle, representing the metal, was much narrower in width (a finite-width waveguide structure) and the top and bottom rectangles were wide and equal in width. All three rectangles together represent the computational domain which must be large enough. In other words, the top and bottom boundaries of the computational domain must be placed far enough from each other to solve for the asymmetric bound mode that is supported by the structure. The lateral boundaries must also be placed far enough from the metal to ensure the mode's field is approaching zero near to the boundaries. The solved field intensities around the boundaries of the domain were forced to zero by applying perfect electric conductor boundaries. As the structure is horizontally symmetric about the stripe's center, a perfect magnetic conductor was applied across this axis in order to solve for the horizontally symmetric SPP modes while reducing the total number of elements required for the solution by a factor of 2. This technique increased the accuracy of the solution even more by allowing the use of double the computational power. If applying a perfect electric conductor along the vertical axis of the stripe's centre instead of a magnetic one, horizontally asymmetric SPP modes will result.

The materials were defined by the optical permittivity and the refractive index parameters which were given earlier in this chapter for Au, Air, and silicon at both $\lambda_0 = 1310nm$ and $\lambda_0 = 1550nm$.

The numerical solution given by Comsol for solving the mode is the complex effective refractive index of the mode which must have a real part that is greater than the index of refraction of both the substrate and the superstrate. The following equation represents the complex effective refractive index of the mode:

$$n_{eff} = \frac{\beta}{\beta_0} - i\frac{\alpha}{\beta_0} \tag{2.8}$$

Where the real and the imaginary part of the effective refractive index are given by [11]:

$$\frac{\beta}{\beta_0} = Re\sqrt{\frac{\varepsilon_{r,1}\varepsilon_{r,2}}{\varepsilon_{r,1} + \varepsilon_{r,2}}} \tag{2.9}$$

and,

$$\frac{\alpha}{\beta_0} = -Im\sqrt{\frac{\varepsilon_{r,1}\varepsilon_{r,2}}{\varepsilon_{r,1} + \varepsilon_{r,2}}} \tag{2.10}$$

In the structure's cross section shown on figure 2.1, the mode propagates in (+z) direction (out of the page) which is taken to be the direction of propagation throughout this thesis.

Because the computational power is limited, a good mesh is needed for the top and bottom interfaces of the metal film and the area surrounding them. Selecting the areas of interest in refining the initial mesh is crucial since refining the initial mesh several times for the whole computational domain could consume power and time making it hard to set a dense mesh for the metal and its surroundings where the mode disperses. Therefore, sections that are away from the structure where almost no field exists were excluded from multiple mesh refinements in order to allow for more mesh refinement at the chosen area of interest (the metal boundaries and their vicinity), making it possible to obtain a converged mesh that provides more accurate mode solution. .

2.3.2 Convergence

The strong localization of mode fields and the large permitivity contrast between the metal and the dielectric made it hard to achieve accurate mode analysis; therefore, a convergence study was necessary in this research in order to evaluate the accuracy of the mode solution produced [53]. The study aims to create a mesh that is able to produce a converged mode solution that maintains a good level of accuracy. The following is a description of how convergence was studied in this thesis:

As was discussed previously in this chapter, the waveguide is composed of a finite width Au stripe deposited on a silicon substrate and covered by air. The size of the Au stripe was very small, ranging between $10nm$ to $50nm$ of thickness and $10nm$ to $100nm$ of width. Compared to the size of the silicon substrate and the computational area defined as air, the metal size was very small. Since it was not possible to do multiple mesh refinement for the whole computational domain as this requires a lot of memory and time, especially because of the small size of Au stripe, the solution was to subdivide this domain into many smaller domains so that a mesh can be refined only at the areas of interest. Instead of having three sub domains (Silicon, Au, air), there was an additional four sub-domains leading the computational domain to be composed of 7 computational sub-domains in total, as seen in the sketch shown on figure 2.2. All the sub-domains are rectangular and were given different mesh sizes with the smallest mesh size being in sub-domains 6 and 7 (the Au/silicon upper and lower interfaces), which both represent the areas were the field is maximum.

A triangular mesh was initialized for the whole computational domain with the maximum element size fixed to $5nm$ for domains 1&2, $0.5nm$ for domains 4&5, and decreasing gradually from $0.1nm$ to $0.03nm$ for domains 6&7 which represent the metal/dielectric interfaces. In contrast, the maximum element size of domain 3 was fixed to be $1nm$ as there does not exist any field near the centre of the metal and there is no need to refine this sub-domain. The convergence study was mainly conducted for sub-domains 6&7 due to two reasons. The first, because of the fact that the field is maximum at the interfaces, they can largely affect the mode solution produced; therefore, those sub-domains were given priority in tracking convergence. The second, was due to the memory consumption and the need to decrease the number of elements required for the solution to be able to set a fine mesh for sub-domains 6&7 and as a result, be able to get more accurate results.

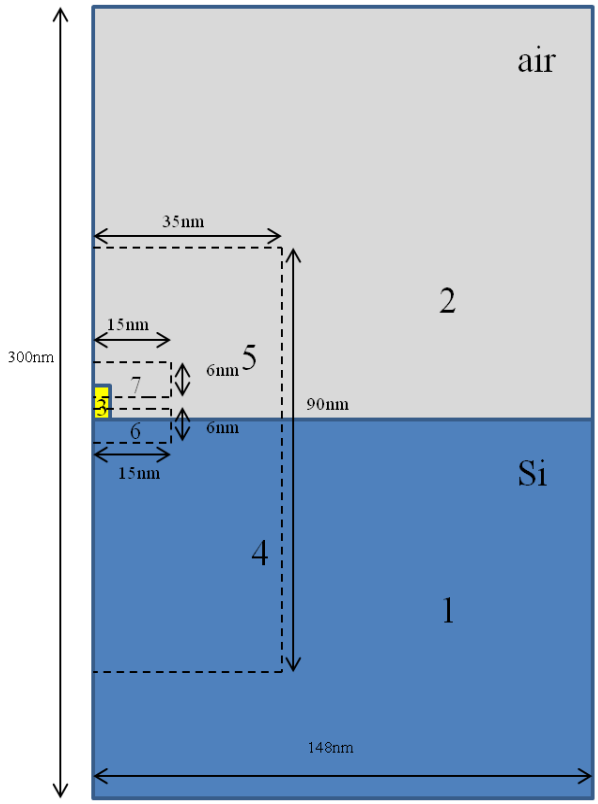

Figure 2.2: Schematic representing the sub-division of the waveguide structure during the convergence study.

The maximum element size of the lateral domains was gradually decreasing from $0.1nm$ to $0.03nm$ and the effective index of the mode was gradually decreasing until the real part of effective index $R_e(n_{eff})$ maintained 3 digits of accuracy at a maximum element size of $0.03nm$. The level of accuracy is highly affected by the computational power available since the mesh of small and thin sub-domains in the structure increases the effort and results in consuming memory and time. The aforementioned case is related to sub-domains 6&7 which are incredibly small ($6nm$ in height and $15nm$ in width). The machine I used for the simulations would run out of memory if I decreased the maximum element size in sub-domains 6&7 beyond $0.03nm$; it could not provide more than 3 digits of accuracy even when I tried to make large maximum element sizes for the larger sub-domains. I believe, however, that using high computing tools could provide at least 5 digits of accuracy for such a nano-structured device. And, the maximum element size of sub-domains 6&7 could decrease to less than $0.03nm$, leading to much more accurate mode solutions for nano-structured SPP waveguides. Below is a plot of the real part of effective index $R_e(n_{eff})$; which is equivalent to $(\frac{\beta}{\beta_0})$ in equation 2.8; as a function of

mesh size according to this study:

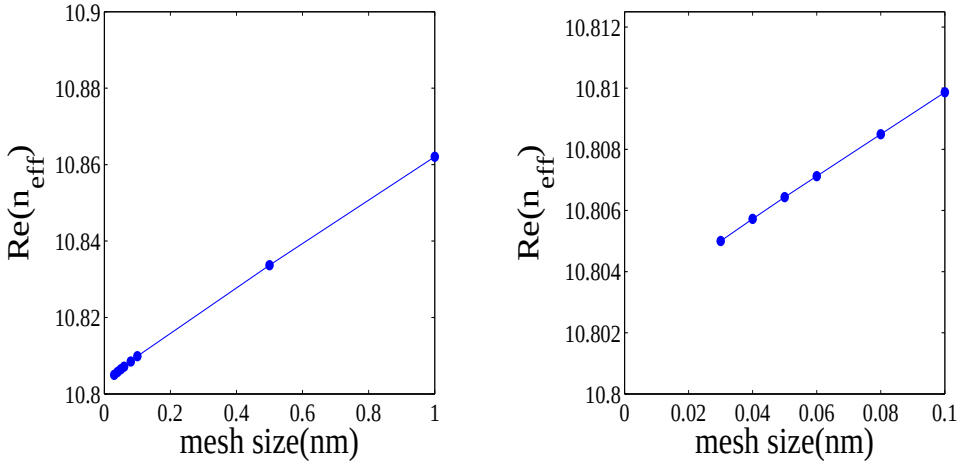

Figure 2.3: (a) Real part of effective refractive index as a function of mesh size. (b) a zoom in the mesh sizes between 0 and $0.1nm$.

Figure 2.3 shows how the real part of effective index converges with the mesh size. Figure 2.3, part (b), is a zoom in on the mesh sizes between 0 and $0.1nm$, indicating that the real part of effective index maintained three digits of accuracy at a maximum element size of $0.04nm$. The imaginary part of effective index, however, maintained two digits of accuracy.

As noted in figure 2.3, the simulations were done for half of the structure only. Given that the mode is symmetric at the vertical axis, a magnetic wall was defined along this axis to be able to double the computational power, enhancing the mode solution.

An accurate selection of the size of the computational domain was considered so that a good mesh could be made without being off on the computational power available. For example, the computational domain for a metal that is $10nm$ thick and $10nm$ wide was taken to be smaller at the wavelength $1310nm$ than the wavelength $1550nm$. This is because the wavelength $1310nm$ allows for more mode confinement than the wavelength $1550nm$ thus there was no need to make a large computational domain at this wavelength.

The field peaked at the metal/dielectric interface and thus, it was clearly observed with having asymmetric and symmetric nature of field vertically and horizontally, re-

spectively. This can be clearly observed in figures 2.10 and 2.11.

2.4 Modelling Results

In this thesis, the mode solutions for the waveguide were produced in Comsol Multiphysics, by which the effective index of the guided modes was calculated. Calculations of the mode's effective index and loss as the structure dimensions vary were carried out in Matlab scripts. A variety of structure sizes were studied in this work.

2.4.1 Effects of Varying Stripe's Thickness on the Behaviour of the Fundamental Mode as_b^0 at $\lambda_0 = 1310nm$ and $1550nm$

2.4.1.1 Mode Confinement and Loss as a Function of Waveguide Thickness

The mode confinement can be defined as the fraction of the power flowing through the stripe to the total power in the mode [46]. In other words, a strong mode confinement or tight field localization to the metal interfaces signifies that more energy of the mode is localized inside the metal itself [46]. Sub-wavelength mode confinement of electromagnetic energy, leads to sub-micron propagation lengths [46]. Many experimental results demonstrated the possibility of propagation of SPP along nanowires and achieving large confinement [**?**, 11, 18]. This raised the interest in doing more investigations about the transverse field confinement that resulted when using stripe waveguides [46].

Figures 2.4, 2.5 show that both the real effective index and the loss (imaginary part of effective index) increase as the thickness (t) of the metal stripe decreases. This causes the mode power attenuation to increase and the propagation length of the SPP modes to decrease. The decrease of propagation length arises when the stripe dimensions become comparable with the wavelength of excitation and it decreases even more as the stripe dimensions become even smaller [46].

The increase in mode power attenuation with decreasing (t) is due to the increase in mode confinement. In other words, the bound SPP modes become more confined to the metal stripe. Increasing mode confinement means that the metal absorbs more optical

energy [46].

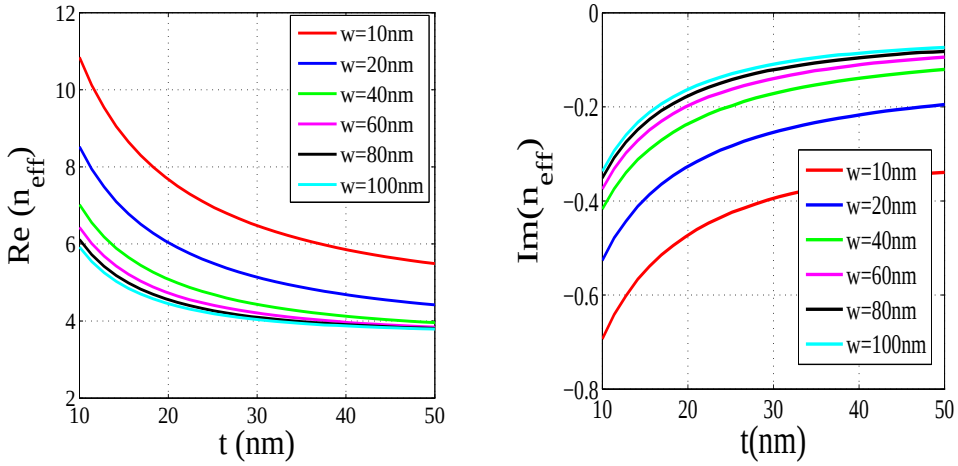

(a) (b)

Figure 2.4: Real (a) and imaginary (b) part of effective index as a function of stripe thickness (t), with stripe width (w) varying from $10nm$ to $100nm$ at $\lambda_0 = 1310nm$.

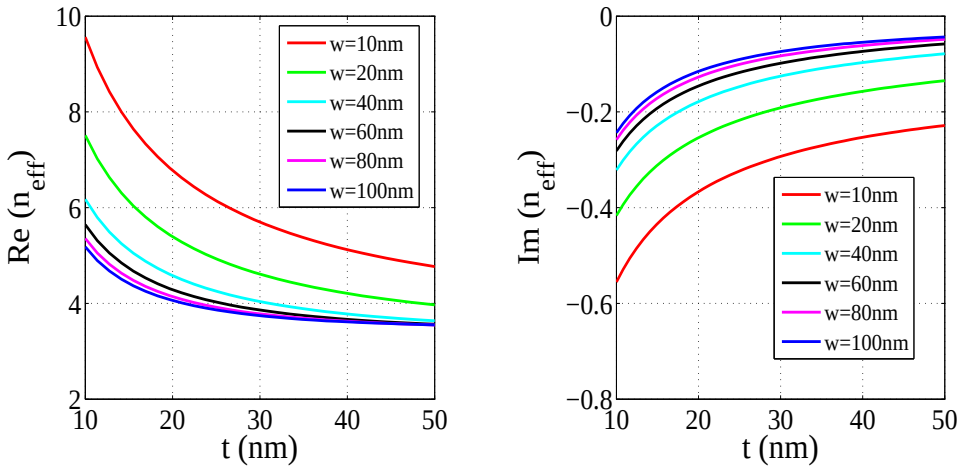

(a) (b)

Figure 2.5: Real and imaginary part of effective index as a function of stripe thickness, with stripe width varying from $10nm$ to $100nm$ at $\lambda_0 = 1550nm$.

2.4.1.2 Mode Power Attenuation as a Function of Waveguide Thickness

In order to understand the mode power attenuation, it is worthwhile to define the propagation length of the mode that is known as the distance from the launch point at which

the mode power gets reduced by a factor of $1/e$. It is given by:

$$L = \frac{1}{2\alpha} \tag{2.11}$$

Calculations of the mode power attenuation (MPA) are central to the evaluation of the waveguide performance. They were used to compare the performance of several structures operating at different wavelengths or having different designs or different materials [53].

A simple definition of the mode power attenuation (MPA) is the power loss per unit length [20]. It can be computed in dB/mm using the attenuation constant (α) in m^{-1} as follows:

$$MPA = \alpha \frac{20}{1000} log_{10} e \tag{2.12}$$

The attenuation is directly proportional to the mode confinement [53]. A high mode confinement will always result in high attenuation and vice versa. An example of highly confined and highly attenuated modes is the mode supported by an asymmetric metal stripe having a finite width. This was the mode of interest in this research.

It is clearly shown on figure 2.6 that the mode power attenuation increases with a decreasing metal thickness. This increase is mainly due to Ohmic heating and it reveals that the propagation distance decreases with a decreasing metal thickness.

The highest attenuation is produced when the stripe's thickness and width are only $10nm$. In this case, the propagation length of the asymmetric bound SPP modes is the shortest propagation length predicted in this research.

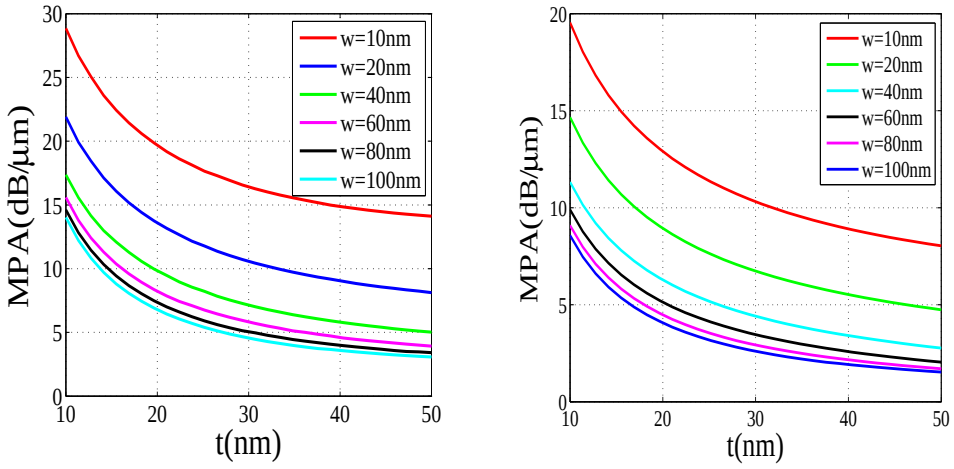

Figure 2.6: Mode power attenuation as a function of stripe thickness, with stripe width varying from $10nm$ to $100nm$ at (a) $\lambda_0 = 1310nm$ and (b) $\lambda_0 = 1550nm$.

As seen on figure 2.6, a high mode power attenuation occurs at the wavelength $1310nm$ mainly due to the high mode confinement at this wavelength.

2.4.2 Effects Of Varying Stripe's Width on the Behaviour of the Fundamental Mode as_b^0 at $\lambda_0 = 1310nm$ and $1550nm$

2.4.2.1 Mode Confinement and Loss as a Function of Waveguide Width

It is seen on figure 2.7 at the wavelength $1310nm$ that both the real and imaginary part of effective index are inversely dependant on the metal width. They increase with a decreasing metal width, leading to an increase in the mode confinement and a decrease in the propagation length of the SPP modes. Similarly, at the wavelength $1550nm$, figure 2.8, both the effective index and loss are also increasing with the decreasing metal width (w); though with less values than the wavelength $1310nm$. Those results confirm the ones produced as a function of change in stripe thickness. Figures 2.4, and 2.5 both conclude that structures operating at the wavelength $1550nm$ provide less mode confinement, less loss, and more propagation length for the SPP modes when compared to the ones operating at the wavelength $1310nm$.

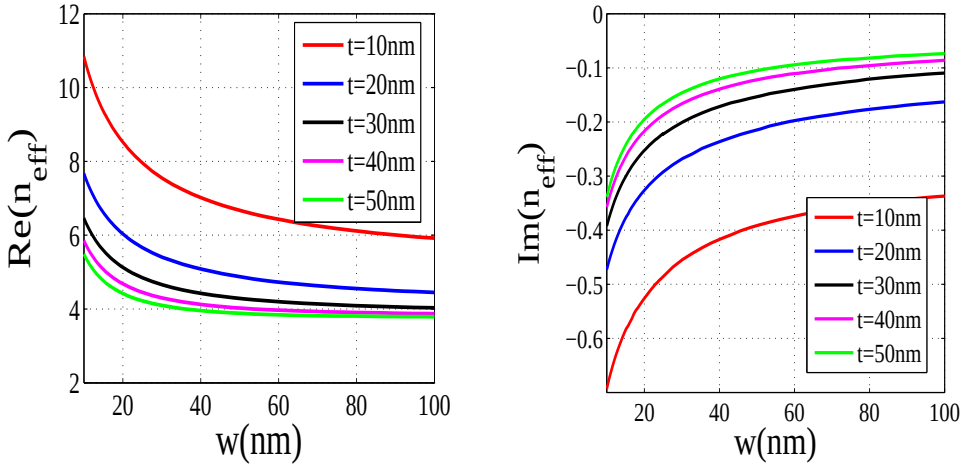

(a) (b)

Figure 2.7: Real (a) and imaginary (b) part of effective index as a function of stripe width, with stripe thickness varying from $10nm$ to $50nm$ at $\lambda_0 = 1310nm$.

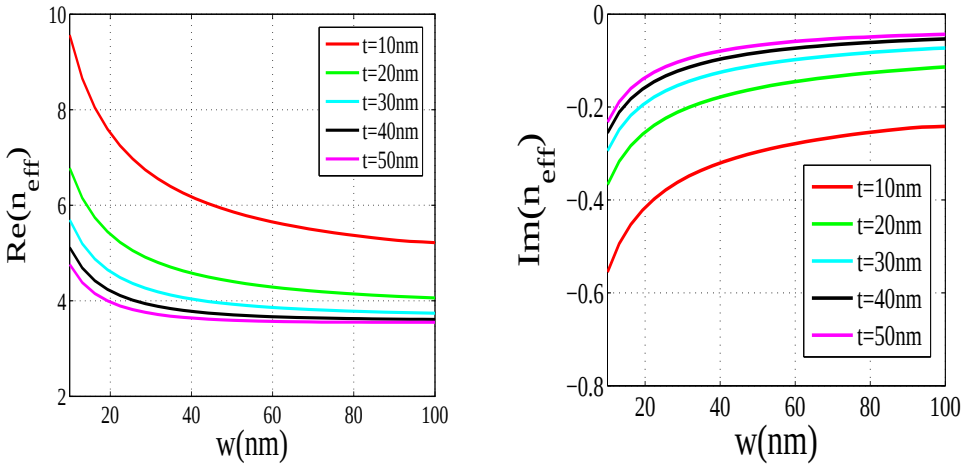

(a) (b)

Figure 2.8: Real (a) and imaginary (b) part of effective index as a function of stripe width, with stripe thickness varying from $10nm$ to $50nm$ at $\lambda_0 = 1550nm$.

2.4.2.2 Mode Power Attenuation as a function of Waveguide Width

Figure 2.9 shows that the mode power attenuation increases with a decreasing metal thickness. In conclusion, using thin metal stripes in asymmetric finite-width waveguide structures shortens the propagation length of the SPP modes.

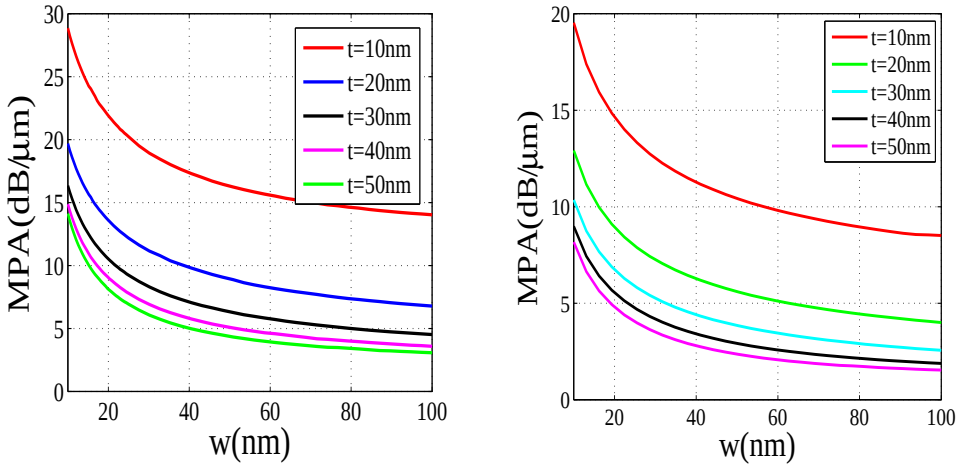

Figure 2.9: Mode power attenuation as a function of stripe width with stripe thickness varying from $10nm$ to $50nm$ at (a) $\lambda_0 = 1310nm$ and (b) $\lambda_0 = 1550nm$.

Calculations of mode power attenuation as a function of change in stripe width at the wavelength $1550nm$ show an increasing attenuation with a decreasing stripe width; however, the attenuation values are still smaller compared to the calculations done at the wavelength $1310nm$. Figure 2.9 indicates this observation.

2.4.3 The Fundamental SPP mode propagating along a nano-structured gold stripe

Although an asymmetrically cladded metal stripe of finite width can support many propagating modes, only the fundamental mode as_b^0 was studied in this research. This is due mainly to the good coupling which can be achieved when this mode overlaps with the mode of an optical fibre. Different fundamental modes supported by many Au stripes of different thickness and width were studied throughout this research and different mode characteristics were observed for the different structure sizes studied.

2.4.3.1 Mode Field Distributions

The dispersion of any SPP mode depends on the nature of the surrounding dielectric [14]. This fact forms the basis for the manufacturing of SPP based modulators and switches as well as for the applications of biochemical sensing [14]. Due to the con-

finement of the SPP field to the metal/dielectric interface, it was possible to overcome the diffraction limit encountered in classical optics and make highly integrated optical devices [14]. In addition, due to resonant build-up, the local electric field at the corners and edges of metallic elements is enhanced, thus nonlinear optical effects are enhanced as well [14].

As noted on figure 2.10, the field distributions tend to be localized at the corners for very thin metal strips and tend to have a single lobed distribution beneath the strip with increasing the metal thickness and width. For example, Akbari [5] investigated the mode supported by the structure shown on Figure 1.12 at $\lambda_0 = 1310nm$ and found that the fundamental mode (as_b^0) is localized at the corners for strip thickness ($t = 15nm$) and having a single lobed distribution along the strip width for strip thickness ($t = 100nm$). Both of our results demonstrate a decreasing propagation length and an increasing mode confinement with decreasing strip's width.

The main reason behind this behaviour of the mode is the fact that the real effective index of the mode increases for narrow and thin stripes causing the mode to be confined to the metal/silicon interface. Similarly, the real effective index of the mode decreases for wider and thicker stripes causing the mode to spread into the dielectric of higher refractive index and maintain a Gaussian-like lobed distribution beneath the stripe.

My results parallel the ones produced by Akbari; however, the maximum thickness investigated by me was only $50nm$, which although was not enough to eliminate the field distribution above the stripe, it was enough to conclude that the field above the stripe vanishes for higher thicknesses. In addition, the maximum aspect ratio for the metal stripe that I investigated is only 2, while the maximum stripe dimensions investigated by Akbari was 45, which was suitable to achieve the single lobed distribution beneath the stripe. The field distribution of the mode shown in Figure 2.10 for a stripe having ($t = w = 10nm$) is actually localized at the corners, similar to the mode of $t = 15nm$ in Akbari's structure but it presents as a point source due to the very small stripe width, and indicates the fact that the metal stripe is tiny and squared.

My results, as seen in Figure 2.10, show that the (as_b^0) mode is vertically asymmetric and horizontally symmetric which are in good agreement with Akbari's results.

It is clearly seen in figure 2.11 that the modes are less confined at the wavelength $1550nm$ than at the wavelength $1310nm$. The as_b^0 mode variation with different stripe thicknesses and widths, figures 2.10, 2.11, demonstrate that the field is more intense beneath the stripe, especially near the corners; however, it tends to have a single lobed distribution that extends beneath the stripe into the Si substrate as the stripe gets thicker and wider. It is also noted that the field above the stripe vanishes as the stripe gets thicker and wider.

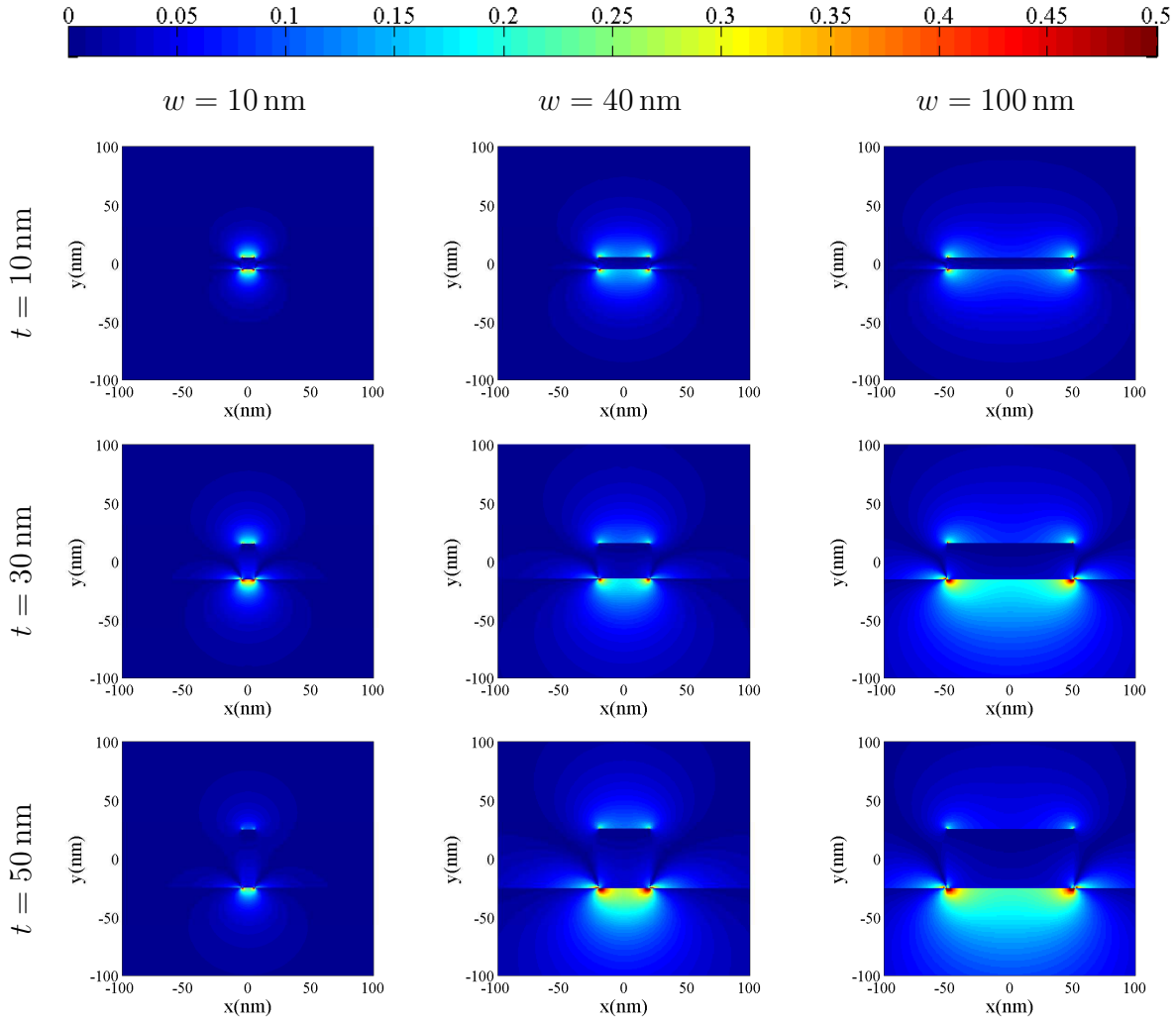

Figure 2.10: Field distribution (normalized absolute of Ey) of the first lower order bound SPP mode (as_b^0) supported by an asymmetric metal stripe at ($\lambda_0 = 1310nm$) for three stripe widths(w=10,40,100nm) and three thicknesses (t=10,30,50nm)

In those structures and because the metal stripe is embedded in an asymmetric en-

vironment, the two $SPPs$ supported at the two metal-dielectric interfaces have phase mismatch between them, thus long ranging modes cannot be supported by such structures.

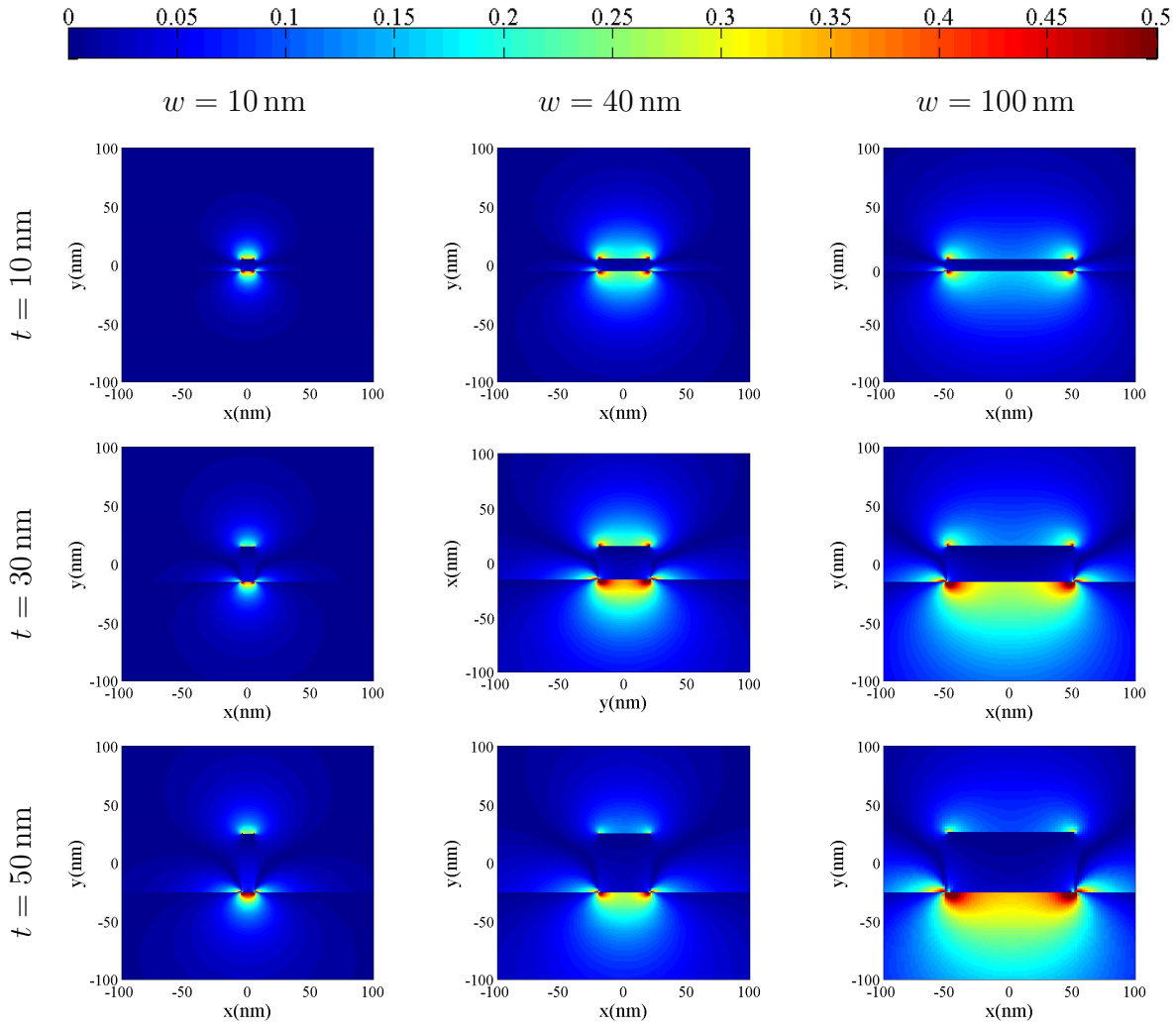

Figure 2.11: Field distribution (normalized absolute of Ey) of the first lower order bound SPP mode (as_b^0) supported by an asymmetric metal stripe at ($\lambda_0 = 1550nm$) for three stripe widths(w=10,40,100nm) and three thicknesses (t=10,30,50nm)

2.4.3.2 Mode Phase

The phase of the fundamental mode as_b^0 supported by an asymmetric metal stripe of finite t and w was studied for all the structure dimensions investigated in the previous section.

It is clearly seen on figures 2.12, 2.13 that the field switches sign across the interface. The phase difference is higher for stripes having small thickness and width; however, there exists almost no phase difference for stripes of large thickness and width.

The phase is plotted in the range between $-\pi$ and π for all the fundamental modes studied at both operating wavelengths.

Results show correlation between mode confinement and phase. For example, the mode supported by a metal of $10nm$ thickness and width that is operating at the wavelength $1310nm$, experiences a high confinement as well as a large phase difference across the interface.

Figure 2.12 is the phase calculated for the modes generated at $1310nm$ and figure 2.13 is the phase calculated for the modes generated at $1550nm$.

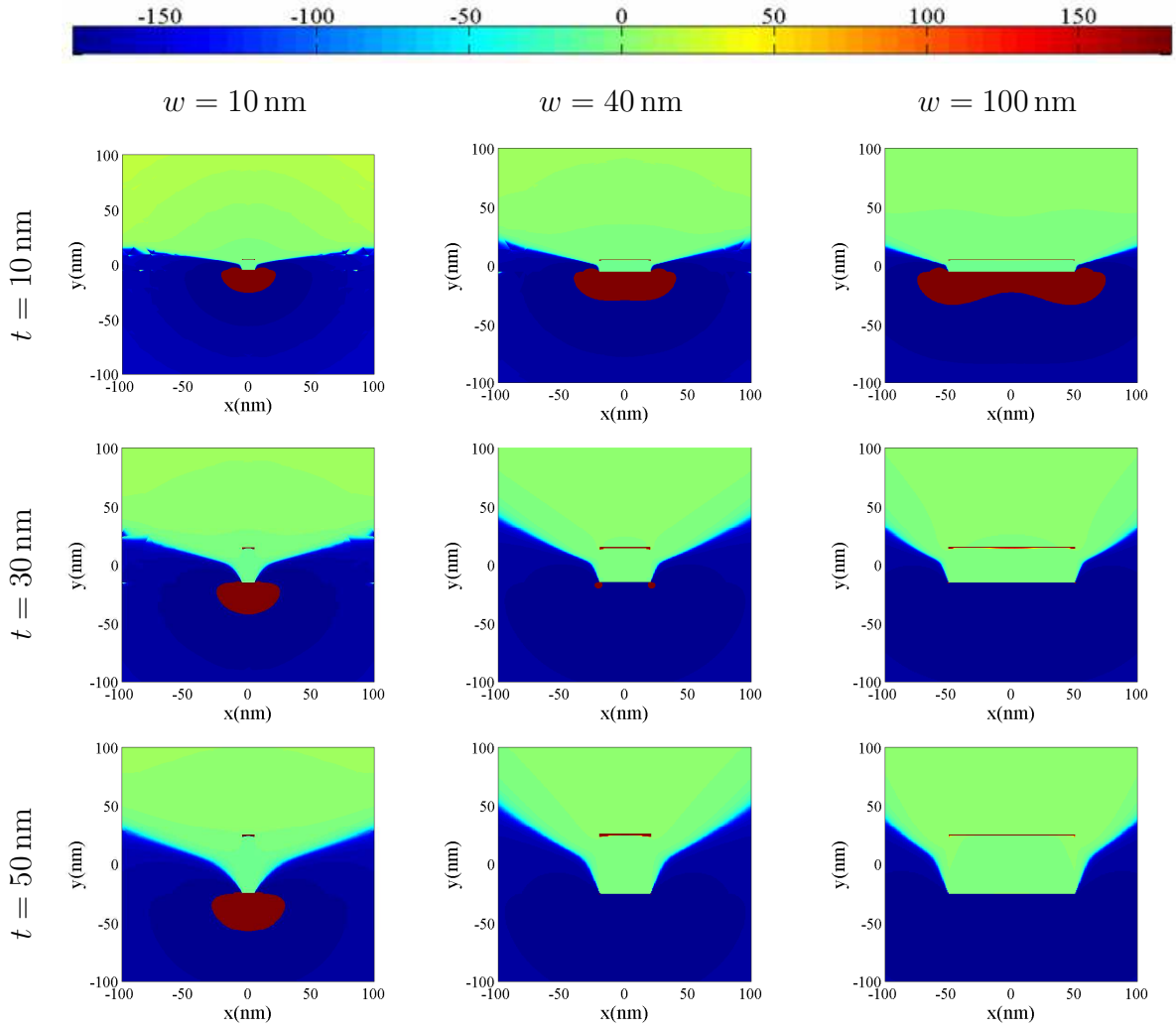

Figure 2.12: Phase of the first lower order bound SPP modes (as_b^0) shown on figure 2.10

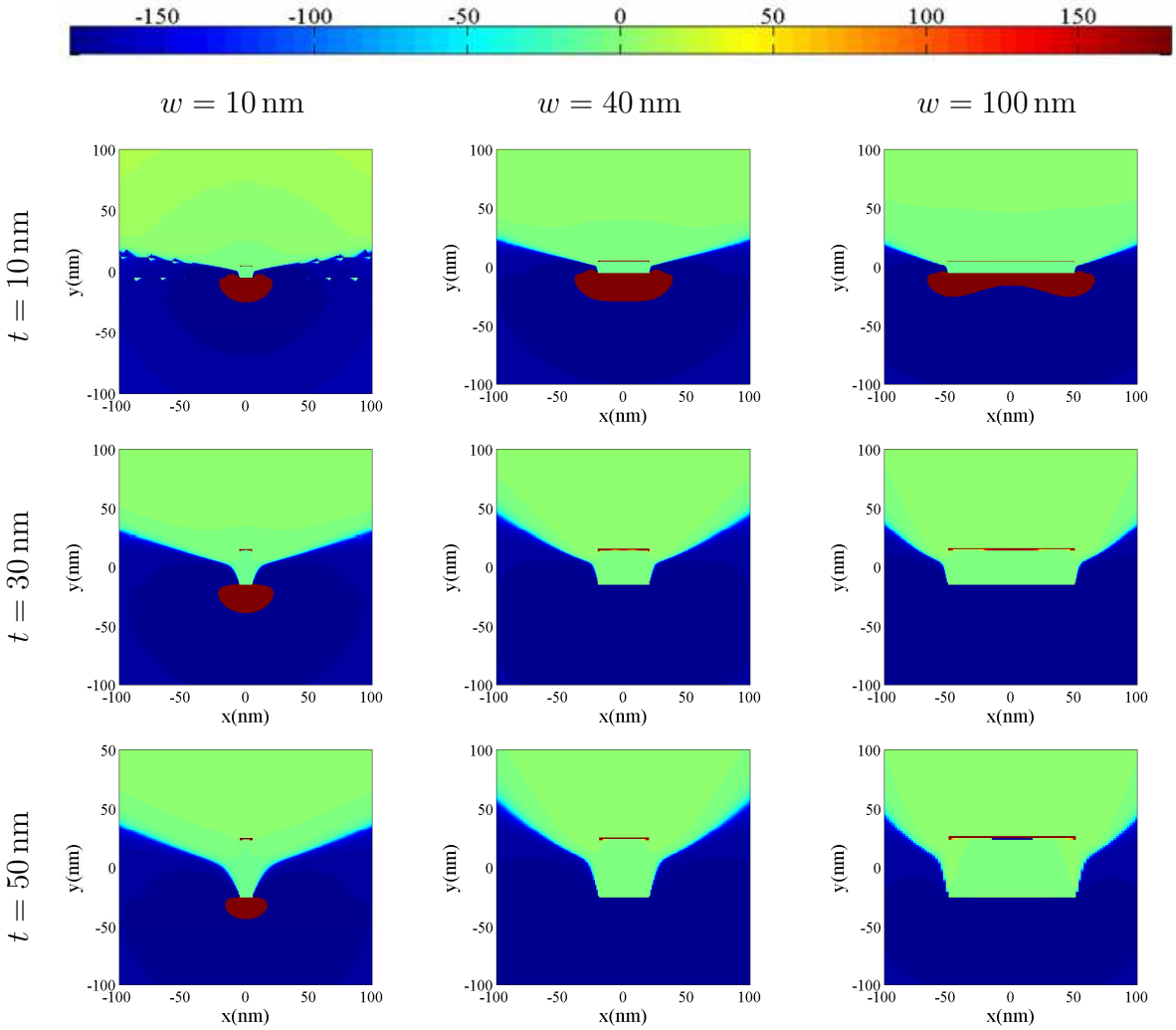

Figure 2.13: Phase of the first lower order bound SPP modes (as_b^0) shown on figure 2.11

Chapter 3

Schottky Contact Photodetectors

This chapter contains an overview of Schottky photodetectors, the detection mechanism adopted, the detector designs used in this research, the coupling characteristics as a function of variation in structure's thickness and width, the device performance as a near-field scanner, and comparison of designs performance at different infrared wavelengths.

The interface between a metal and a lightly doped semiconductor is well known to form a Schottky barrier that has special electrical characteristics. Such property has been widely used in designing Schottky based photodetectors that exploit the excitation of SPP or are integrated with resonant cavities [5]. The interface resulted when a metal film is deposited on top of a semiconductor is known as a Schottky contact.

3.1 Overview of Schottky Photodetectors

For many years, Schottky barrier diodes have been used in detection applications which are below the band gap energy of the semiconductor [5]. They are commonly used as a long wavelength optical detectors [44]. Unlike the conventional diodes which operate with a semiconductor-semiconductor junction, Schottky barrier diodes operate with a metal-semiconductor junction which forms between a metal and a semiconductor [58].

A typical Schottky barrier detector is sketched on figure 3.1 with the semiconductor being Silicon and the metal being gold. The radiation is applied perpendicularly to the metal surface (top illumination) and the energy is absorbed by the metal [5, 13, 19].

The absorbed photons excite charge carriers in the metal leading them to cross over the Schottky barrier where they will be collected as photocurrent after being swept by an applied voltage bias [5, 19]. This internal photoemission process is displayed in the energy band diagram shown on Figure 3.2, ref [13].

3.1.1 The detection Mechanisms of Schottky Photodetectors

Generally, there are two photodetection mechanisms which are usually implemented for the generation of photocurrent in Schottky photodetectors. Below is a description of both mechanisms:

3.1.1.1 The Electron Hole Pair Creation (EHP) of Schottky Photodetectors

This mechanism is demonstrated on figure 3.2 (a) where a radiation of energy ($h\nu$) greater than the bandgap energy of Si (E_g) gets absorbed by the structure and the result is creating electron- hole pairs ($EHPs$) in Si. The (EHP) mechanism is subdivided into four steps [4]:

1. The optical absorption of energy $h\nu > E_g$ and creation of $EHPs$.

2. The separation of $EHPs$.

3. Transport across the absorption region under reverse bias.

4. collecting of $EHPs$ into photocurrent at the device contacts.

3.1.1.2 The Internal Photoemission Process of Schottky Photodetectors

The electron hole pair creation of Schottky photodetecotrs that is shown on figure 3.2 (a) is one mechanism of photodetection. Another mechanism is the internal photoemission process of Schottky photodetectors. It is somehow similar to the photo-electric effect but occurs at an interface between two materials whereas the photo-electric effect occurs at

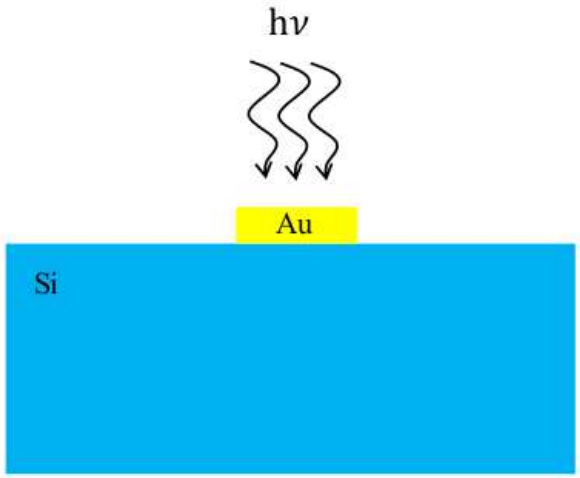

Figure 3.1: An asymmetrically cladded Schottky barrier detector with the use of front-end illumination.

a metal/vacuum interface [4].

This detection mechanism is the one used to model the detector studied in this theoretical research, it is depicted on figure 3.2 (*b*). The internal photoemission process can be divided into three steps:

For n-type silicon, the process is as follows [13, 19]:

1. Photoexcitation: when an electron in the metal in a state below E_F absorbs an incident photon of energy $h\nu$, it can move to a state above E_F and leave behind it a free hole. The energy gained by the electron is usually referred to as its excess energy.

2. Transport: When the hot electron gains enough energy and moves towards the metal-semiconductor interface.

3. Emission: When the hot electron's energy is larger than the Schottky barrier energy, it can overcome the Schottky barrier and be emitted into the semiconductor.

When a number of hot electrons are emitted over the Schottky barrier, they will be

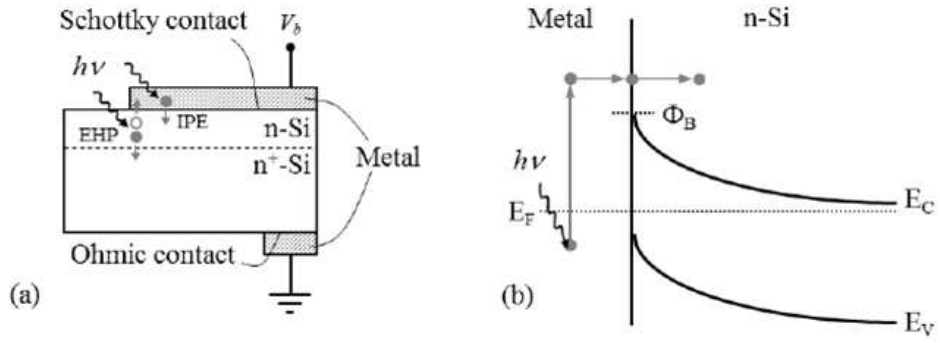

Figure 3.2: (a) An asymmetrically cladded Schottky detector on n-doped Silicon. The structure is employing a front end illumination by a beam of photon energy($h\nu$). The filled and the unfilled circles represent the electrons and holes, respectively.(b) An energy band diagram of a Schottky barrier displaying the 3-steps involved in the photoemission process where E_F is the Fermi level, E_V and E_C are the valence band and the conduction band edges, respectively.ϕ_B is the Schottky barrier height. Figure is shown as published in [13].

swept by an applied voltage bias and then collected as photocurrent at another terminal [5, 18, 19].

The internal photoemission mechanism allows for detection of energies that are below the band gap of the semiconductor $\phi_B < h\nu < E_g$ [13]. This mechanism is of interest especially for devices incorporating Silicon which has a widespread use in detection applications at infrared optical wavelengths (1310 and 1550nm) [44].

3.1.1.2.1 The Internal Photoemission of Schottky Photodetectors Integrated into Very Thin Metal Stipes Schottky Photodetectors integrated into a thin metal stripe can allow for more carrier escape than those integrated into thick metals. The quantum efficiency for a thin metal stripe can get significantly enhanced due to the multiple reflections of excited carriers inside the thin metal [18].

Although a very thin metal film can enhance the internal photoemission and thus, the quantum efficiency through multiple reflections, it absorbs less optical power which affects negatively the enhancement of carrier emission [44]. Integrating the detector with an optical cavity or merging the detector with a dielectric waveguide can both increase the optical absorption. Such techniques were investigated in [59, 60, 61, 62]. Other techniques which have been used to enhance the Schottky detector response involve coupling of incident light into the $SPPs$ propagating along the metal film which is the method

adopted in this thesis work. The same technique was used in [63, 64, 65, 34] with an increase in responsivity as well as internal photoemission being reported.

3.1.2 The Schottky Barrier Height ϕ_B

The Schottky barrier height ϕ_B is largely dependant on the work function of the metal W and the electron affinity of the semiconductor χ but for p-type semiconductor, it will also depend on E_g [19, 5, 28]. Additionally, recent investigations have led to a sharp dependence of the Schottky barrier height on the atomic structure of the metal/silicon interface [66].

For an $n-type$ semiconductor, $\phi_B = W - \chi$ and, for $p-type$ semiconductor, $\phi_B = E_g - (W - \chi)$ where W is the work function of the metal, χ is the electron affinity of the semiconductor, and E_g is the band-gap energy of the semiconductor [19].

The Schottky barrier energy is evaluated relative to E_F which, in the metal, refers to the Fermi energy and, in the semiconductor, refers to the Fermi level [19]. This Schottky barrier energy or height is lower for detectors with gold structures than detectors with Aluminium structures. For example, it is 0.34 and 0.8 eV for $Au/p-Si$ and $Au/n-Si$ while it is 0.58 and 0.72 eV for $Al/p-Si$ and $Al/n-Si$, respectively [4]. A real metal-semiconductor contact may develop surface states which cause the experimentally measured Schottky barrier energies to be different from the theoretically expected values [19].

The Schottky barrier energy ϕ_B can be related to the external quantum efficiency η_e through the following relation [19]:

$$\sqrt{\eta_e h\nu} = \sqrt{C}(h\nu - \phi_B) \tag{3.1}$$

A plot of $\sqrt{\eta_e h\nu}$ versus $h\nu$ is linear with the slope being equal to $\sqrt{C}$, where C is the quantum efficiency coefficient; known also as Schottky emission coefficient. The x-intercept occurs when $\eta_e = 0$ and it is equivalent to the Schottky barrier height ϕ_B [19]. Such plots are refereed to as Fowler plots. From Fowler theory, it is concluded that $\eta_e \propto (h\nu - W)^2$, where W is the work function of the metal [67].

Many experiments demonstrated the dependency of Schottky barrier height on the fabrication process [5]. Reducing the Schottky contact area plays an important role in reducing the dark current, thus a nano-structured Schottky photodetector can enhance the performance of Schottky photodetectors and their integration with nano-plasmonics as well as nano-photonics structures [5, 18, 19]. Such device is useful for power monitoring applications and short-reach optical interconnects [5, 18].

3.1.3 Silicon Based Schottky Photodetectors

A Shottky barrier diode has been used for many years for detection applications at or near infrared wavelengths (below the bandgap energy of the semiconductor) [5, 18]. Shottky barrier detectors with asymmetric structure can be easily fabricated and integrated with silicon based electronic devices. Due to the low cost and fast response of Silicon, there has been a great interest in designing Silicon based photodetectors [28]. These advantages allowed for monolithic integration of detectors [28]. Schottky barrier detectors integrated into symmetric metal stripes are known to have high performance but they are more difficult to integrate than those of the asymmetric metal stripes [19].

Schottky photodetectors with $p-type$ Silicon are usually used due to the low Schottky barriers which allow for high quantum efficiencies and thus, larger photoresponse for the diode and detection at longer wavelengths [19, 44]. However, they must operate at cryogenic temperatures in order to avoid a large dark current [19].

In [68], a p-type silicon is used as the active semiconductor with a carbon nano-tube (CNT) film acting as the transparent metal. The device exhibited a large photocurrent to dark current ratio and the responsivity was reported to be high, around $0.1A/W$, because of the high transmittance of the carbon nano-tube film. And, in [69], a Silicon resonant cavity enhanced (RCE) photodetector which is based on the internal photoemission effect at the wavelength $1.55\mu m$ was characterized and fabricated. A reasonable improvement in responsivity was measured with this device.

Other materials have also been used to construct Schottky photodetectors as in the SPP waveguide detector shown in Chapter 1, figure 1.10. However, the use of Si in

photodetector devices is of vigorous current interest due to its low cost, fast response, and wide use for detection at infrared optical communications wavelengths.

3.1.4 Surface Plasmon Schottky Photodetectors

At optical frequencies, some dielectrics like Silicon and some noble metals like Au tend to have positive and negative real part of permittivity, respectively [5, 11, 19]. In this case, Schottky contact which is the interface between Au and Silicon can support the propagation of bound SPP modes [5, 19]. The SPP is generated through the coupling between a TM polarized electromagnetic wave and electron oscillations in the metal [9, 7]. The electric field component which is perpendicular to the direction of propagation as well as the planar interface is the $SPPs$ dominant field and it has an exponentially decaying distribution that is extending from the metal stripe into the dielectric claddings [5, 9, 18, 19].

An SPP detector is of a great advantage to the field of integrated optics. It is known to combine a metallic structure which supports the propagation of surface plasmons with a photodetection structure and operates with internal photoemission or electron hole pair creation. Such detectors are useful in many applications including photovoltaic solar energy conversion, biochemical sensing, low noise high speed detection, near-and mid-infrared imaging, and single plasmon detection [4]. The importance of those detectors lies behind the sub-wavelength confinement property of surface plasmons and their ability to resonate on very small metals [4].

Surface plasmon based detectors have the advantage of polarization and angular selectivity. Moreover, they produce enhanced photoresponse and speed [4].

Since many metals can support the propagation of $SPPs$ at optical wavelengths, and due to the variety of detection materials and schemes, many photodetectors with different architectures and designs were fabricated to date [4].

The metal-dielectric structure which supports $SPPs$ can be metal grating, metal nanoparticles, antennas or planar arrangements of metals [4]. Those examples were discussed in more detail in Chapter 1.

With the use of surface plasmon polaritons, small detectors that are tempting for many recent applications can be designed.

3.2 End fire coupling Efficiency

One method of exciting an SPP mode is to let the incident fibre light that is used to excite and couple to the SPP mode to be TM oriented and aligned to the bottom center of the metal stripe along the facet normal. The emerged field is then assumed to have a Gaussian-like field distribution that is governed by its spot size [5]. This method is known as the end-fire coupling technique. The coupling efficiency is calculated through the following equation [47]:

$$\gamma_c = |C|^2$$

Where the coupling factor C is given by:

$$C = \frac{\iint_{-\infty}^{\infty} E_{y1}(x,y)E_{y2}^*(x,y)\,\mathrm{d}A}{\sqrt{\left(\iint_{-\infty}^{\infty} E_{y1}(x,y)E_{y1}^*(x,y)\,\mathrm{d}A\right)\left(\iint_{-\infty}^{\infty} E_{y2}(x,y)E_{y2}^*(x,y)\,\mathrm{d}A\right)}} \tag{3.2}$$

where E_{y1} is the $SPP's$ electric field in y-direction and E_{y2} is the fibre's electric field in y-direction. The total overlap integral between the two fields is calculated in the numerator and the term in the denominator is only used as a normalization factor in order to get γ_c value in the range between 0 and 1.

Figure 3.3 shows a sketch of an asymmetric SPP waveguide detector composed of a thin and narrow gold stripe placed on $n-Si$ substrate with air on top being the superstrate. The metal stripe sketched has a width of $100nm$ and a thickness of $20nm$. In this structure, the interface between the metal and Si forms a Schottky contact which has rectifying electrical characteristics. The fundamental mode (as_b^0) that is supported by this structure is localized to the metal/Si interface and propagates thereon with strong

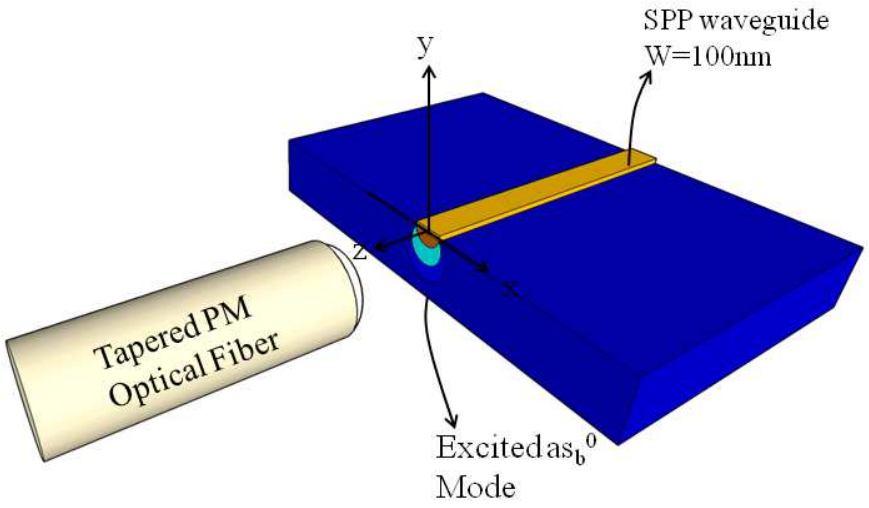

Figure 3.3: A close-up view of the alignment of a tapered PM optical fiber with an SPP waveguide which is also a Schottky photodetector structure.

absorption. The absorption in the metal creates hot carriers inside the metal and along the interface (the Schottky Contact). Carriers , whose energy get higher than the Schottky barrier height, cross the barrier and become collected as photocurrent. This process is known as the internal photoemission process (IPE). The supported fundamental mode (as_b^0), as seen on figure 3.3, is being excited via coupling to a tapered polarizatiom-maintaining single mode optical fiber ($PM-SMF$) at wavelengths below the bandgap of Si [4].

The optical fibers used to couple to the as_b^0 are characterized by their transverse field component Ey which is given by [47]:

$$E_y = exp\left[\frac{-x^2 - \left(y - \frac{t}{2}\right)^2}{r_f^2}\right] \tag{3.3}$$

where r_f is the mode field radius and it is given by:

$$r_f = a\left(0.65 + \frac{1.619}{V^{3/2}} + \frac{2.879}{V^6}\right) \tag{3.4}$$

and, the parameter V is given by:

$$V = \frac{2\pi a}{\lambda_0} NA \tag{3.5}$$

where (a) and (NA) are the fiber core radius and the numerical aperture of standard single mode fiber $(SMF - 28)$. The value of a is $4.1\mu m$ and the value of NA is 0.12.

3.2.1 Coupling of Asymmetric Bound Schottky SPP Modes with Single Mode Optical Fibers

In general, using end-fire excitation techniques, the fundamental mode supported by the symmetric stripe waveguides, denoted as (ss_b^0), or the asymmetric stripe waveguides, denoted as (as_b^0) can be excited using a tapered optical fiber. With asymmetric stripe waveguides, the fiber is TM aligned and placed incident to the bottom center of the metal stripe as shown on figure 3.3. The coupling efficiency is higher when using the (ss_b^0) mode supported by the symmetric waveguides. This is due to the Gaussian like shape for its field distribution. On the other hand, P.Berini *et al.*, have proved that 18% of overlap can be achieved when using a tapered polarization-maintaining single-mode optical fibre $TPM - SMF$ of waist radius $w_0 = 1.3\mu m$ with a fundamental mode of Schottky contact (an asymmetric SPP mode) supported by a $135nm$ thick and $1.5\mu m$ wide Au stripe deposited on $p - si$ at $\lambda_0 = 1550nm$ [36]. The tapered $PM - SMF$ was scanned over the end facet of the waveguide, as seen on figure 3.3, using a piezoelectric nanopositioner. The reported photocurrent map was largest when the fiber was perfectly aligned with the bottom center of the stripe. This is where the maximum overlap between the incident beam and the as_b^0 mode occurs.

In this thesis, the as_b^0 mode supported by an asymmetric Schottky contact structure, having a gold stripe of finite width (maximum width $100nm$ and maximum thickness $50nm$) as the metal, was excited by two PM (polarization maintaining) tapered optical fibres. The spot sizes of the fibers are 10% smaller at the wavelength $\lambda_0 = 1310nm$ than the wavelength $\lambda_0 = 1550nm$.

The power coupling efficiency γ_c was studied as a function of variation in the as_b^0 mode size which varies for different stripe thicknesses and widths. The dimensions of the metal stripe were varied to track the best coupling efficiency possible between the fibre mode and the SPP mode.

A previous theoretical work done by Akbari [34] showed that the best coupling efficiency is achieved when the as_b^0 mode has the most Gaussian-like shape for its field distribution. This usually occurs when the stripe width approaches the spot size of the incident field and when its thickness is large enough ($> 80nm$), leading the mode to have less confinement and a large distribution beneath the stripe.

3.2.2 Variation of Coupling efficiency with waveguide dimensions (t, w) at $\lambda_0 = 1310$ and $1550nm$

Equation 3.2 shows clearly the dependency of coupling on the waveguide dimensions. As the mode evolves with varying stripe's thickness and width, the overlap integral changes. This change of overlap causes a change in the photocurrent I_{ph}, responsivity R, and minimum detectable power (S_{min}) of the detector as they strongly depend on the coupling efficiency γ_c. Since this evolution of the waveguide's mode with stripe dimensions (t, w) became clearly understood, many promising structures can be designed to enhance a photodetector performance. This involves optimizing some of the photodetector parameters such as its dark current (I_{dark}), minimum detectable power (S_{min}) or its responsivity (R).

Figure 3.4 plots the coupling efficiency γ_c as a function of stripe thickness t showing that it increases with t until it reaches a maximum value of $\sim 2.7\%$ at $t = 50nm$ and $\lambda_0 = 1310nm$. This coupling efficiency value gets increased up to $\sim 8\%$ at $\lambda_0 = 1550nm$. Similarly, the coupling efficiency γ_c as a function of stripe width w increases with w but with a slightly different trend. The increase of coupling efficiency is associated with the

increase in mode confinement and localization of the SPP mode along the metal/silicon interface. As the mode profile tends to have a lobed distribution along the bottom interface, the coupling efficiency increases. However, as the mode profile gets strongly confined to the corners of the metal stripe (at small t), the coupling efficiency decreases.

The mode profile acquires a Gaussian-like field distribution as the metal extends in width ($w \gg t$) such as the range of structures investigated by Akbari in [5]. The as_b^0 mode field extends into the silicon substrate as the metal increases in thickness, leading to a higher coupling efficiency value of this mode into an optical fiber mode.

Asymmetric metal stripes support many higher order modes but their coupling into optical fibers is almost negligible, thus only the coupling of the fundamental mode as_b^0 is considered.

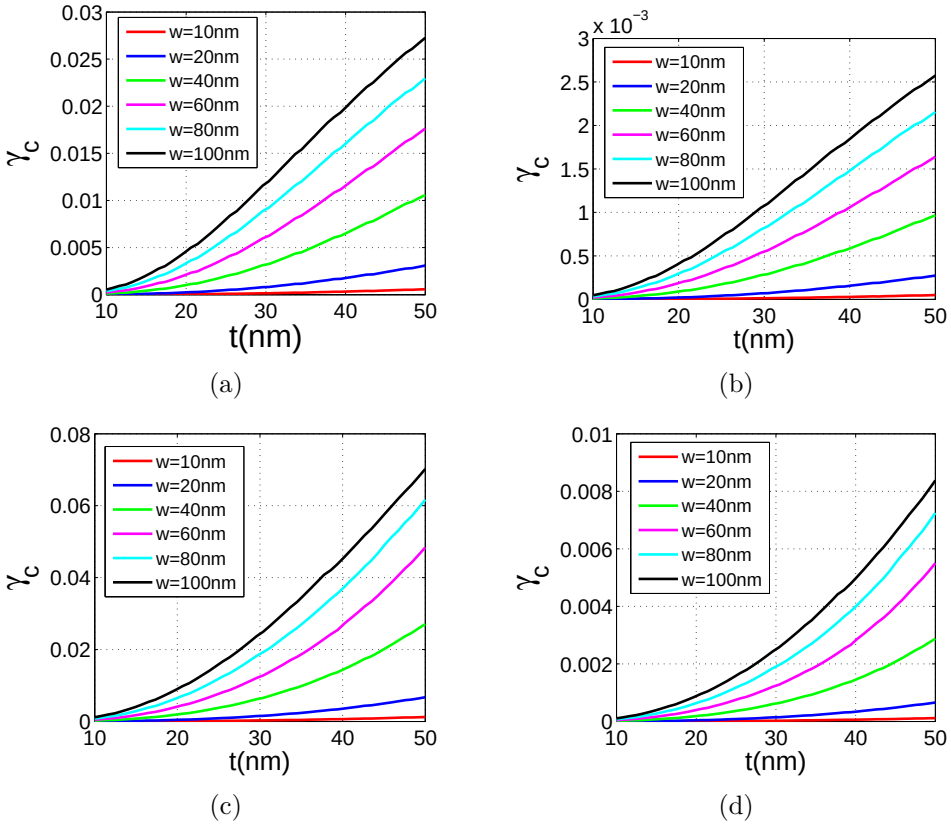

Figure 3.4: Coupling efficiency into the as_b^0 mode as a function of stripe thickness for a Au/Si Schottky photodetector .$(a), (b)$ two tapered polarization-maintaining single-mode optical fibres $TPM - SMF$ having spot sizes of $\sim 2.25\mu m$ and $9.129\mu m$, respectively at $\lambda_0 = 1310nm$ were used to excite the as_b^0 SPP Schottky mode via end-fire coupling.$(c), (d)$ two tapered polarization-maintaining single-mode optical fibres $TPM - SMF$ having spot sizes of $\sim 2.5\mu m$ and $10.183\mu m$ at $\lambda_0 = 1550nm$ were used to excite the as_b^0 SPP Schottky mode via end-fire coupling Techniques.

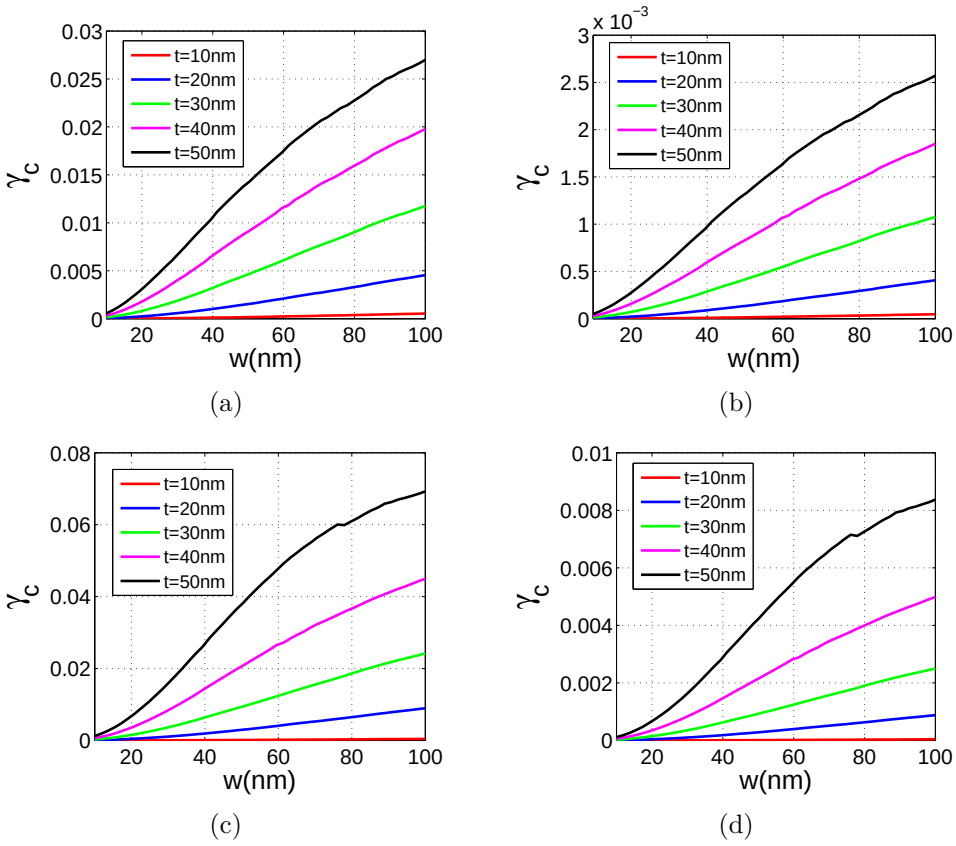

Figure 3.5: Coupling efficiency into the as_b^0 mode as a function of stripe width for a Au/Si Schottky photodetector .$(a), (b)$ two tapered polarization-maintaining single-mode optical fibres $TPM - SMF$ having spot sizes of $\sim 2.25\mu m$ and $9.129\mu m$ at $\lambda_0 = 1310nm$ were used to excite the as_b^0 SPP Schottky mode via end-fire coupling.$(c), (d)$ two tapered polarization-maintaining single-mode optical fibres $TPM - SMF$ having spot sizes of $\sim 2.5\mu m$ and $10.183\mu m$, respectively at $\lambda_0 = 1550nm$ were used to excite the as_b^0 SPP Schottky mode via end-fire coupling Techniques.

Figures 3.4, 3.5 show that the highest coupling efficiency is always achieved for the highest stripe's thickness and width which agrees with the results produced by Akbari in [5]. That is mainly because the field evolves from being localized to the metal corners to having a single lobed distribution along and beneath the stripe.

By looking at the data produced on figures 3.4, 3.5, we can say that the maximum coupling efficiency is acquired when exciting the fundamental mode as_b^0 that is supported by a $50nm$ thick and $100nm$ wide Au stripe by an optical power of an optical fiber having $2.5\mu m$ spot size at the wavelength $1550nm$.

3.3 Photodetection using a tiny Schottky mode

Nano-structuring the metal used in the waveguide was known to be useful in enhancing the field around the metal. Thus, the guided mode can get enhanced and hence, the detection can be improved. In this thesis, some Schottky modes supported by gold metal stripes having nano-structured dimensions were used to detect the mode of a single mode optical fibre through calculations of the overlap factor C between the transverse spatial distribution of the guided SPP mode Ey_1 and the transverse spatial distribution of the optical fibre mode Ey_2 using equation 3.2.

A metal with tiny thickness and width can be thought of a Dirac delta function. A review of the main properties of this function is discussed in appendix C, and the theoretical expectations of the overlap integral between a Dirac function and another function of larger field distribution are discussed in the following subsection.

3.3.1 The fundamental SPP mode as_b^0 as a delta function

The SPP mode supported by a tiny metal was used to play the role of Dirac function. For example, this tiny mode field was used to scan other larger mode fields like optical fiber fields, and the results were expected to satisfy equations C.1, C.4, C.9 assuming the tiny (SPP) mode to act like a Dirac. The technique is based on calculating the overlap integral between the transverse field component (E_y) of this tiny (SPP) mode and the transverse field component (E_y) of some other larger field modes like optical fibers modes at two different operating wavelengths $1310nm$ and $1550nm$ using equation 3.2.

Throughout this research, the optical fiber is characterized by its E_y field distribution which is modelled as a simple Gaussian distribution centred on the excited waveguide. The transverse field component of the fiber is given by equation 3.3. The spot size of the fiber is $2.5\mu m$ at the wavelength $1550nm$, it is 10% smaller at the wavelength $1310nm$.

When a function that is not a Dirac function is swept by a Dirac function, the result then is the value of the function at the location of the Dirac delta function. As a result, the coupling efficiency between the SPP mode field supported by the tiny metal stripe and a tapered fibre's mode field will give the fibre mode at the location of the tiny SPP mode. The concept can be explained mathematically as follows:

If $E^*_{y2}(x_2, y_2)$ in equation 3.2; which is the conjugate of the $SPP's$ electric field in y-direction at the position (x_2, y_2); was a Dirac, then the result of the overlap integral will be $E_{y1}(x_2, y_2)$. It is the value of E_{y1} at the location of the Dirac delta function $E_{y2}(x_2, y_2)$. This can be represented mathematically as follows:

If:

$$I_1 = \sqrt{\iint_{A_\infty} E_{y1}.E^*_{y1}\,\mathrm{d}A} \tag{3.6}$$

and,

$$I_2 = \sqrt{\iint_{A_\infty} E_{y2}.E^*_{y2}\,\mathrm{d}A} \tag{3.7}$$

then, using equations 3.6 and 3.7, equation 3.2 becomes:

$$C = \iint_{A_\infty} \frac{E_{y1}}{I_1}.\frac{E^*_{y2}}{I_2}\,\mathrm{d}A \tag{3.8}$$

and if:

$$\delta(x_2, y_2) = \frac{E^*_{y2}(x_2, y_2)\,\mathrm{d}A}{I_2} \tag{3.9}$$

then, the overlap factor C in equation 3.2 becomes:

$$C(x_2, y_2) = \frac{E_{y1}(x_2, y_2)}{I_1} \tag{3.10}$$

where: (E_{y1}) is the transverse component of the fiber field, (I_1) is its normalization term.

3.4 The Overlap Integral as a function of Position Sweeps

The best coupling efficiency can only be produced for the fundamental as_b^0 mode. Coupling efficiencies for higher order modes are almost negligible when compared to the coupling efficiencies of the as_b^0 mode [5]. The coupling efficiency produced for the fundamental mode of a Schottky photodetector or a finite width asymmetric waveguide is not as high as the coupling produced for the fundamental mode supported by a symmetric finite width waveguide. That is mainly because of the horizontally asymmetric nature of the modes supported by the asymmetric structure.

Maps of overlap and photocurrent were produced for two waveguides at two operating wavelength $1310nm$ and $1550nm$. Additional Maps of overlap were also produced for the coupling between a fundamental mode as_b^0 of Schottky photodetector with itself. A Schottky photodetector was used to detect another identical one of exact waveguide dimensions, exact mode, and exact wavelength. Such calculations were performed for the first time to make sure a centred overlap map is achieved, and thus gain confidence in the overlap maps resulted for the as_b^0 mode overlap with an optical fiber.

3.4.1 The Schottky Photodetector Modes Supported by asymmetric finite-Width Waveguides

Generally, the asymmetrically cladded metal stripes support the propagation of several SPP modes. However, those modes have different propagation properties as well as different field distributions. The first three bound modes were studied by Akbari in [5] and [34] using Au and Al stripes deposited on $n - Si$ and $p - Si$ over a wide range of stripe thickness and width. Those three modes were of interest because they appeared to be strongly localized to the metal/Si interface which is also known as the Schottky barrier. The smallest stripe thickness and width investigated by Akbari is $10nm$ and

$2.5\mu m$, respectively at the optical wavelengths $1310nm$ and $1550nm$.

In this thesis, only one mode is of interest which is the fundamental mode as_b^0 supported by an Au metal stripe over a range of thickness (t) and width (w). The Au stripe is characterized by its relative permittivity value which varies for each optical wavelength used while Si is characterized by its refractive index due to its negligible absorption at the wavelengths of interest. An interpolation technique of some refractive index data of the materials used to model the waveguide structure was implemented to estimate and find some unavailable values of optical parameters at the wavelengths of interest[5].

A study of the fundamental mode's behaviour for different stripe dimensions was needed in order to understand the produced overlap and coupling results. The fundamental mode of two waveguide structures was used to couple to tapered polarization maintaining single mode optical fibers. The waveguides selected are for an Au stripe deposited on Silicon substrate and covered by air. The Au stripe is used with $10nm$ of thickness and width for the first waveguide and $50nm$ of thickness with $100nm$ of width for the second waveguide.

Unlike the infinite width SPP waveguides, which allow for only one dimensional field confinement in the vertical direction [9], finite width SPP waveguides, have mode confinement in two dimensions and field varies in the vertical as well as the lateral direction [20]. This property made the finite width SPP waveguides to be of important use in integrated optics technology. Figures 3.6,3.7,3.8, 3.9, for the real and imaginary parts of the as_b^0 mode, indicate this two dimensional mode confinement property of such waveguides. They also indicate the fact that modes are more confined at the wavelength $1310nm$ than $1550nm$.

The Schottky mode profile tends to be lobed underneath the stripe as the stripe expands in width. That is due to the fact that the real part of effective index $Re(n_{eff})$ of the mode gets smaller at larger stripe width w, leading the mode field to expand over a larger area and acquire a lobe-like distribution that extends into the cladding of higher refractive index (Si). Thus, when overlapping with a fiber field, the higher overlap is achieved at the highest width as shown on figures 3.4,3.5. The overlap is higher at the wavelength $1550nm$ as the mode has smaller real effective index value at this wavelength and thus, its field extends over a larger area than the wavelength $1310nm$. The results

produced by Akbari [5], showed that the optimal excitation of the as_b^0 mode is achieved for a waveguide thickness higher than $80nm$ and for a waveguide width between $2.5\mu m$ and $3.5\mu m$. This was explained by the fact that the stripe width $2.5\mu m$ is identical to the spot size of the incident fiber field and the fact that the mode confinement is less at a large t which causes a large lobed distribution beneath the stripe.

With the use of equation 3.2, those two Schottky modes are used to overlap with the modes of tapered polarization maintaining single mode fibers as a function of position.

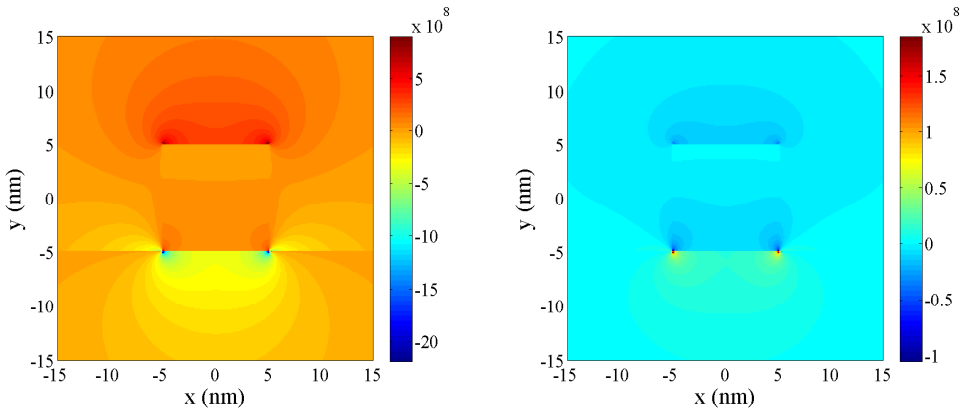

Figure 3.6: A close up view of the real (a) and imaginary (b) part of the transverse field distribution (E_y) for the as_b^0 mode supported by an Au metal film of $10nm$ thickness and $10nm$ width, surrounded by air on top and Si at the bottom at $\lambda_0 = 1310nm$.

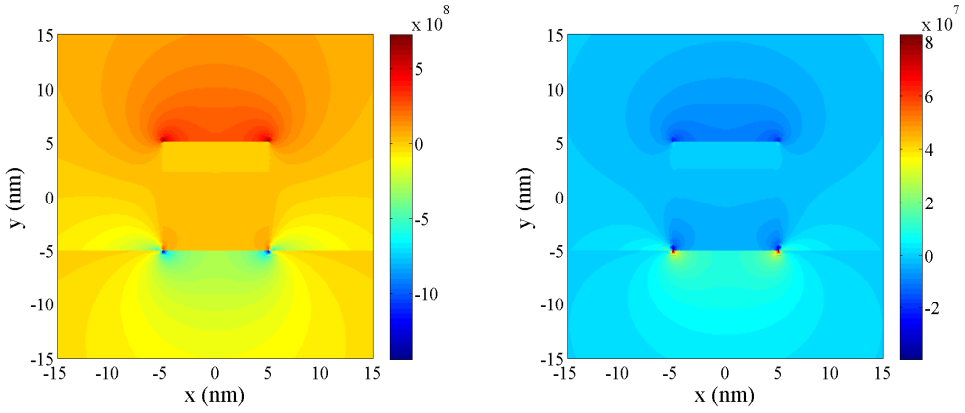

(a) (b)

Figure 3.7: A close up view of the real (a) and imaginary (b) part of the transverse field distribution (E_y) for the as_b^0 mode supported by an Au metal film of $10nm$ thickness and $10nm$ width, surrounded by air on top and Si at the bottom at $\lambda_0 = 1550nm$.

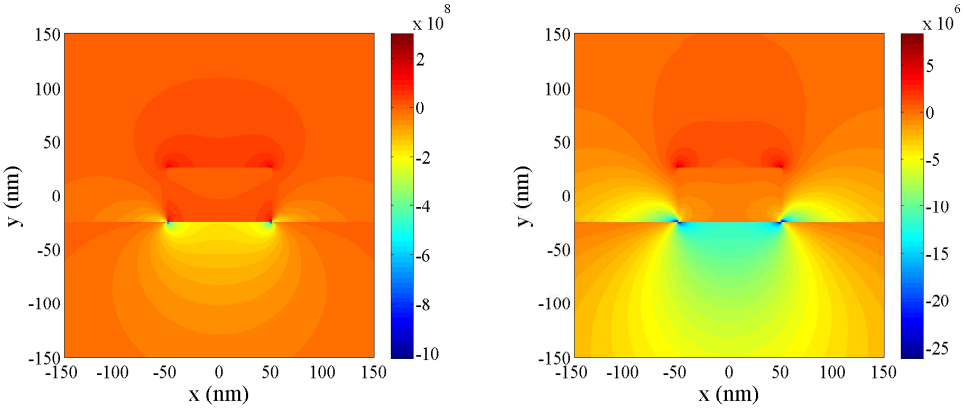

(a) (b)

Figure 3.8: A close up view of the real (a) and imaginary (b) part of the transverse field distribution (E_y) for the as_b^0 mode supported by an Au metal film of $50nm$ thickness and $100nm$ width, surrounded by air on top and Si at the bottom at $\lambda_0 = 1310nm$.

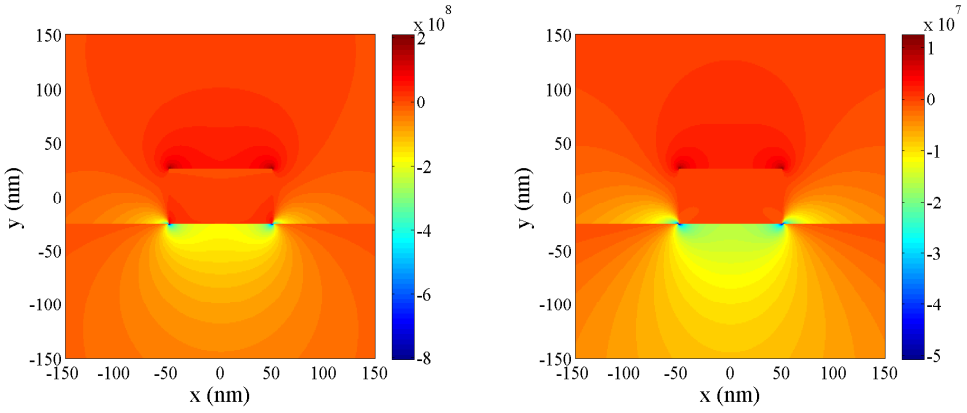

Figure 3.9: A close up view of the real (a) and imaginary (b) part of the transverse field distribution (E_y) for the as_b^0 mode supported by an Au metal film of $50nm$ thickness and $100nm$ width, surrounded by air on top and Si at the bottom at $\lambda_0 = 1550nm$.

3.4.2 The Overlap Integral between Two Identical SPP Photodetectors as a function of position

Overlap integral calculations were implemented between two identical as_b^0 modes supported by identical waveguide structure which are constructed with the same materials at the same operating wavelength. Such calculations were done for the first time. In the results shown on figures 3.10, 3.11, One photodetector was used to scan another identical fixed detector and a centred overlap map was achieved. Figure 3.10 is the absolute of the overlap resulted from two photodetectors having Au metal stripes of $50nm$ thickness and $100nm$ width. And, figure 3.11 is the the absolute of the overlap resulted from two photodetectors having Au metal stripes of $10nm$ thickness and $10nm$ width.

As one detector scans the other, the overlap integral between their transverse field components E_y is calculated using equation 3.2. A gap where no overlap exists was generated above and below the maximum overlap. It is where a negative field from one detector cancels out with a positive field from the other detector. This is clearly observed with the scan of the two small detectors as the supported mode has a higher real effective index and its field does not extend in the Si substrate as much as it does for the two big detectors. For the two big photodetector's overlap, the gap is barely visible due to the low real effective index and to the large mode field supported by both detectors. In more details, as one detector scan the other and changes its position, there is always a

field to overlap with which results in a continuous overlap expanding over a large area.

The overlap maps of the detectors operating at $1550nm$, as seen on figures 3.10b, 3.11b, expand over a greater area due to the fact that the modes have less real effective index at this wavelength, thus more expanded mode field into the Si substrate.

The calculations were performed with $1nm$ step size for both detectors at both operating wavelengths. The results were convincing and a maximum overlap of 1 was reached.

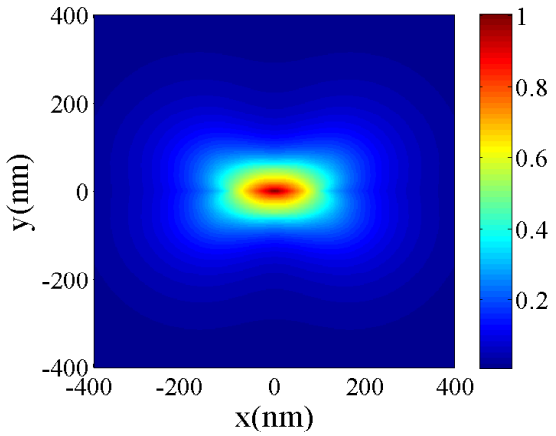

(a)

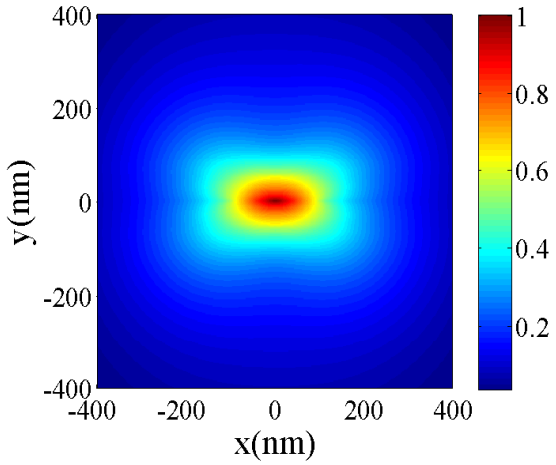

(b)

Figure 3.10: The absolute of the overlap between two identical fundamental (as_b^0) Schottky modes. Both supported by a metal stripe of $50nm$ thickness and $100nm$ width at (a) $\lambda_0 = 1310nm$ and (b) $\lambda_0 = 1550nm$.

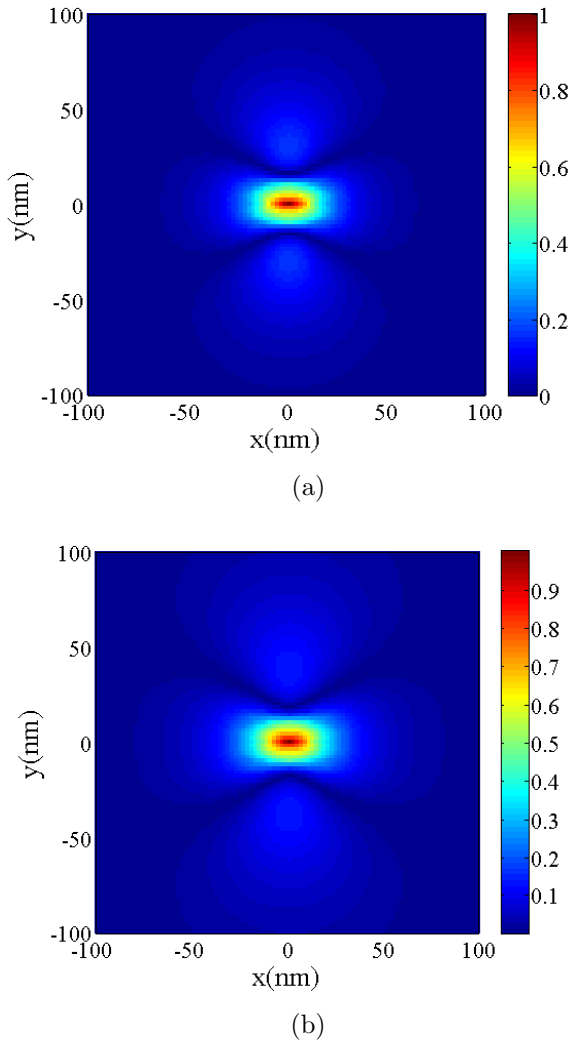

Figure 3.11: The absolute of the overlap between two identical fundamental (as_b^0) Schottky modes. Both supported by a metal stripe of $10nm$ thickness and $10nm$ width at (a) $\lambda_0 = 1310nm$ and (b) $\lambda_0 = 1550nm$.

3.4.3 The Overlap Integral Between a Schottky Photodetector Mode and an optical fiber mode as a function of Position

Using the two Schottky modes presented in the previous section at the wavelengths $1310nm$ and $1550nm$, the mode of a $PM - SMF$ was scanned and detected through an overlap integration process which was defined in equation 3.2. Generally, the fiber must be TM oriented and aligned with the bottom centre of the metal stripe to achieve a maximum coupling efficiency. However, since a position sweep is needed, the fiber was fixed at the centre of a $2d$ domain which measures $5\mu m$ wide and $5\mu m$ high and the

Schottky photodetector mode was moving over and scanning the fiber domain. As the two selected photodetector modes were very small compared to the mode of the optical fiber, only a small rectangular area from the fiber domain identical in size to the the domain of the Schottky mode was used in the calculations. Each time the detector changes its position, it gets multiplied by a new rectangular piece of the TM aligned fiber field and the result of each multiplication is summed to a one complex overlap value placed at the centre of the Schottky detector position. The absolute of all the complex overlap values is then plotted in a $2D$ domain as seen on section C of figures 3.12, 3.13, 3.14, 3.13.

In summary, the highest coupling is achieved for a detector operating at the wavelengths $1550nm$ as the real part of the effective index of the mode is smaller at this wavelength which causes the field to expand more into the Si substrate. Moreover, the higher the thickness and width of the metal used in the detector, the higher the coupling is. This is because the field spreads into the substrate with increasing the metal thickness and gets a large lobed distribution along and beneath the metal with increasing the metal width.

As seen on figure 3.15, the greatest overlap acquired over the range of metal thickness t and width w that are of interest in this research is for a Schottky photodetector integrated into a metal stripe of $50nm$ thickness and $100nm$ width operating at the wavelength $1550nm$.

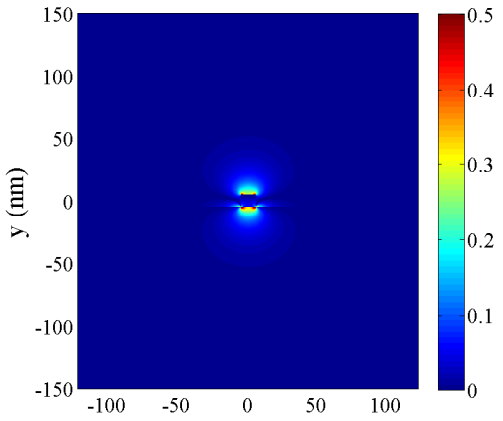

(a)

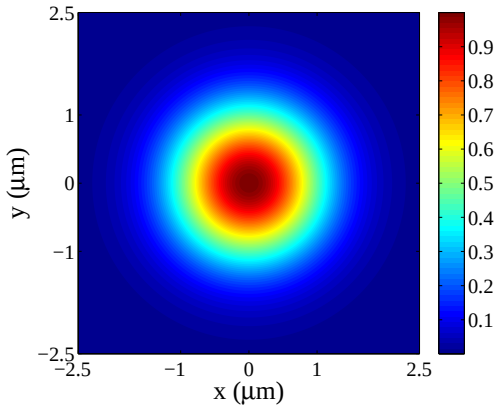

(b)

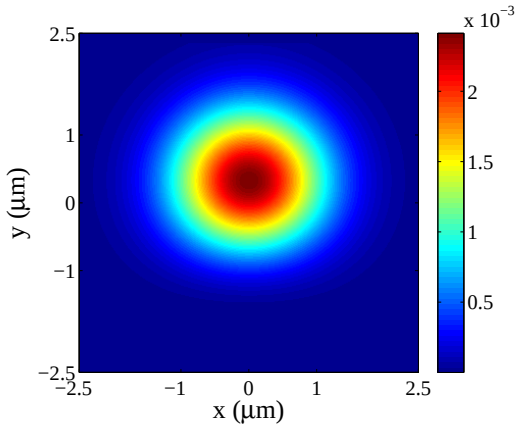

(c)

Figure 3.12: (a) The absolute value of the transverse field distribution (E_y) for the as_b^0 mode supported by an Au metal film of $10nm$ thickness and $10nm$ width, surrounded by air on top and Si at the bottom at $\lambda_0 = 1310nm$.(b) the transverse field distribution (E_y) for an optical fiber having a spot size of $2.25\mu m$ at $\lambda_0 = 1310nm$.(c) the absolute of the overlap between the as_b^0 SPP mode and the fiber mode shown on (a) and (b) , respectively.

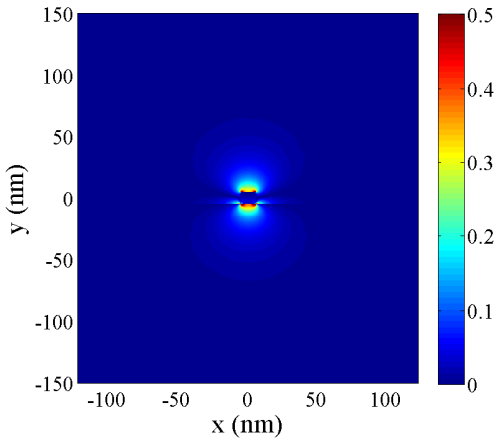

(a)

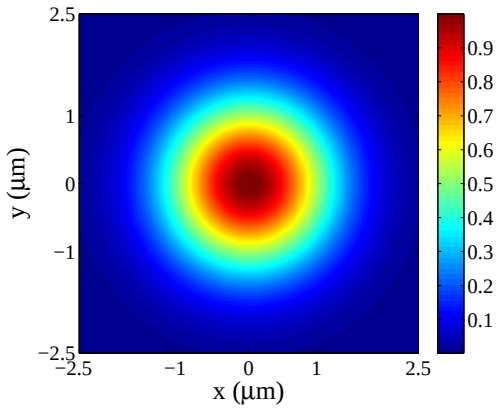

(b)

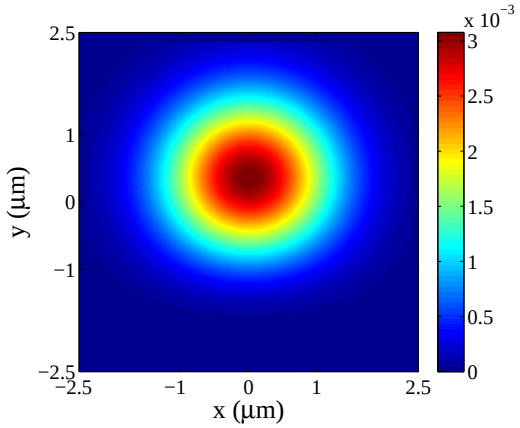

(c)

Figure 3.13: (a) The absolute value of the transverse field distribution (E_y) for the as_b^0 mode supported by an Au metal film of $10nm$ thickness and $10nm$ width, surrounded by air on top and Si at the bottom at $\lambda_0 = 1550nm$.(b) the transverse field distribution (E_y) for an optical fiber having a spot size of $2.5\mu m$ at $\lambda_0 = 1550nm$.(c) the absolute of the overlap between the as_b^0 SPP mode and the fiber mode shown on (a) and (b) , respectively.

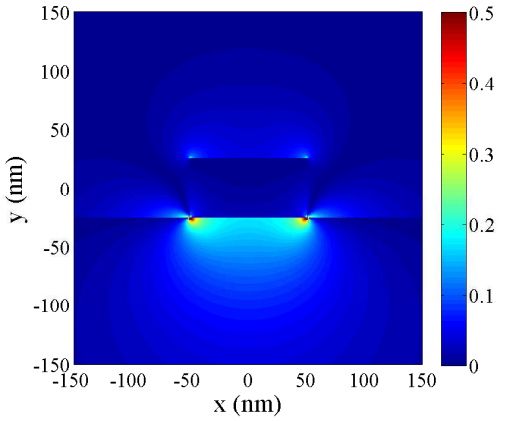

(a)

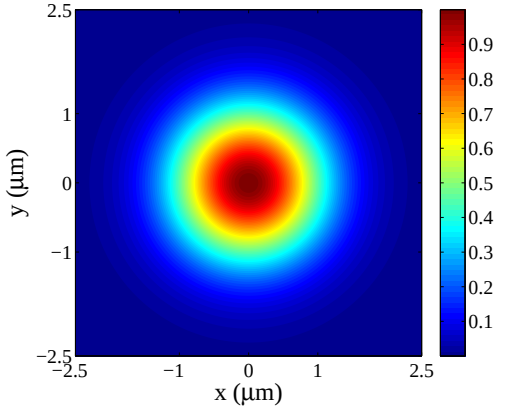

(b)

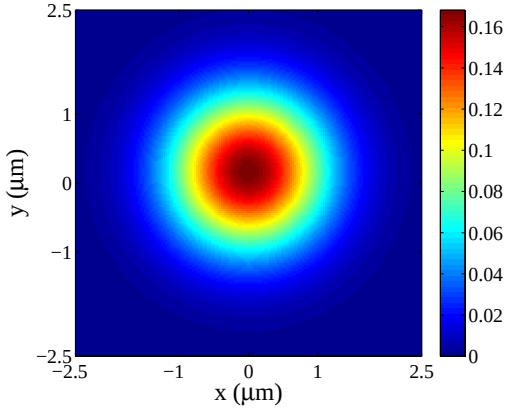

(c)

Figure 3.14: (a) the absolute value of the transverse field distribution (E_y) for the as_b^0 mode supported by an Au metal film of $50nm$ thickness and $100nm$ width, surrounded by air on top and Si at the bottom at $\lambda_0 = 1310nm$.(b) the transverse field distribution (E_y) for an optical fiber having a spot size of $2.25\mu m$ at $\lambda_0 = 1310nm$.(c) the absolute of the overlap between the as_b^0 SPP mode and the fiber mode shown on (a) and (b) , respectively.

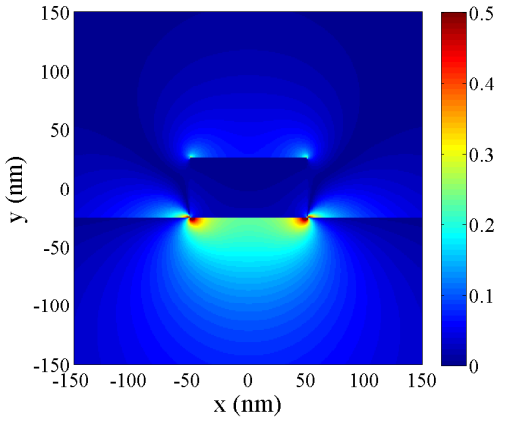

(a)

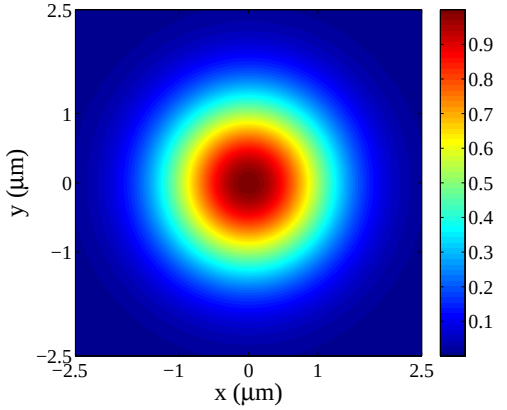

(b)

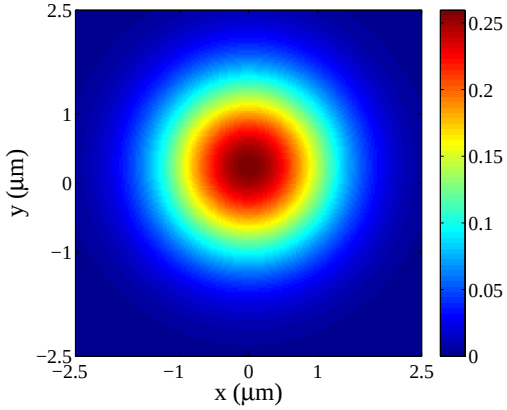

(c)

Figure 3.15: (a) The absolute value of the transverse field distribution (E_y) for the as_b^0 mode supported by an Au metal film of $50nm$ thickness and $100nm$ width, surrounded by air on top and Si at the bottom at $\lambda_0 = 1550nm$.(b) the transverse field distribution (E_y) for an optical fiber having a spot size of $2.5\mu m$ at $\lambda_0 = 1550nm$.(c) the absolute of the overlap between the as_b^0 SPP mode and the fiber mode shown on (a) and (b) , respectively.

Chapter 4

The Performance of The Nano-structured SPP Photodetector

A Schottky nano-photodetector integrated into a metal stripe supported by a Silicon substrate is an attractive device which holds promise for developing and enhancing the Silicon based nano-photonic devices. In this chapter, the performance of a Silicon based photodetector integrated into an asymmetric nano-structured gold stripe was investigated for the fundamental mode as_b^0 at two infrared wavelengths ($1310nm$ and $1550nm$). Testing the performance of the device was done via calculating how much of the input optical power that was coupled into the fundamental mode supported by the stripe is absorbed over the given waveguide length which, in this nano-structured asymmetric structure, was very short due to the high attenuation of the SPP mode. The absorbed power is known to cause excitation of carriers in the metal, leading the excited carriers to cross over the Schottky barrier and be collected as photocurrent under reverse bias in an operation known as the internal photoemission process, asdiscussed in more detail in this chapter.

4.1 The Detector Performance Parameters

The detector performance is evaluated in terms of parameters such as its responsivity, minimum detectable power and dark current. Theoretical predictions of these parameters were made to describe the performance of the nano-structured Schottky SPP detector with an Au stripe deposited on $n-Si$ and $p-Si$ at both 1310 and $1550nm$ optical

wavelengths [19]. The performance strongly depends on η_i, which is a function of the waveguide's thickness t and Schottky barrier height ϕ_B [5]. In addition, the device performance is greatly affected by the coupling efficiency which varies for different waveguide dimensions and operating wavelengths.

Here is an overview of the parameters which describe the detector performance:

4.1.1 Responsivity R_{esp}

In order to evaluate a detector performance, the detector's responsivity must be calculated. The Responsivity of the photodetector is expressed as:

$$R_{esp} = (1 - e^{-\alpha l})\gamma_c \frac{\eta_i}{h\nu} \tag{4.1}$$

where η_i is the internal quantum efficiency for a thin metal film defined in equation 4.19, γ_c is the coupling efficiency of the optical source into the SPP mode, l is the length of the waveguide, and α is the mode power attenuation coefficient of the SPP mode [34].$h\nu$ is in eV.

4.1.2 Minimum Detectable Power S_{min}

The minimum detectable power of the photodetector is defined as the ratio of the dark current to the responsivity.

$$S_{min} = \frac{I_{dark}}{R_{esp}} \tag{4.2}$$

where R_{esp} is the responsivity, and I_{dark} is the dark current of the photodiode.

The minimum detectable power (S_{min}) is directly proportionate to the dark current and thus, it is proportional to the temperature as well. So, if the device is cooled down,

the minimum detectable power will be reduced.

4.1.3 Dark Current I_{dark}

According to the thermionic theory, the dark current is given by:

$$I_{dark} = C_{area} A^{**} T^2 \exp(\frac{-q\phi_B}{KT}) \tag{4.3}$$

where C_{area} is the Schottky contact area, T is the absolute temperature which is taken to be $300K$, and A^{**} is the effective Richardson constant (112 and 32 $Acm^{-2}K^{-2}$ for electrons and holes, respectively) [18].

4.1.4 The Optical Absorptance Factor A

It is the ratio of the absorbed optical power to the incident optical power.

$$A = \frac{S_{abs}}{S_{inc}} \tag{4.4}$$

Many photodetector suffer from low optical absorptance.

4.1.5 Internal and External Quantum Efficiencies η_i, η_e

The internal quantum efficiency η_i, known also as the internal photoyield, is defined as the number of carriers that contribute to the photocurrent I_p per absorbed photon per second [13, 19]. It is given by:

$$\eta_i = \frac{I_p/q}{S_{abs}/h\nu} \tag{4.5}$$

where I_p is the photocurrent, q is the elemental charge, S_{abs} is the absorbed optical

power, h is Plank's constant, and ν is the optical frequency.

The internal quantum efficiency is related to the external quantum efficiency through the following equation:

$$\eta_e = A\eta_i \tag{4.6}$$

where A is the optical absorptance factor.

The external quantum efficiency η_e, known also as the external photoyield, can be defined as the number of carriers which contribute to the photocurrent per incident photon per second.

The external quantum efficiency using equations 4.4, 4.5, 4.6 can be given by:

$$\eta_e = \frac{I_p/q}{S_{inc}/h\nu} \tag{4.7}$$

where I_p is the photocurrent, q is the elemental charge, S_{inc} is the incident optical power, h is Plank's constant, and ν is the optical frequency.

The responsivity of the photodetector can be expressed in terms of η_i and η_e as follows [19]:

$$R_{esp} = \frac{I_p}{S_{inc}} = \frac{\eta_e q}{h\nu} = \frac{A\eta_i q}{h\nu} \tag{4.8}$$

Using a temperature of $T = 40K$ and a free-space optical wavelength of $\lambda_0 = 1500nm$, the external quantum efficiency η_e was measured by Chen et al [70, 19] for a $2nm$ thick $PtSi/p-Si$ Schottyk detector to be 5% and 2% for back and front illumination, respectively. Furthermore, using an optical cavity on the front side of the structure was reported to enhance the performance of the detector. For example, Kosonocky et al. [59, 19] formed an optical cavity on the front side of the structure using layers of Al

and *Sio* which resulted in responsivities (R_{esp}) up to $0.25A/W$ and an external quantum efficiency ($\eta_e \sim 20$) under back illumination.

4.1.6 The Emission Probability

Since the Schottky diode is integrated into a thin metal film for this thesis work, the total emission probability is calculated by modelling a carrier travelling back and forth across the metal thickness. This carrier has a finite emission probability each time it reaches the metal semiconductor interface, which is known as Schottky barrier [19, 5].

If a carrier travels m times across the metal thickness, the probability of internal photoemission of this carrier can be defined as:

$$P_m(E) = \frac{1}{2}(1 - \sqrt{\frac{\phi_B}{h\nu \ e^{(\frac{-2mt}{L})}}}\ ) \tag{4.9}$$

where L is the attenuation length of a hot carrier in the metal, which is equal to 74 and 55 for electrons and holes in Au, respectively [19, 5].

Photoemission at the metal-air interface is impossible in our case because the work function of the metal is much larger than the energy of infrared photons [19]. In this case, the emission probability of hot carriers over this interface is zero [5]. The total emission probability of a hot carrier over the Schottky barrier can then be calculated as the sum of all emission probabilities including an emission probability of a carrier that was reflected off the barrier m times.

The total photoemission probability is defined as the sum of probabilities of carriers that have reflected off the metal semiconductor contact 0 to m times [19],[5].

$$P(E) = \Sigma_{m=0}^{\infty} P_m(E) \Pi_{k=0}^{m-1} [1 - P_k(E)] \tag{4.10}$$

4.2 Thick and Thin Film Schottky Barrier Detectors

Scales and Pierre Berini [19] presented models for the quantum efficiency of thick and thin film Schottky barrier detectors; two thin film models and one thick film model were produced. One thin film model has one single Schottky barrier where a metal film is placed onto a Si substrate. The other thin film model has two Schottky barriers where a metal film is buried in Si. The latter model enhanced the quantum efficiency as both barriers contributed to the photoemission process. Those models were applied by Berini group to test the impact of using metal stripes in plasmonic photodetectors on the performance of such detectors. Detection was maintained via the three-step internal photoemission process which includes photoexcitation of carriers, transport of excited carriers, and emission of excited carriers into the semiconductor [19].

Photoexcitation is when an electron in the metal located in a state below E_F (at a temperature of 0K) absorbs an incident photon and is elevated to a higher state, leaving a free hole behind [19, 5]. Transport is when an excited carrier (electron or hole) acquires enough energy and overcomes the Schottky barrier height ϕ_B. This gained energy is also known as the excess energy of the transported carrier. In this step, the velocity of the excited carrier in the direction perpendicular to the interface contributes to a kinetic energy that exceeds the Schottky barrier height ϕ_B; thus, enabling the excited carrier to cross over the Schottky barrier [5]. Finally, emission is when the hot carrier is emitted into the semiconductor where it will be collected as photocurrent [19]. Figure 4.1 depicts the three-step internal photoemission process for (a) $n-Si$ and (b) $p-Si$.

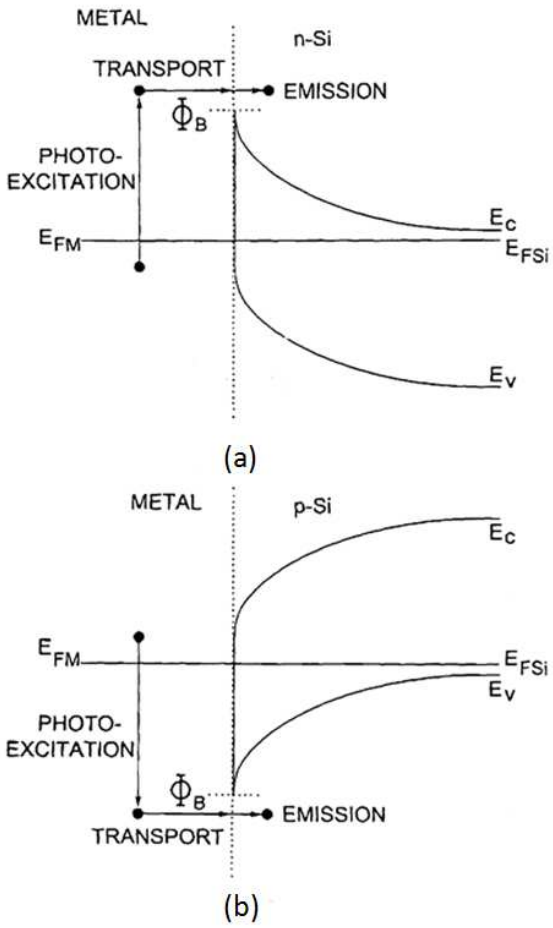

Figure 4.1: The energy band diagrams of Schottky barriers involved in the 3-step internal Photoemission process. (a, b) represent the emission of a hot electron and a hot hole over the Schottky barrier on $n-Si$ and $p-Si$, respectively. Figure is shown as published in [71].

4.2.1 Thick Film Single Barrier Schottky Detectors

A metal film is considered thick if $t \gg \delta$, L_e, L_h where δ is the skin depth , L_e is the hot electrons attenuation length, L_h is the hot holes attenuation length.

The skin depth δ is the distance at which an optical field incident perpendicularly drops to $\frac{1}{e}$ of its incident magnitude when propagating through a lossy medium [19]:

$$\delta = \frac{1}{\sqrt{\pi \nu \mu \sigma}} \tag{4.11}$$

Where ν is the optical frequency, μ is the permeability, and σ is the conductivity of the

material. The skin depth was computed for various metals at $\lambda_0 = 1550$ and $1310nm$. Below are some of the computed values for the skin depth:

Table 4.1: Skin depths and attenuation lengths of hot carriers for A_g, C_u, and A_u at $\lambda_0 = 1550$ and $1310nm$. Table is adapted from [19].

Metal	$\delta(nm)$ at $\lambda_0 = 1550nm$	$\delta(nm)$ at $\lambda_0 = 1310nm$	$L_e(nm)$	$L_h(nm)$
Ag	4.6	4.2	44	
Cu	4.8	4.4	14.5	
Au	5.6	5.2	74	55

It is noted from table 4.1 that $L \gg \delta$. This is true for several metals and when using photons whose wavelengths are between 1000 and $2000nm$ [19].

If T was assumed to be $0K$ and if the total energy $E_s > E_F + \phi_B$ or the excess energy $E_d > \phi_B$, then a hot carrier will have a chance of being emitted over the Schottky barrier [19].

If the electron was treated as a classical particle with kinetic energy equal to the photon energy, and if we assume that the electron cannot cross the barrier unless it has enough momentum in the direction perpendicular to the metal surface, we can write the following relation for the internal quantum efficiency η_i for a thick metal film [5], [19].

$$\eta_i = \frac{1}{2}(1 - \sqrt{\phi_B/h\nu}) \tag{4.12}$$

4.2.2 Thin Film Single Barrier Schottky Detectors

A metal film is considered thin if the following condition is satisfied:

$$t \ll L_e, L_h \tag{4.13}$$

If we assume a Schottky contact structure is illuminated through back-side illumination

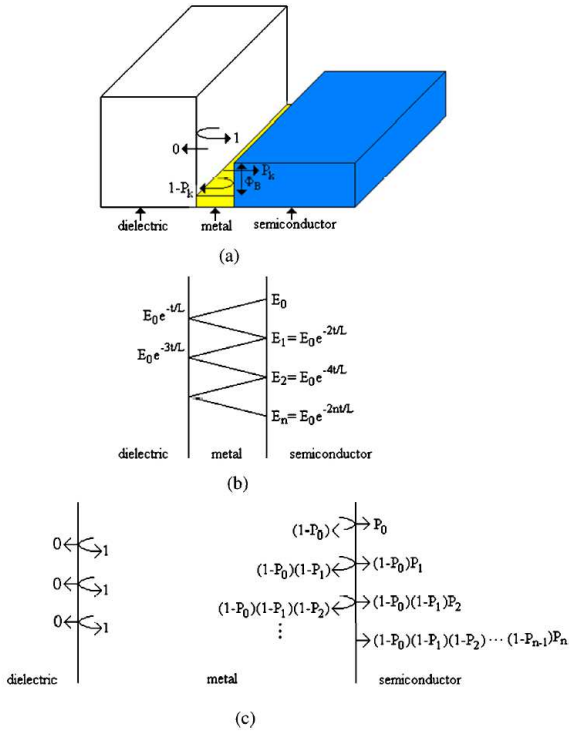

Figure 4.2: (*a*) Hot carrier reflections in a thin-film single-barrier Schottky detector. (*b*) Excess energy of a (non-emitted) hot carrier at each interface after reflection (multiple hot carrier reflections). (*c*) Emission probability of a hot carrier as the number of reflections increases. Figure is shown as published in [19].

by photons of energy $h\nu$ and, if we assume that those photons are absorbed uniformly in the metal film, then the excited hot carriers can experience reflections off the internal metal walls which results in increasing their emission probability over the Schottky barrier [19].

Figure 4.2.2 illustrates the reflection of hot carriers off the internal metal surfaces in a single barrier Schottky detector and the increased emission probability of the hot carriers as the number of reflections increase. The emission probability is defined as P_k and the reflection probability is defined as $(1 - P_k)$, with all reflections assumed to be diffuse. The emission probability over the metal-dielectric interface is zero, thus the reflection probability of the internal side of the interface is 1.

Assuming $T = 0K$ and a uniform distribution of hot carrier's positions and excess energy E_d between 0 and $h\nu$, and for an isotropic distribution of momenta, a reduction in the hot carrier population as well as in its excess energy is expected after one round

trip due to emission and scattering, respectively. Thus, a new round trip will cause more reduction in both hot carrier's population and excess energy.

As noted in figure 4.4 (b), a carrier having an excess energy E_d that is equal to E_0,where $E_0 > \phi_B$, travels a distance of $2t$ after being reflected from the metal-semiconductor interface and its excess energy after reduction becomes $E_1 = E_0 e^{\frac{-2t}{L}}$. This carrier's excess energy is reduced to $E_2 = E_0 e^{\frac{-4t}{L}}$ after being reflected twice (two round trips) and to $E_n = E_0 e^{\frac{-2nt}{L}}$ after being reflected off the metal-semiconductor interface n times (n is the total number of round trips possible before the carrier's excess energy becomes equal to ϕ_B). The maximum number of round trips occurs when E_0 is equal to $h\nu$. n can be defined in terms of E_0 and ϕ_B as follows:

$$n = \frac{L}{2t} ln(\frac{E_0}{\phi_B}) \tag{4.14}$$

thus,

n_{max} can be defined as follows:

$$n_{max} = \frac{L}{2t} ln(\frac{h\nu}{\phi_B}) \tag{4.15}$$

As described in figure (c), the total emission probability of a hot carrier, whose excess energy E_0 is greater than the Schottky barrier energy ϕ_B is given by the following equation:

$$P^t(E_0) = P_0 + (1 - P_0)P_1 + (1 - P_0)(1 - P_1)P_2 + ... + P_n \Pi_{k_0}^{n-1}(1 - P_k) \tag{4.16}$$

where: P_k is the emission probability of a carrier that has an excess energy E_k, thus $P_k = P(E_k)$ and is defined through the following equation:

$$P(E_k) = \frac{1}{2}(1 - \sqrt{\frac{\phi_B}{E_k}}) \tag{4.17}$$

where $E_k > \phi_B$.

and,

$$E_k = E_0 e^{-2k\frac{t}{L}} \tag{4.18}$$

Previous assessments were done to evaluate the emission probability of hot carriers after multiple reflections off the internal metal-semiconductor interfaces and while their excess energy E_0 is being reduced to the value of the Schottky barrier energy ϕ_B . Scales [19] computed the probability of emission for both thin and thick film single-barrier Schottky detectors as a function of $(\frac{L}{t})$ where E_d=E_0= $h\nu$ =0.8eV and ϕ_B = 0.208eV. The result is shown on figure 4.3, where $P^t(E_0)$ and $P(E_d)$ denote the emission probabilities for thin and thick film single-barrier Schottky detectors, respectively. As seen in this result, when the metal gets thicker (t value increases) and $(\frac{L}{t})$ drops to zero, the probability of emission for the thin film single-barrier Schottky detector approaches the value of emission probability for the thick film. Thus, no multiple reflections will occur as the attenuation length is very small. On the other hand, for the thin film case, the number of hot carrier reflections increases and the probability of emission $P^t(E_0)$ approaches 1 as the fraction $(\frac{L}{t})$ approaches infinity for any value of E_0 that is higher than ϕ_B but smaller than $h\nu$, this can also be observed through equations 4.14, 4.16, 4.17, 4.18. The reduction of excess energy due to reflections is negligible in the thin film case and does not prevent emission. The thin film single barrier Schottky detector enhanced the internal quantum efficiency with an internal quantum efficiency gain of $\sim$ 2.4 for $(\frac{L}{t}) \sim 10$ compared to the thick film Schottky barrier detector. The thin film double barrier Schottky detector provided a gain of $\sim$ 4.6. The gain doubled for the double barrier case due to emission over 2 barriers.

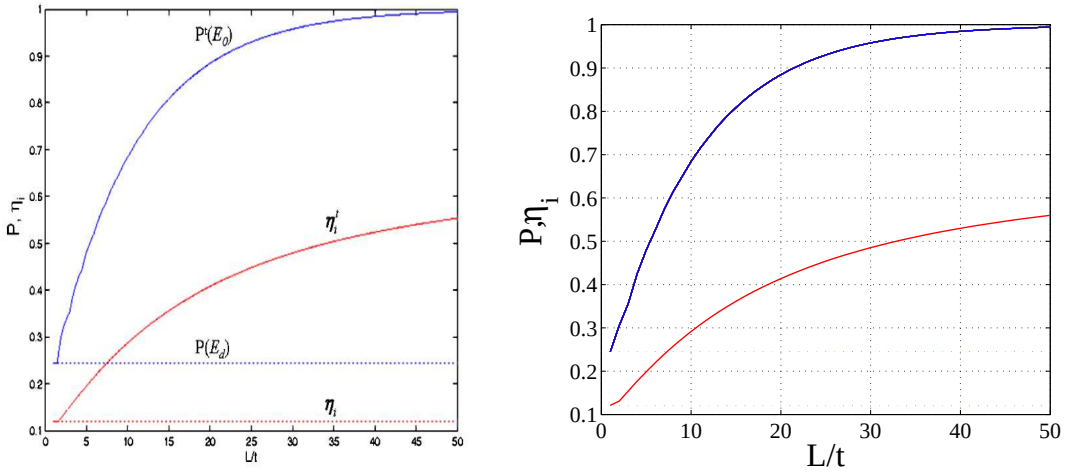

(a) (b)

Figure 4.3: Validation of emission probability and internal quantum efficiency of thick-film (dashed) and thin-film (solid) single-barrier Schottky detectors . 4.3a is the original data and 4.3b is a validation.

Thin film Schottky contact photodetectors provide enhanced internal quantum efficiencies because of the multiple hot carrier reflections within the metal film. Using very thin metal films ($t << L$) can enhance the internal photoemission process because of the increased number of hot carrier reflections, thus increasing the number of opportunities for the carriers to be emitted over the Schottky barrier [19],[5]. Thin metal films are quite useful for optical communications devices.

For a thin metal film, the internal quantum efficiency can be defined as:

$$\eta_i^t = \frac{1}{h\nu} \int_{\phi_B}^{h\nu} P^t(E_0)\, dE_0 \tag{4.19}$$

Where ϕ_B is the Schottky barrier height (0.80 and 0.34 eV for Au on $n - Si$ and $p - Si$, respectively), ν is the optical frequency, and h is Plank's constant. $P^t(E)$ is the total probability of internal photoemission of a hot carrier.

As noted on figure 4.3, the internal quantum efficiency for thin and thick film single-barrier Schottky detectors is plotted as a function of $(\frac{L}{t})$. The graphs, which were initially produced by Crestine, show an increasing number of hot carrier reflections as $(\frac{L}{t} \to \infty)$.

This was demonstrated through through the increase of η_i^t as $(\frac{L}{t}) \to \infty$. In contrast,η_i^t does not reach unity as $(\frac{L}{t})$ approaches infinity which is attributed to the fact that not all excited electrons acquire an excess energy (E_0) that is higher than ϕ_B.

If we assume that all carrier of excess energy E_0 that is higher than ϕ_B are emitted, then the internal quantum efficiency can be rewritten using equation 4.19 as follows:

$$\eta_{t,\infty}^t \cong \frac{h\nu - \phi_B}{h\nu} \tag{4.20}$$

Where $P^t E_0 \to 1$ when $(\frac{L}{t}) \to \infty$.

If a carrier has an initial probability of having a velocity in all directions and if near the Fermi level in the metal, there is a regular density of states, the probability of carrier escape over the Schottky barrier can then be evaluated as the ratio of those velocities, knowing that their normal component is larger than the Schottky barrier [5]. In the diagram shown in figure 4.4, the probability of emission can be defined as the ratio of the surface area of the cone to the surface area of the sphere [5].

$$P(E) = \frac{1}{2}(1 - \sqrt{\frac{\phi_B}{E}}) \tag{4.21}$$

4.3 The responsivity of an asymmetric nano-structured Silicon based photodetector

The Schottky photodetector significant in this thesis is integrated into an asymmetric SPP waveguide and operating in the short-range SPP. It has lower responsivity than a Schottky photodetector integrated into a symmetric SPP waveguide, which operates in the long range SPP; however, its length can be significantly shorter due to the high attenuation of its supported SPP modes which results in less required wafer area. It is easier to fabricate; thus it is considered to be of lower cost than the symmetric. The aforementioned advantages make the asymmetric photodetector appealing for low cost silicon based photonics.

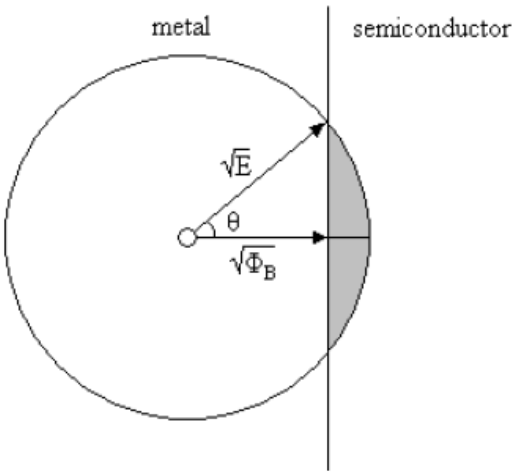

Figure 4.4: Uniform distribution of electron momentum in entire momentum space.Figure is shown as published in [5].

The responsivity of a detector is greatly affected by the reverse bias applied. For example, a responsivity of $1mA/W$ was reported for Au stripe of width $2.5\mu m$ and thickness $135nm$ deposited on $n-Si$ for a reverse bias of $200\Omega mV$ and an optical power of $2mW$ [34]. Moreover, a structure using a $1.5\mu m$ wide and $40nm$ thick Au stripe under reverse bias of $100mV$, incident optical power of $1mW$, and an excitation wavelength of $1310nm$ provided a good responsivity. On the other hand, other structures which operate near breakdown; under a strong reverse bias reported $10X$ increase in responsivity compared to structures with low reverse bias [35, 37].

There is a number of factors that can generate a good responsivity. They can be generally summarized in the following steps [19, 4]:

1. Efficient coupling to $SPPs$ guided by the stripe.

2. Full absorption of $SPPs$ along the length of the stripe, which results in hot carriers creation in the metal along the interfaces.

3. The multiple internal reflections which result in an increased probability for carrier escape from the metal stripe into the semiconductor through the internal photoe-

mission process (IPE).

4. Having more than one barrier which means more carriers will be escaping.

4.4 Modelling Results

With the use of end-fire excitation from a tapered optical fiber, the photodetector's coupling efficiency, responsivity, photocurrent, dark current, and minimum detectable power were calculated, allowing for evaluation of the devices performance.

The detector's responsivity (R) is directly proportional to the coupling efficiency γ_c; as such, the higher the coupling efficiency, the greater the device's responsivity is. Referring to figures 4.5,4.6, it can be noted that the greater responsivity is achieved for stripes with larger thickness and vice versa. This trend is also the same with the stripe's width. The higher responsivity achieved for the range of waveguide structures investigated in this research is for a structure of $50nm$ thickness and $100nm$ width. That is associated with the greatest coupling efficiency acquired in this research at this specific thickness and width. It can also be noted that the reponsivity is greater when using $p-Si$ due to the low Schottky barrier height which allows for more carrier escape from the metal to the semiconductor.

In addition to the type of Si substrate, the operating wavelength also has a great impact on the device's performance. Results shown on figures 4.5,4.6,4.7, and 4.8 indicate that the responsivity is better at the wavelength $1550nm$ than the wavelength $1310nm$.

Generally, the responsivity increases with increasing stripe thickness t and width w. It is higher for modes of lower real effective index and this explains why it is higher at the wavelength $1550nm$ than $1310nm$.

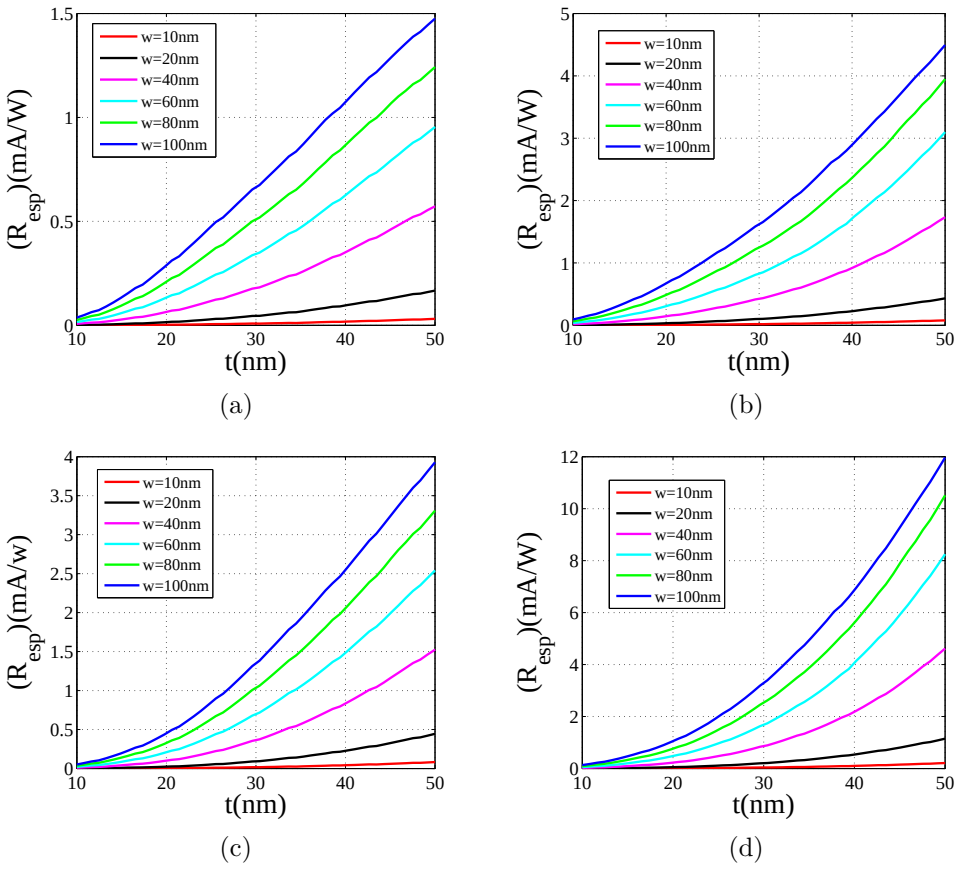

Figure 4.5: Responsivity as a function of metal thickness, generated by using data from the coupling between a fiber having $\sim 2.25\mu m$ spot size at $\lambda_0 = 1310nm$ and $\sim 2.5\mu m$ spot size at $lambda_0 = 1550nm$ and a photodetector whose stripe thickness ranges from $10nm$ to $50nm$ at (a, c) $\lambda_0 = 1310nm$ and (b, d) $\lambda_0 = 1550nm$ for (a, b) carriers are electrons $L_e = 74nm$, $\Phi_B = 0.8ev$ and (c, d) carriers are holes $L_h = 55nm$, $\Phi_B = 0.34ev$.

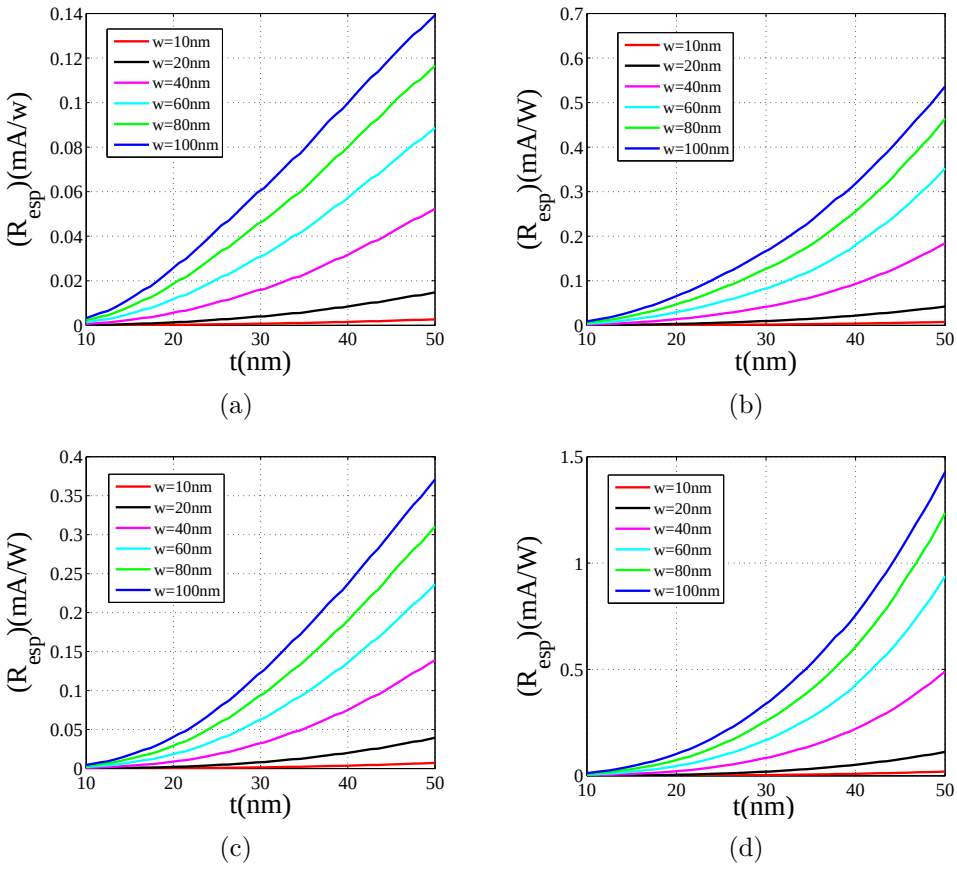

Figure 4.6: Responsivity as a function of metal thickness, generated by using data from the coupling between a fiber having $\sim 9.129\mu m$ spot size at $\lambda_0 = 1310nm$ and $\sim 10.183\mu m$ spot size at $lambda_0 = 1550nm$ and a photodetector whose stripe thickness ranges from $10nm$ to $50nm$ at (a, c) $\lambda_0 = 1310nm$ and (b, d) $\lambda_0 = 1550nm$ for (a, b) carriers are electrons $L_e = 74nm$, $\Phi_B = 0.8ev$ and (c, d) carriers are holes $L_h = 55nm$, $\Phi_B = 0.34ev$.

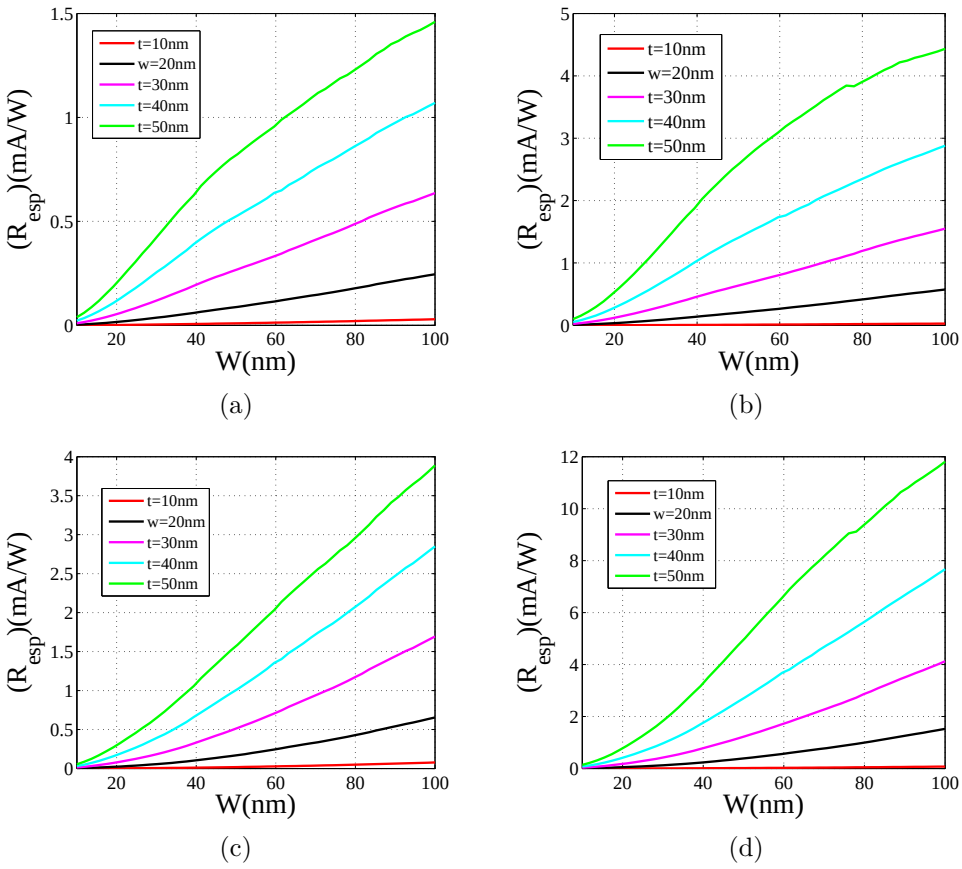

Figure 4.7: Responsivity as a function of metal width, generated by using data from the coupling between a fiber having $\sim 2.25\mu m$ spot size at $\lambda_0 = 1310nm$ and $\sim 2.5\mu m$ spot size at $lambda_0 = 1550nm$ and a photodetector whose stripe thickness ranges from $10nm$ to $50nm$ at (a, c) $\lambda_0 = 1310nm$ and (b, d) $\lambda_0 = 1550nm$ for (a, b) carriers are electrons $L_e = 74nm$, $\Phi_B = 0.8ev$ and (c, d) carriers are holes $L_h = 55nm$, $\Phi_B = 0.34ev$.

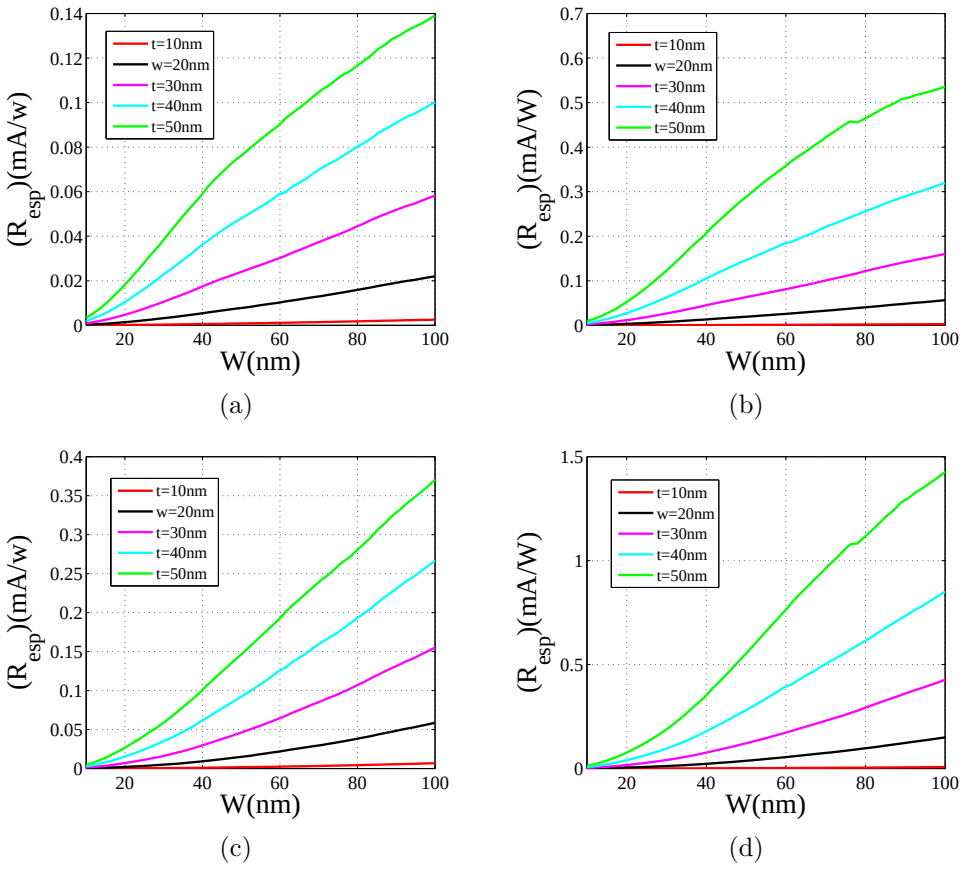

Figure 4.8: Responsivity as a function of metal width, generated by using data from the coupling between a fiber having $\sim 9.129\mu m$ spot size at $\lambda_0 = 1310nm$ and $\sim 10.183\mu m$ spot size at $lambda_0 = 1550nm$ and a photodetector whose stripe thickness ranges from $10nm$ to $50nm$ at (a, c) $\lambda_0 = 1310nm$ and (b, d) $\lambda_0 = 1550nm$ for (a, b) carriers are electrons $L_e = 74nm$, $\Phi_B = 0.8ev$ and (c, d) carriers are holes $L_h = 55nm$, $\Phi_B = 0.34ev$.

The propagation length of the detectors was selected such that the term $e^{-\alpha l}$ is negligible ($e^{-\alpha l} \ll 0.001$) using the attenuation of the modes which were calculated and presented in Chapter 2 as a function of waveguide thickness and width at the two adopted wavelengths.

Here is a calculation example:

$$e^{-\alpha l} \ll 0.001 \tag{4.22}$$

then,

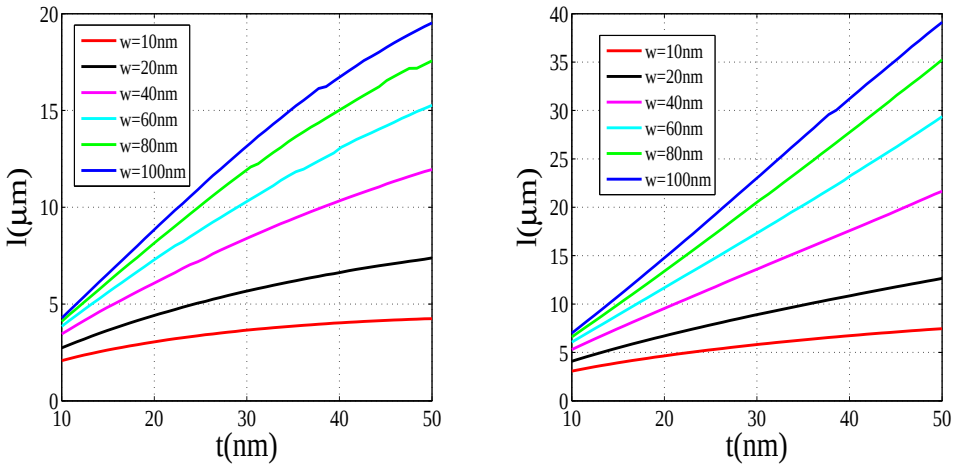

Figure 4.9: Stripe length as a function of metal thickness at several stripe widths. (a) at $\lambda_0 = 1310nm$ and (b) at $\lambda_0 = 1550nm$.

$$l \cong \frac{ln(0.001)}{\alpha} \tag{4.23}$$

where:

$$\alpha = Im(n_{eff}) * 2\pi/\lambda_0 \tag{4.24}$$

Making the photodetector smaller in size can reduce the cost of the device especially since each wafer is composed of a large number of devices [18].

Figures 4.9, 4.10, show the device length as a function of stripe thickness and width.

The maximum detector lengths for the range of stripe dimensions investigated in this research are $20\mu m$ and $40\mu m$ for structures operating at $1310nm$ and $1550nm$, respectively.

The minimum detectable power S_{min} demonstrated an increase with decreasing structure thickness and width. The results are shown on figures 4.11, 4.12. The highest minimum detectable power is achieved for a device having $t = w = 10nm$.

Minimum detectable power is converted to dBm using the following:

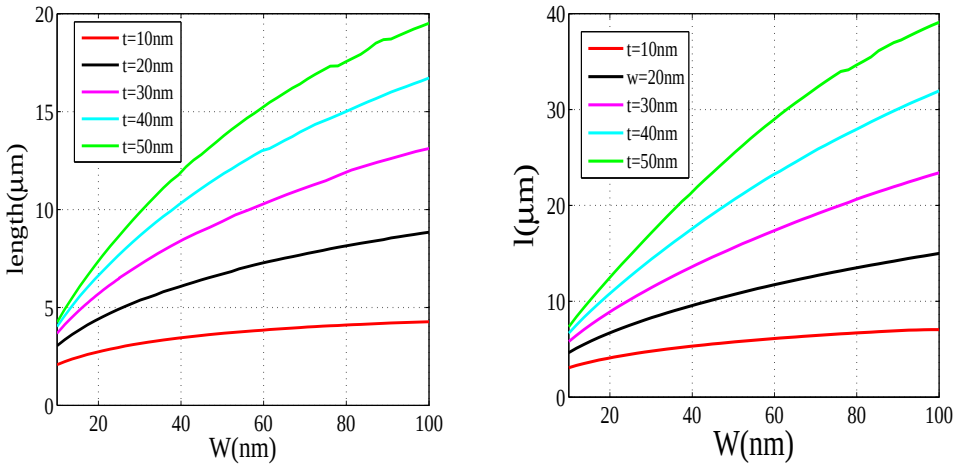

Figure 4.10: Stripe length as a function of metal width at several stripe thicknesses. (a) at $\lambda_0 = 1310nm$ and (b) at $\lambda_0 = 1550nm$.

$$Smin_{dBm} = 10 * (log(1000 * Smin)) \tag{4.25}$$

The power shows a non-smooth relation with metal thickness, which reflects the number of emission probabilities or reflections the carrier encounters before it is successfully emitted into the semiconductor. This can be understood through equations 4.15, 4.16.

The dark current results achieved in this thesis are very promising as they showed a rapid decrease in dark current as the stripe width shrinks from $100nm$ to $10nm$. With a stripe thickness of $10nm$, the device produces a very low dark current that gets almost negligible for a stripe sized $10nm$ thick and wide. As expected, when using p-type Schottky barrier, high quantum efficiency and photocurrent are achieved but this comes at the expense of large dark current. The dark current versus the Schottky contact area is shown on figure 4.13 for $n - si$ and $p - si$ at $1310nm$ and $1550nm$.

The photocurrent maps achieved for the nanostructures Schottky diode that is integrated into a thin metal stripe are computed and presented. The largest photocurrent is acquired using a Schottky photodetector that is integrated into a metal stripe of $50nm$ thickness and $100nm$ width, deposited on p-type Si substrate and operates at the wavelength $1550nm$. The photocurrent maps, generated for the two structures studied in this thesis work, are shown on the figures 4.14, 4.15.

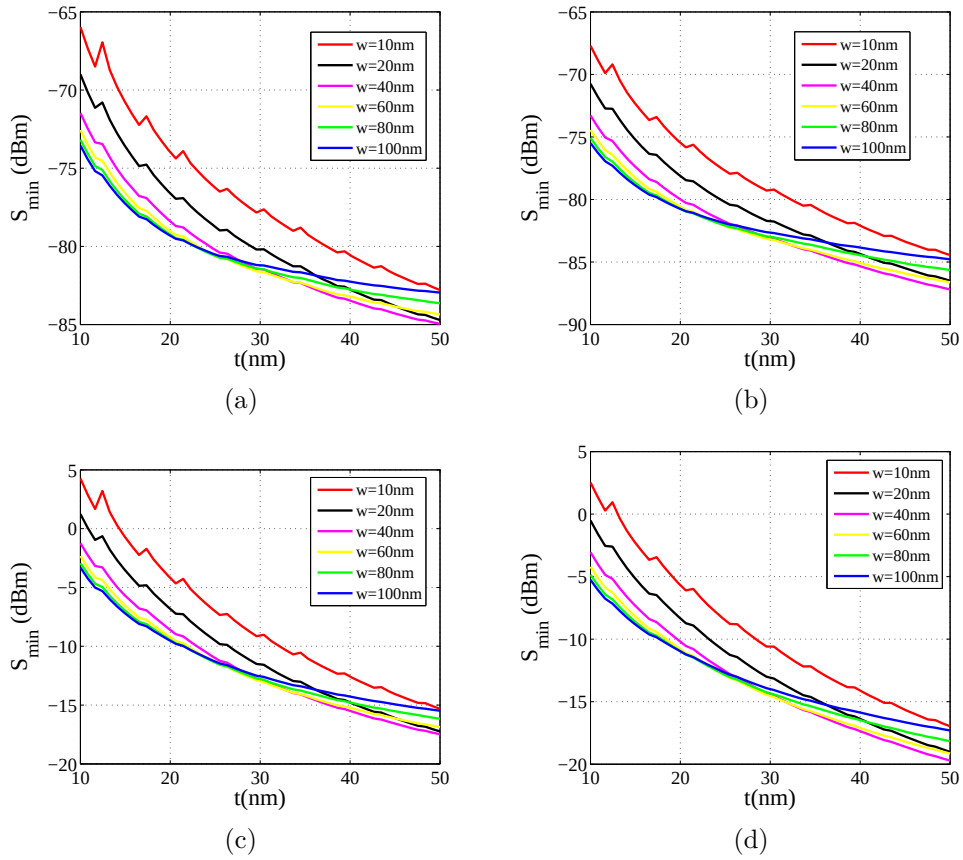

Figure 4.11: Minimum detectable power ($Smin$) as a function of stripe thickness (waveguide thickness) at (a, c) $\lambda_0 = 1310nm$ and (b, d) ($\lambda_0 = 1550nm$) for(a,b) carriers are electrons and (c, d) carriers are holes.

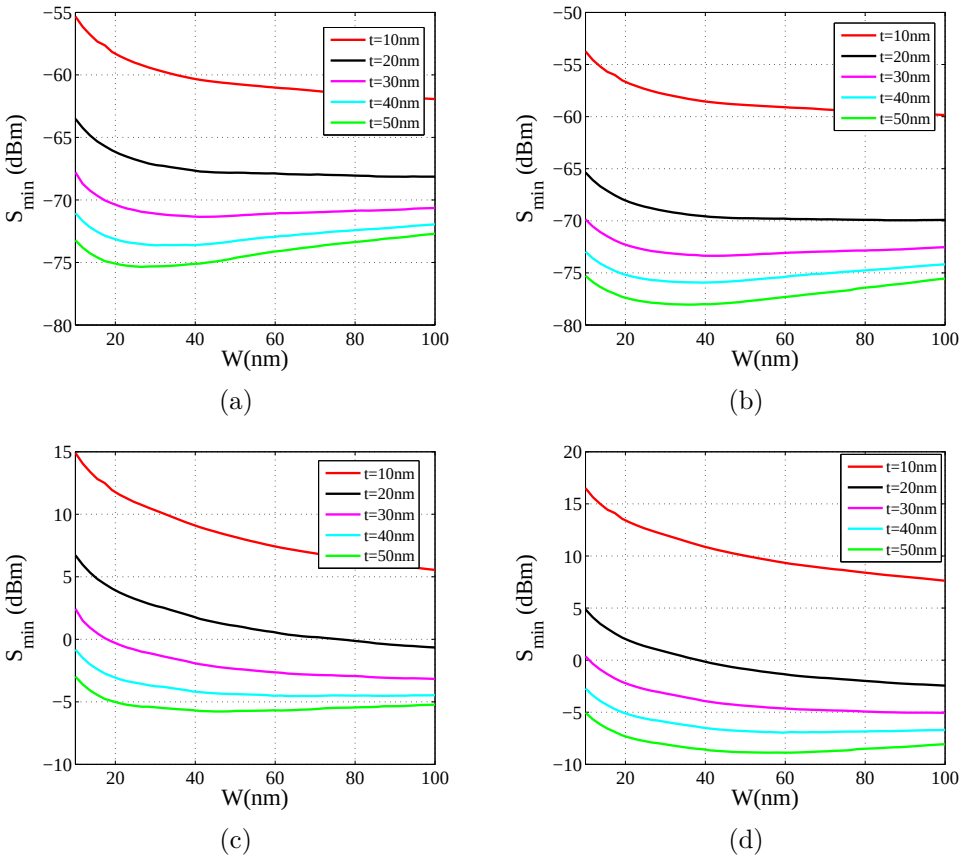

Figure 4.12: The minimum detectable power ($Smin$) as a function of the stripe's width (w) (the waveguide's width) at (a, c) $\lambda_0 = 1310nm$ and (b, d) ($\lambda_0 = 1550nm$) for (a, b) carriers are electrons and (c, d) carriers are holes.

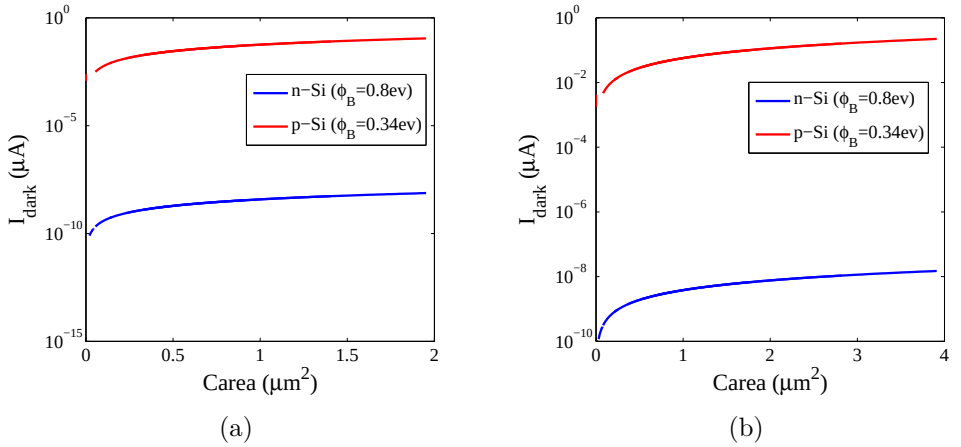

Figure 4.13: The dark current ($Idark$) as a function of the waveguide's area ($Carea$) at (a) $\lambda_0 = 1310nm$ and (b) $\lambda_0 = 1550nm$.

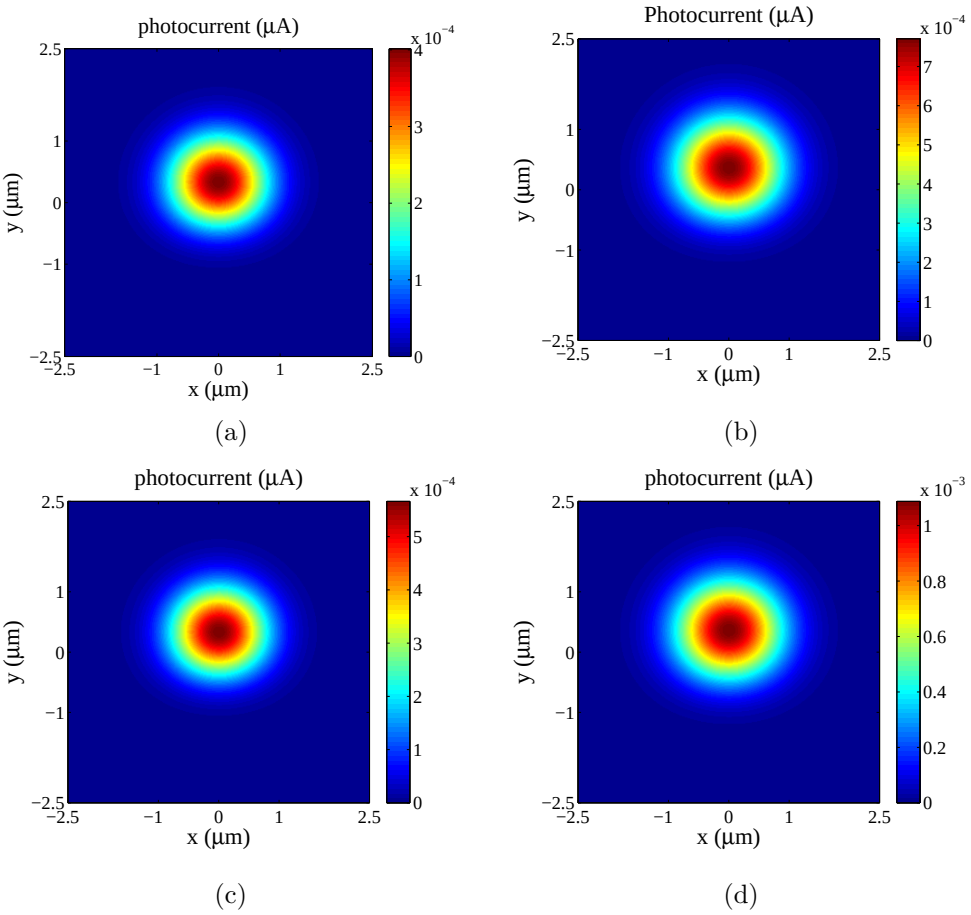

Figure 4.14: The photocurrent map generated for a Schottky photodetector integrated into an Au stripe of $10nm$ thickness and $10nm$ width for (a, c) $n - Si$ and $p - Si$, respectively at the wavelength $1310nm$, and for (b, d) $n - Si$ and $p - Si$, respectively at the wavelength $1550nm$.

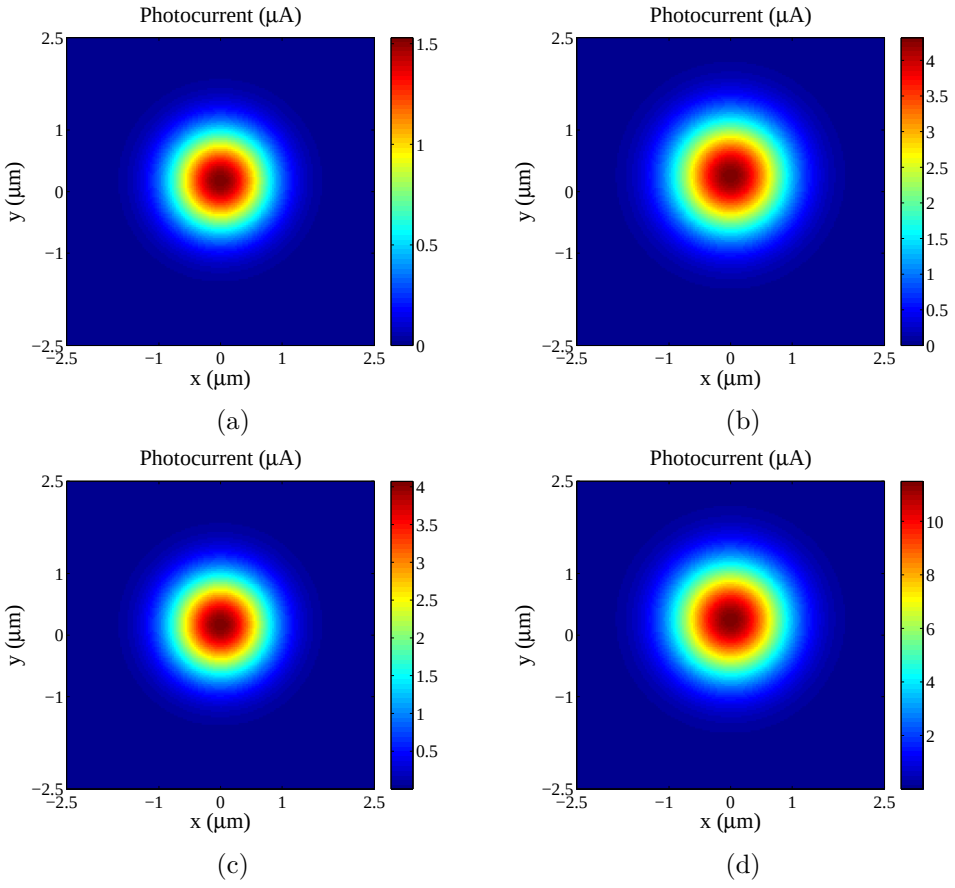

Figure 4.15: The photocurrent map generated for a Schottky photodetector integrated into an Au stripe of $50nm$ thickness and $100nm$ width for (a, c) $n - Si$ and $p - Si$, respectively at the wavelength $1310nm$, and for (b, d) $n - Si$ and $p - Si$, respectively at the wavelength $1550nm$.

Chapter 5

Conclusion, Contributions and Future work

5.1 Conclusion

A nanostructured schottky photodetector is of a growing interest in integrated optics technology, mainly because of the attractive properties of Si, the ease of fabrication of this device, and its performance as a detector as well as a waveguide structure . Investigating the performance of this detector at the nano-scale was an attempt to explore if some other advantages can exist such as, a near field scanner.

The device combines a Shottky detector structure with a waveguide structure and operates with the internal photoemission mechanism (IPE). This device is able to detect surface plasmons or involve them in the photodetection process. Properties of $SPPs$ allow for producing small detectors with dimensions similar to the ones of highly integrated electronic elements. The use of small detectors can be very useful for biochemical sensing, low-noise high-speed detection, photovoltaic solar energy conversion, near- and mid-infrared imaging, single plasmon detection.

A Schottky based nano-photodetector that operates with IPE and is able to produce enhanced photo-response, large photocurrent to dark current ratio, and decreased minimum detectable power is studied and presented. This type of detector can be very useful for near field scanning applications. This plasmonic photodetector allow for Local enhancement of electric fields. It can also enhance the absorptance. With the nano-scale

metal features, this detector can have another advantage which is the increasing number of total internal reflections which, in turn, increases the emission probability of excited carriers.

The fundamental mode of this Schottky detector was coupled to an optical fiber mode at optical wavelengths and good coupling efficiency values were achieved.

Detection of a tiny Schottky photodetector by another identical tiny Schottky photodetector was investigated and approved. A maximum coupling of 1 was achieved. The detector performance is highly affected and well defined by the geometry of the waveguide, the materials used, and the wavelength.

5.2 Contributions

The work presented in this thesis has made contributions to the field of Schottky based photodetectors. The behaviour of a nano-structured Schottky based photodetector having a single Schottky barrier and operates with IPE was studied in detail.

Effects of several parameters on the performance of the device was determined.

The detection has been evaluated based on the coupling calculations of the fundamental supported mode of a Schottky nano-detector with the mode of a tapered optical fiber at different optical wavelengths.

The performance of the nano-structured Schottky detector as a near-field scanner was investigated and presented.

A manuscript based on this thesis work is in preparation for publication.

5.3 Future Work

The results presented in this theoretical thesis work are promising. The work highlights the performance of a Schottky nano-detector as a near field scanner. Some experimental

verification is required to confirm the results obtained.

Appendix A

Surface Plasmon Polaritons at a Single Interface

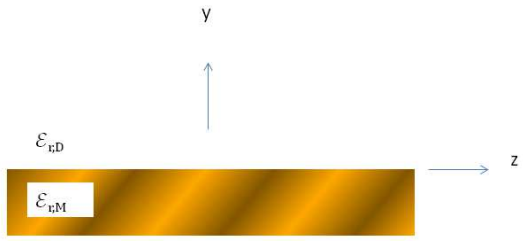

Figure A.1: An interface between a semi-infinite dielectric of relative permittivity $\varepsilon_{r,D}$ and a semi-infinite metal of relative permittivity $\varepsilon_{r,M}$.

A metal at optical frequencies gets very similar to a cold plasma with a negative real part and a non-negligible imaginary part for its permittivity where both the real and imaginary parts of the permittivity are larger than zero. From the fact that an interface between two materials with opposite signs of real part of permittivity can support the propagation of TM surface modes, thus,a metal dielectric interface at optical wavelength can support the propagation of Surface Plasmon Polariton (SPP) modes which are bound to the metal via coupling of electromagnetic waves to electron oscillations at the metal surface [56].The intensity of the SPP modes gets peaked at the interface and experiences an exponential decay perpendicular to the interface [56]. The waveguide is of interest in sensing applications due to the strong localization of field at the interface and to the fact that the propagation of the SPP is largely affected by any small change in the environment [56].

A single interface is the simplest geometry which can support the propagation of SPP_S [46].The field solutions of this single interface SPP mode can be derived from Maxwell's equations.

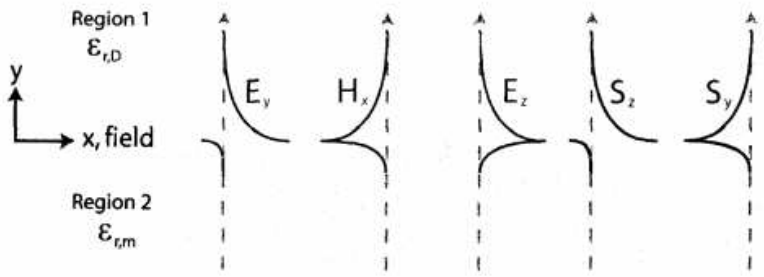

Figure A.2: A diagram showing the field components of the SPP sketched on the dielectric and metal regions (single interface structure). Field are positive on the right of the dotted line, and negative on left. Adapted from [56].

Since $R_e\varepsilon_{r,m} < 0$, the perpendicular electric field component E_y changes sign between the dielectric and metal regions [56]. This is clearly seen in figure A.2.S_z, which is the Poynting vector in the direction of propagation, is negative in the metal because the power in the metal flows in the -z direction, on the contrary, the bulk of the SPP mode travels in the +z direction. S_y ,which is the Poynting vector in the perpendicular direction, is negative in both the dielectric and the metal due to the fact the metal is lossy [56]. As a result, the power continue to propagate downwards until it is finally lost in the metal because of electron scattering.

$$\varepsilon_{r,M} = -\varepsilon_R - j\varepsilon_I \tag{A.1}$$

Where: $\varepsilon_R, \varepsilon_I > 0$
and , $\varepsilon_R >> \varepsilon_{r,D}$

The interface between the metal and the dielectric shown in Figure A.1, supports only a TM polarized mode which is a surface plasmon mode, thus ($H_Z = H_{ZD} = H_{ZM} = 0$). H_{ZD} and H_{ZM} represent the magnetic field components in the direction of propagation for dielectric and metal, respectively.

The interface is invariant along x and z with $+z$ being the propagation direction. Hence, all field dependencies along z are of the form $e^{-\gamma_z} = e^{-\alpha z - j\beta z}$.

Assuming an $e^{+j\omega t}$ time dependence, the field distribution for the non-zero field components of this mode can be derived and an expression for the mode's complex propagation constant can be obtained.

It is also known that for a TM mode, there is no variation in $X - direction$, thus $(\frac{\partial}{\partial x} = 0)$.

In the direction region and by using the solutions for the separation functions, we get the following expression for the electric field in the direction of propagation:

$$E_{ZD} = x(x)y(y)z(z) \tag{A.2}$$

Where :

$$x(x) = A_X e^{-\gamma_x X} \tag{A.3}$$

$$y(y) = A_Y e^{-\gamma_y Y} \tag{A.4}$$

$$Z(z) = A_Z e^{-\gamma_z Z} \tag{A.5}$$

since there is no variation of field in X- direction, equation A.3 becomes:

$$x(x) = A_X \tag{A.6}$$

Substituting equations A.4,A.5, andA.6 in A.2, we get the following form for the electric field in the direction of propagation (+z-direction):

$$E_{ZD} = A_1 e^{-\gamma_{yd} Y} e^{-\gamma_z Z} \tag{A.7}$$

Where:

$$A_1 = A_X A_Y A_Z \tag{A.8}$$

In the metal region and by using the solutions for the separation functions, we get the following expression for the electric field in the direction of propagation:

$$E_{ZM} = x(x)y(y)z(z) \tag{A.9}$$

using equations A.4,A.5, and A.6, equation A.9 cab be represented as:

$$E_{ZM} = A_2 e^{\gamma_{ym} Y} e^{-\gamma_z Z} \tag{A.10}$$

Where γ_{ym} has a positive sign because the transverse field in the metal extends in the opposite direction (-y-direction).

Maxwell's equations in rectangular coordinates are as follows:

$$\frac{\partial}{\partial y}E_z - \frac{\partial}{\partial z}E_y = -j\omega\mu H_x \tag{A.11}$$

$$\frac{\partial}{\partial z}E_x - \frac{\partial}{\partial x}E_z = -j\omega\mu H_y \tag{A.12}$$

$$\frac{\partial}{\partial x}E_y - \frac{\partial}{\partial y}E_x = -j\omega\mu H_z \tag{A.13}$$

$$\frac{\partial}{\partial y}H_z - \frac{\partial}{\partial z}H_y = (j\omega\varepsilon + \sigma)E_x \tag{A.14}$$

$$\frac{\partial}{\partial z}H_x - \frac{\partial}{\partial x}H_z = (j\omega\varepsilon + \sigma)E_y \tag{A.15}$$

$$\frac{\partial}{\partial x}H_y - \frac{\partial}{\partial y}H_x = (j\omega\varepsilon + \sigma)E_z \tag{A.16}$$

Knowing that ($\sigma = 0$) and using equation A.15, we get the following expression for E_y:

$$E_y = \frac{1}{j\omega\varepsilon}(\frac{\partial}{\partial z}H_x - \frac{\partial}{\partial x}H_z) \tag{A.17}$$

Substituting equation A.17 in equation A.11 for E_y, we have:

$$\frac{\partial}{\partial y}E_z - \frac{\partial}{\partial z}[(\frac{1}{j\omega\varepsilon})(\frac{\partial}{\partial z}H_x] = -j\omega\mu H_x \tag{A.18}$$

Taking the differential of equation A.7 with respect to (z), we get:

$$\frac{\partial}{\partial z} = -\gamma_z \tag{A.19}$$

We also can get equation A.19 by taking the differential of equation A.10 with respect to (z).

By substituting equation A.19 in equation A.18, we get:

$$H_x = \frac{j\omega\varepsilon}{(\gamma_z^2 + \omega^2\mu\varepsilon)}\frac{\partial}{\partial y}E_z \tag{A.20}$$

Using the following equation which is known as the constraint equation:

$$\gamma^2 = \gamma_x^2 + \gamma_y^2 + \gamma_z^2 \tag{A.21}$$

And since there is no variation in x-direction, then the term (γ_x^2) is neglected.

Thus,equation A.21 can be rewritten as:

$$\gamma_y^2 = \gamma^2 - \gamma_z^2 \tag{A.22}$$

Equation A.22 can be rewritten again in the following form:

$$\gamma_y^2 = -(\omega^2\mu\varepsilon + \gamma_z^2) \tag{A.23}$$

Where:

$$\gamma^2 = j\omega\mu(j\omega\varepsilon + \sigma) \tag{A.24}$$

And, (σ) which represents the conductivity is equal to zero.

Thus,

$$\gamma^2 = -\omega^2\mu\varepsilon \tag{A.25}$$

Using equation A.23, we can rewrite equation A.20 for H_x to be as follows:

$$H_x = \frac{j\omega\varepsilon}{-\gamma_y^2}\frac{\partial}{\partial y}E_z \tag{A.26}$$

By substituting equation A.26 for H_x in equation A.15 and using equation A.19, we have:

$$E_y = \frac{\gamma_z}{\gamma^2 y}\frac{\partial}{\partial y}E_z \tag{A.27}$$

Where the term $(\frac{\partial}{\partial x}H_z)$ is neglected as there is no variation of field in x-direction.

From equation A.14 and by using equation A.19, we can have the following expression for E_x ,knowing that $H_z = 0$ for TM modes.

$$E_x = \frac{1}{j\omega\varepsilon}(\gamma_z H_y) \tag{A.28}$$

From equation A.28, we can get H_y to be:

$$H_y = \frac{j\omega\varepsilon E_x}{\gamma_z} \tag{A.29}$$

Substituting equation A.29 in equation A.12 for H_y and using equation A.19, we get:

$$(\omega^2\mu\varepsilon + \gamma_z^2)E_x = 0 \tag{A.30}$$

Where the term $(\frac{\partial}{\partial x}E_z)$ is neglected as there is no variation for the field in X-direction.

Since:

$$(\omega^2\mu\varepsilon + \gamma_z^2) \neq 0 \tag{A.31}$$

Thus,

$$E_x = 0 \tag{A.32}$$

Substituting in equation A.12 for $(E_x = 0)$, we get:

$$(H_y = 0) \tag{A.33}$$

In the dielectric region, equation A.26 with substituting the value for E_{ZD} in A.7; can be simplified to:

$$H_{xd} = \frac{j\omega\varepsilon_0\varepsilon_d A_1 e^{-\gamma_z z}}{\gamma_{yd}} e^{-\gamma_{yd} y} \tag{A.34}$$

And, equation A.27 with substituting the value for E_{ZD} in A.7; can be simplified to:

$$E_{yd} = \frac{-\gamma_z A_1 e^{-\gamma_z z}}{\gamma_{yd}} e^{-\gamma_{yd} y} \tag{A.35}$$

Similarly, In the metal region, equation A.26 for H_x and equation A.27 for E_y with the use of equation A.10 for E_{ZM}, can be rewritten in the following forms:

$$H_{xm} = \frac{j\omega\varepsilon_0\varepsilon_m A_2 e^{-\gamma_z z}}{-\gamma_{ym}} e^{\gamma_{ym} y} \tag{A.36}$$

$$E_{ym} = \frac{\gamma_z A_2 e^{-\gamma_z z}}{\gamma_{ym} y} \tag{A.37}$$

By applying the boundary conditions at a dielectric interface, which are as follows:

$$n^{\wedge} \times (\vec{E_2} - \vec{E^{1}}) = 0 \tag{A.38}$$

$$n^{\wedge} \times (\vec{H_2} - \vec{H_1}) = 0 \tag{A.39}$$

$$n^{\wedge} \cdot (\vec{D_2} - \vec{D_1}) = 0 \tag{A.40}$$

$$n^{\wedge} \cdot (B_2^{\rightharpoonup} - B_1^{\rightharpoonup}) = 0 \tag{A.41}$$

we see that the tangential fields components $(E^{\rightharpoonup}, H^{\rightharpoonup})$ are continuous across the interface. Thus, at $(y = 0)$, we can have the following two statements:

$$E_{ZD} = E_{ZM} \tag{A.42}$$

$$H_{xd} = H_{xm} \tag{A.43}$$

by equating equations A.7, A.10, we get:

$$A_1 = A_2 \tag{A.44}$$

Also, by equating equations A.34, A.36, and using the relation A.44, we get:

$$\frac{\varepsilon_{r,d}}{\varepsilon_{r,m}} = \frac{-\gamma_{yd}}{\gamma_{ym}} \tag{A.45}$$

Using the following equation:

$$\gamma^2 = \gamma_x^2 + \gamma_y^2 + \gamma_z^2 \tag{A.46}$$

And knowing that $\gamma_x = 0$ and $\gamma^2 = -\omega^2\mu\varepsilon$, we get:

$$\gamma_y = \sqrt{-\omega^2\mu\varepsilon - \gamma_z^2} \tag{A.47}$$

By substituting equation A.47 in equation A.45 for γ_y, and knowing that $\varepsilon = \varepsilon_0\varepsilon_{r,d}$ in

the dielectric and $\varepsilon = \varepsilon_0 \varepsilon_{r,m}$ in the metal. And, using $\mu = \mu_0$ in both the dielectric and the metal, we get:

$$\gamma_z = i\gamma_0 \sqrt{\frac{\varepsilon_{r,m}\varepsilon_{r,d}}{\varepsilon_{r,m} + \varepsilon_{r,d}}} \tag{A.48}$$

Where: γ_z is the propagation along $z - axis$. And, $\gamma_0 = \frac{\omega}{c}$, $c = \frac{1}{\sqrt{\mu_0 \varepsilon_0}}$

Equation A.48 can be re-written as :

$$\gamma_z = i\beta_0 \sqrt{\frac{\varepsilon_{r,m}\varepsilon_{r,d}}{\varepsilon_{r,m} + \varepsilon_{r,d}}} \tag{A.49}$$

Where: $\beta_0 = \sqrt{\omega^2 \mu_0 \varepsilon_0} = \frac{2\pi}{\lambda_0}$ which is known as the free space wavenumber , ω is the angular frequency given by $\omega = 2\pi f$.

If the metal is described by the lossless Drude Model ($\varepsilon_{r,M} = 1 - \frac{\omega_p^2}{\omega^2}$) with $\omega_p = \sqrt{2} \times 10^{16} s^{-1}$, a plot of ω versus β which is known as the dispersion curve can be obtained by substituting the value of $\varepsilon_{r,M}$ in equation A.48 and knowing that $\varepsilon_{r,D} = 1$ we get:

$$\gamma_z = i\gamma_0 \sqrt{\frac{\omega^2 - \omega_p^2}{2\omega^2 - \omega_p^2}} \tag{A.50}$$

since:

$$\gamma = \alpha + i\beta_z \tag{A.51}$$

and knowing that there is no attenuation in the lossless media, so equation A.51 becomes:

$$\gamma = i\beta_z \tag{A.52}$$

substituting equation A.52 in equation A.50, we get:

$$\beta_z = \frac{2\pi}{\lambda_0}\sqrt{\frac{\omega^2 - \omega_p^2}{2\omega^2 - \omega_p^2}} \tag{A.53}$$

The latter equation is known as the dispersion relation , a plot of (w/w_p) versus $beta_z$ is shown on figure A.3.

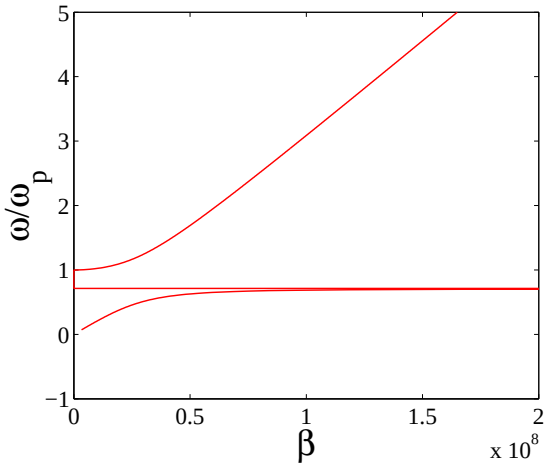

Figure A.3: Despersion of surface plasmons at an interface between a metal and a dielectric.

Appendix B

Validation of Wave guiding and Overlap Results

B.1 Validation of Wave-guiding Results for some Au and Al Structures

Table B.1: Real part of effective index $Re(n_{eff})$ and mode power attenuation (α) versus stripe thickness (t) for the the first order mode as_b^0 at $\lambda_0 = 1310nm$. Comparison of results produced by Naema and Akbari [5].

Metal type/Metal thickness t (nm)	Akbari		Naema	
	$Re(n_{eff})$	α (dB/µm)	$Re(n_{eff})$	α (dB/µm)
Al/100nm	3.626	1.04	3.626	1.036
Au/100nm	3.778	1.265	3.777	1.260
Al/20nm	3.75	1.9	3.666	1.875
Au/20nm	4.25	NA	4.108	4.890
Al/10nm	NA	NA	3.937	7.528
Au/10nm	NA	NA	4.828	9.115

Table B.2: Real part of effective index $Re(n_{eff})$ and mode power attenuation (α) versus stripe thickness (t) for the second order mode aa_b^0 at $\lambda_0 = 1310nm$. Comparison of results produced by Naema and Akbari [5].

Metal type/Metal thickness t (nm)	Akbari		Naema	
	$Re(n_{eff})$	α (dB/µm)	$Re(n_{eff})$	α (dB/µm)
Al/100nm	3.619	1.041	3.608	1.049
Au/100nm	3.772	1.228	3.763	1.297
Al/20nm	3.72	2	3.653	2.010
Au/20nm	4.2	5	4.001	3.251
Al/10nm	5.12	23.5	3.866	5.127
Au/10nm	NA	33.5	4.810	9.157

Table B.3: Real part of effective index $Re(n_{eff})$ and mode power attenuation (α) versus stripe thickness (t) for the the third order mode as_b^1 at $\lambda_0 = 1310nm$. Comparison of results produced by Naema and Akbari [5].

Metal type/Metal thickness t (nm)	Akbari		Naema	
	$Re(n_{eff})$	α (dB/µm)	$Re(n_{eff})$	α (dB/µm)
Al/100nm	3.607	1.056	3.570	1.068
Au/100nm	3.763	1.314	3.728	1.332
Al/20nm	3.69	2.4	3.619	2.054
Au/20nm	4.1	3.8	3.976	3.301
Al/10nm	4.512	16.5	3.840	5.226
Au/10nm	NA	23.4	4.772	9.241

B.2 Validation of Overlap Results for some Au Waveguides

Table B.4: Theoretical attenuations and overlap factors (magnitude | C |, per facet) for some Au waveguides at $\lambda_0 = 1550nm$. Comparison between results produced by Naema and Berini et.al [47].

t (nm)	W (µm)	Naema			Berini et.al	
		$Re(n_{eff})$	Theor. Overlap factor	Theor. MPA (dB/mm)	Theor. Overlap factor	Theor. MPA (dB/mm)
25	8	1.447 413	0.9627	2.128	0.96	2.14
	4	1.446 218	0.9538	1.20	0.96	1.23
31	8	1.448 499	0.9377	4.196	0.94	4.20
	4	1.446 889	0.9571	2.78	0.96	2.81

B.3 Validation of coupling efficiency as a function of wavelength

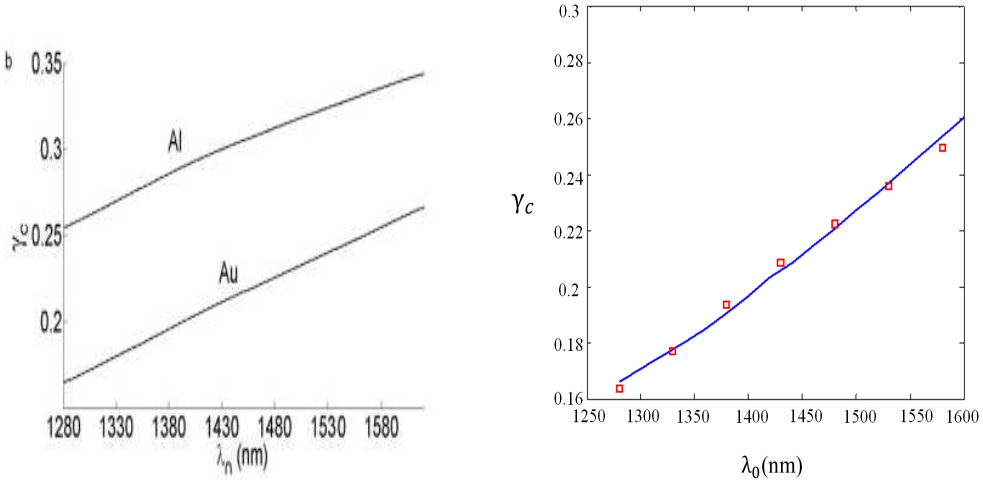

(a) (b)

Figure B.1: Theoretical coupling efficiencies γ_c of the tapered PM optical fibre to the as_b^0 mode for an Au stripe on $n-Si$ over the wavelength range ($1280nm - 1620nm$). B.1a is a previously produced result which was published in [34]. B.1b is a reproduction of the result for Au, the new calculations(blue curve) are plotted along with an estimation of the previous calculations (red curve).

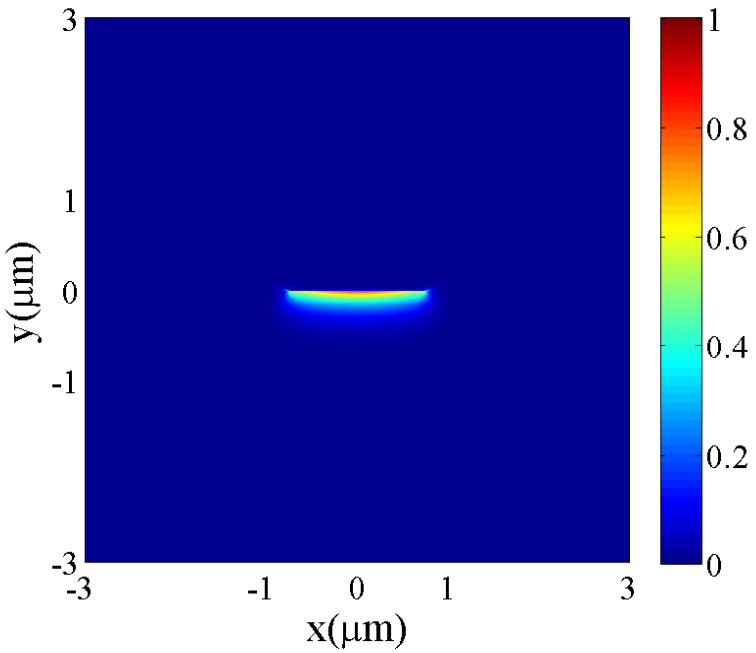

Figure B.2: Field distribution for as_b^0 mode supported by Au metal film of $135nm$ thickness and $1.5\mu m$ width surrounded by air on top and silicon at the bottom at $1310nm$ wavelength.This structure was first simulated by P.Berini et.al ref [36]

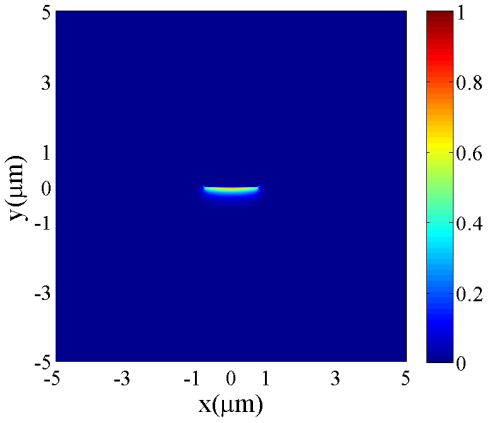

(a)

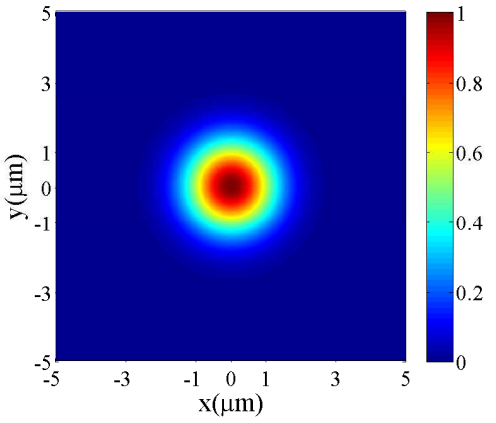

(b)

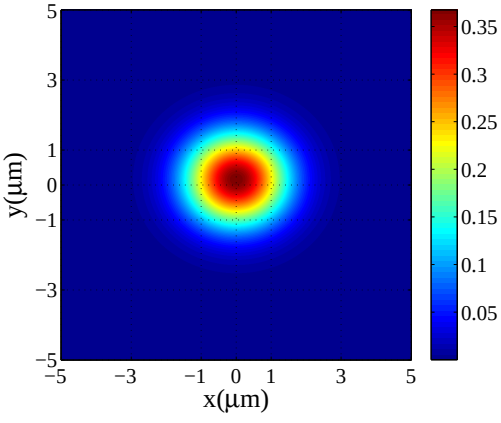

(c)

Figure B.3: (a) the transverse field distribution (E_y) for as_b^0 mode supported by Au metal film of $135nm$ thickness and $1.5\mu m$ width surrounded by air on top and Si at the bottom at $\lambda_0 = 1310nm$.(b) the transverse field distribution (E_y) for an optical fiber having waist radius $(w_0) = 1.3\mu m$.(c) the result of the overlap between the as_b^0 SPP mode and the fiber mode shown on (a) and (b) , respectively. This figure is a validation of one of the overlap results presented in ref [36]

Appendix C

The Dirac delta Function

The expression Dirac delta function, known also as the "unit impulse" function [72] or the "improper function" [73] , has been widely used in quantum mechanics problems; it also appears naturally in many physical problems [74]. It is often used to describe some physical phenomenon due to its convenient mathematical properties [72].

C.1 Definition

Dirac delta function is a symbol denoted as δ which can be treated as a function for certain specific purposes [74].It can be thought of as the generalization of the Kronecker delta to the case of the continuous variables [74].This function is able to get a precise notation which makes it unique for dealing with quantities involving certain type of infinity [74].The concept of delta function usually mean an infinitely thin and high spike at the origin with the total area under the spike being equal to one [58].The function was first introduced by the theoretical Physicist Paul Dirac.

The Dirac delta function is somehow similar to the Kronecker delta but used in integration instead of discrete summations [75]. The function can be defined as follows [75]

$$\delta(x) = \begin{cases} \infty & x = 0 \\ 0 & x \neq 0 \end{cases} \tag{C.1}$$

such that:

$$\int_{-\infty}^{\infty} \delta(x)\, dx = 1 \tag{C.2}$$

From the mathematical point of view, the Dirac delta function is a generalized function or distribution on the real number line which gives a value only at zero and everywhere else its value is zero and its integral is equal to one over the line. On the other hand, from the Physics point of view , it represents the density of an idealized point mass or point charge. In pure mathematics, $\delta(x)$ can not be considered as an ordinary function because it is too singular and is not a function of x in conventional sense while in mathematical literature, it has been known as a generalized function or distribution such as a probability distribution which is also a measure that assigns a value to a function [74] [72].The name "generalized function" means that the function is meaningful only as a part of an integral expression [76]. A delta function can be written outside of an integral but it produces reliable expectations only if it was used as a part of an integral [76].

Since the dirac delta function is an extended-real function having a value only at a single point, it must have total integral zero .It is more suitable to define it as an "operator" that pulls the value of a function at zero.It can only be considered a function if it was used inside integrals.It can be formally thought of as a "distribution" which is also a measure [77].

The value of the delta function is not finite at $(x = 0)$, thus it can not be considered a function at all but the limit of a sequence of functions [78].Thus, it can be considered a special function with zero width ,infinite height and an area of 1 [72]. For example, as seen on figure C.1,as the width approaches zero and the height approaches infinity which means the area is kept constant and equal to 1, the delta function $\delta(x)$ is obtained [75].

If $f(x)$ is an ordinary function that is not another delta function, then the product $f(x)\delta(x)$ is zero everywhere except where $x = 0$.For simplicity, it is more convenient to assume that $f(x)$ is a continuous function [78].Thus,

$$f(x)\delta(x) = f(0)\delta(x) \tag{C.3}$$

The latter relation represents the most important fact about the delta function. If this relation is put under an integral, then the delta function picks out the value of $f(x)$ at $x = 0$.

$$\int_{-\infty}^{\infty} f(x)\delta(x)\,dx = \int_{-\infty}^{\infty} f(0)\delta(x)\,dx = f(0)\int_{-\infty}^{\infty} \delta(x)\,dx = f(0) \tag{C.4}$$

since

$$\int_{-\infty}^{\infty} \delta(x)\,dx = 1 \tag{C.5}$$

The aforementioned equations concludes that integral of any function multiplied by a $\delta - function$ located about zero is just the value of the function at zero.
Since the delta function is zero for $x \neq 0$, thus, the behaviour of the function at infinity does not have any impact on the value of the integral.

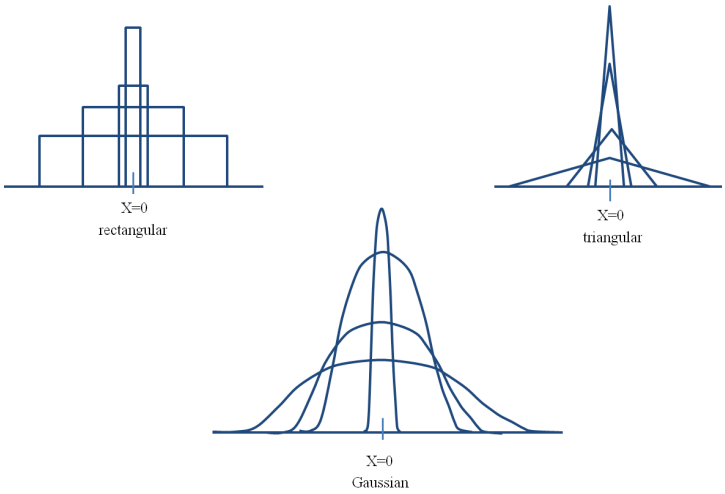

Figure C.1: Geometrical construction of the dirac function as a limit of a sequence of functions.

C.2 Offset of delta function (The shifting property)

In optics, the delta function can be used to describe an idealized point source of light which if real, must have finite width. A point of light that is narrow enough can be approximated with a delta function and thus, its behaviour can be expected using a delta function approximation [72]. If the delta function is displaced, then the point at which the function is not zero will be offset by an amount a such that:

$$\delta(x-a) = \begin{cases} \infty & x = a \\ 0 & x \neq a \end{cases} \tag{C.6}$$

with:

$$\int_{-\infty}^{\infty} \delta(x-a)\, dx = 1 \tag{C.7}$$

Where (a) is any real number [73] and $\delta(x-a)$ is a delta function located at $(x=a)$ as seen on figure C.2.

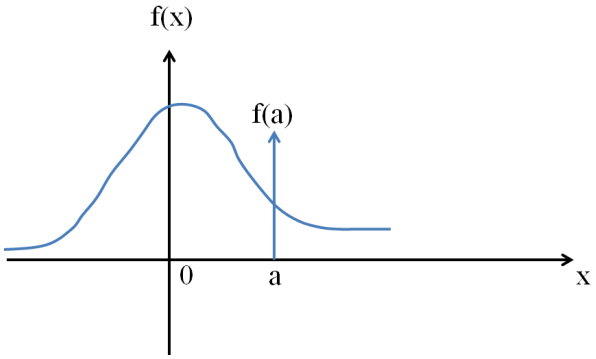

Figure C.2: The shifting property of the delta function.

Then, equation C.3 becomes:

$$f(x)\delta(x-a) = f(a)\delta(x-a) \tag{C.8}$$

Hence, equation C.4 generalizes to [73]:

$$\int_{-\infty}^{\infty} f(x)\delta(x-a)\,dx = f(a) \tag{C.9}$$

The aforementioned relation can be used as an alternate definition of the Dirac delta function and is valid for any function $f(x)$ that is continuous at (a). This relation is known as the shifting property of the Dirac delta function that gives it the sense of a measure.It means that the delta function measures the value of $f(x)$ at the point (a). Any function $\delta(x-a)$ satisfies the shifting property is the Dirac delta function [72].

It is obvious that the limits on the latter integral need only bracket $x = a$ since the product $f(x)\delta(x-a)$ is zero everywhere except at $x = a$. Thus [75]

$$\int_{-1}^{1} f(x)\delta(x)\,dx = f(0) \tag{C.10}$$

If the delta function was in two dimensions, then the property will be somehow similar to the idea of convolution which has several applications in digital image processing and image formation theory [79].Using this approach,equation C.9 will generalize to [79]:

$$\int\int \delta(x-a, y-b)f(x,y)\,dxdy = f(a,b) \tag{C.11}$$

Where $\delta(x-a, y-b)$ is a δ function located at position (a,b).
The latter approach was the one used in this thesis to study and estimate the coupling efficiency between a fiber mode and an SPP mode propagating along a waveguide structure.

C.3 The convolution property of the Dirac delta function

Since the idea of convolution of the Dirac delta function is central to the shifting property in two dimensions which was used this research, it is worth to recall this property.

Convolution of a function $f(x)$ with a delta function at $(x = a)$ is equivalent to shifting the function $f(x)$ by (a).This can be expressed mathematically as follows:

$$f(x) * \delta(x - a) = f(x - a) \tag{C.12}$$

Appendix D

Additional Device performance calculations

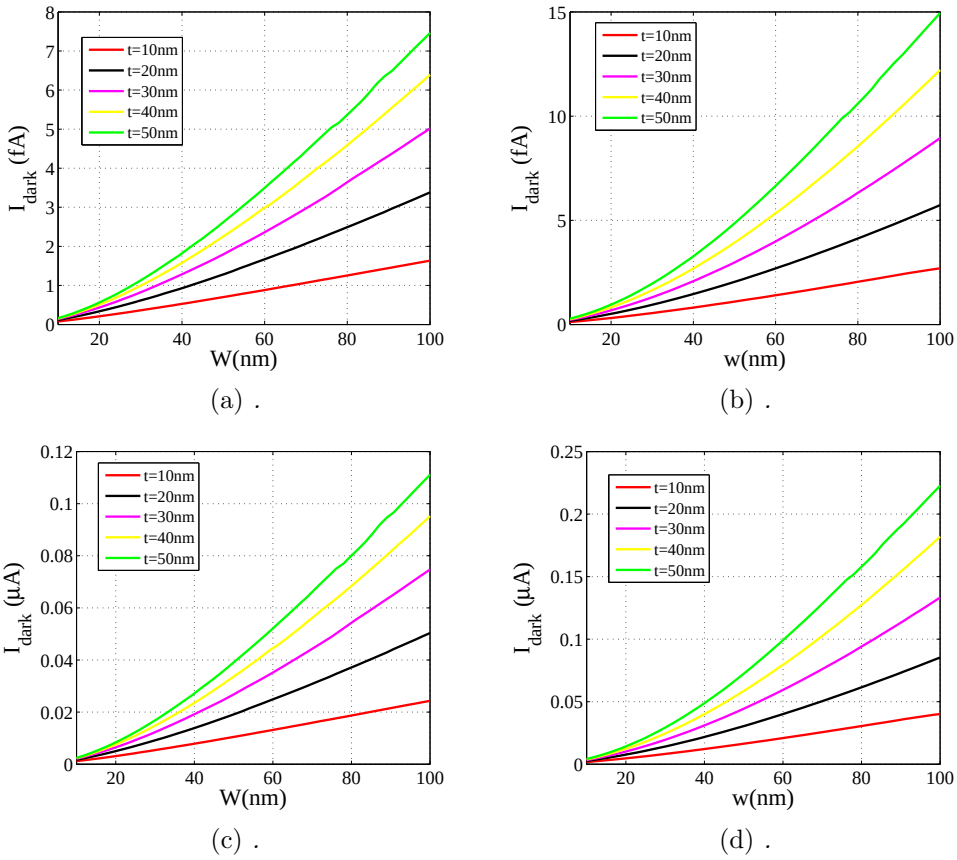

Figure D.1: The dark current as a function of the stripe's width (w) (the waveguide's width) at (a, c) $\lambda_0 = 1310nm$ and (b, d) ($\lambda_0 = 1550nm$) for (a, b) carriers are electrons and (c, d) carriers are holes.

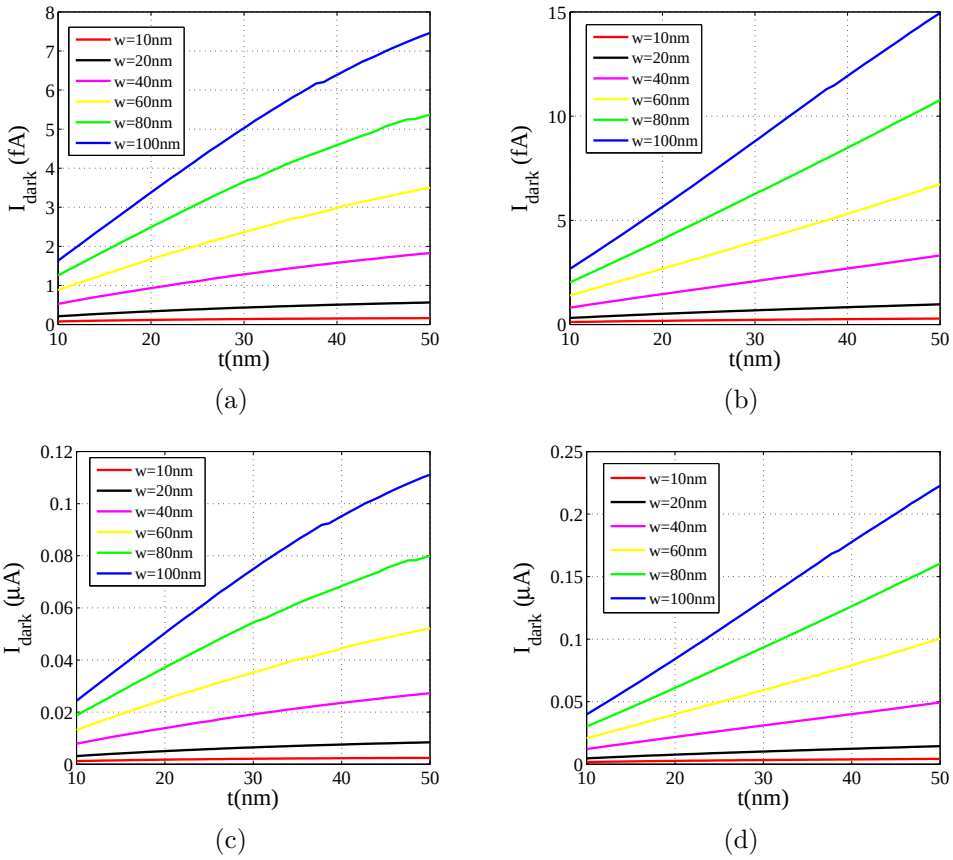

Figure D.2: Dark current ($Idark$) as a function of stripe thickness (t) (the waveguide's thickness) at (a, c) $\lambda_0 = 1310nm$ and (b, d) ($\lambda_0 = 1550nm$) for (a, b) carriers are electrons and (c, d) carriers are holes.

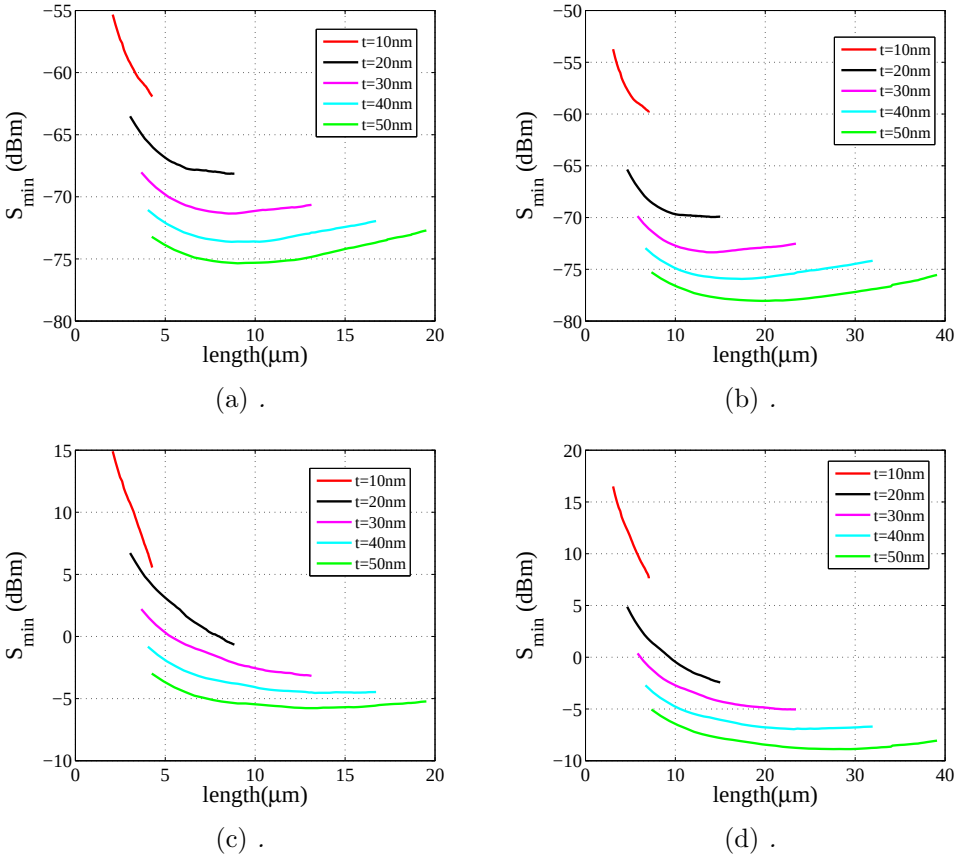

Figure D.3: The minimum detectable power as a function of the stripe's length (l) (the waveguide's length) at (a, c) $\lambda_0 = 1310nm$ and (b, d) ($\lambda_0 = 1550nm$) for (a, b) carriers are electrons and (c, d) carriers are holes.The stripe length was estimated using the effective index data that was acquired as a function of the waveguide's width and which are shown on figure 2.7 at ($\lambda_0 = 1310nm$) and on figure 2.8 at ($\lambda_0 = 1550nm$). The minimum detectable power was calculated using the responsivity data shown on figure 4.8.

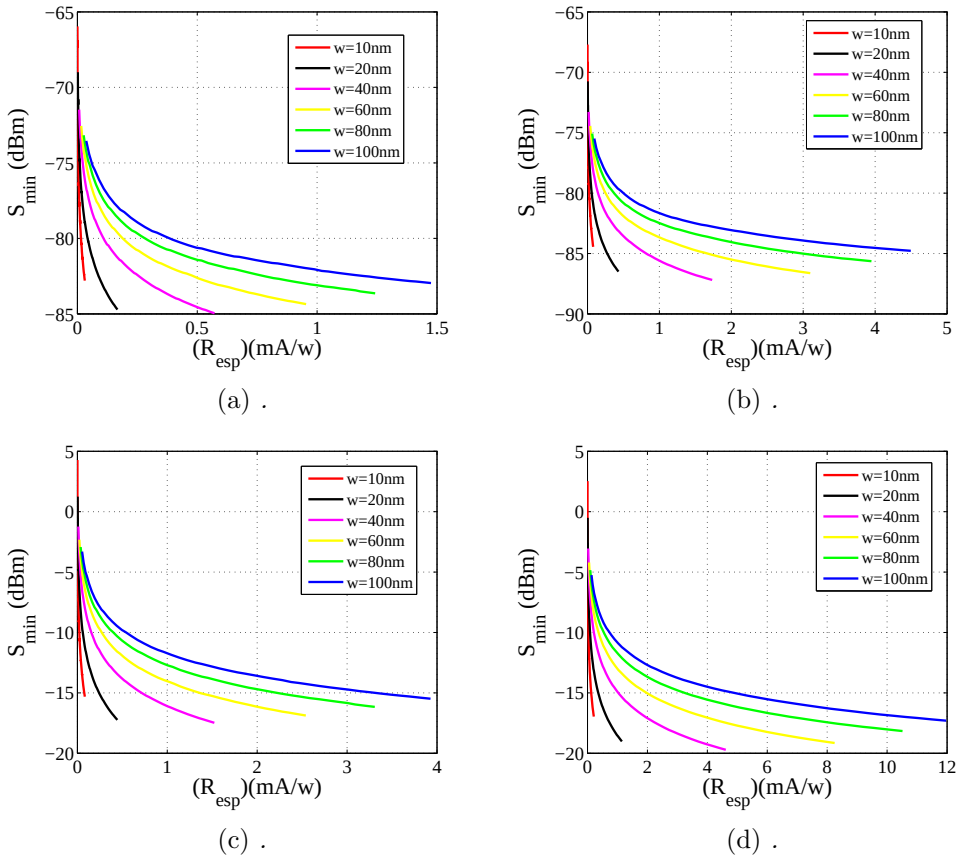

Figure D.4: Minimum detectable power ($Smin$) as a function of the device's responsivity (R) at (a, c) $\lambda_0 = 1310nm$ and (b, d) ($\lambda_0 = 1550nm$) for (a, b) carriers are electrons and (c, d) carriers are holes.The minimum detectable power was acquired from the responsivity data present in figure 4.5.

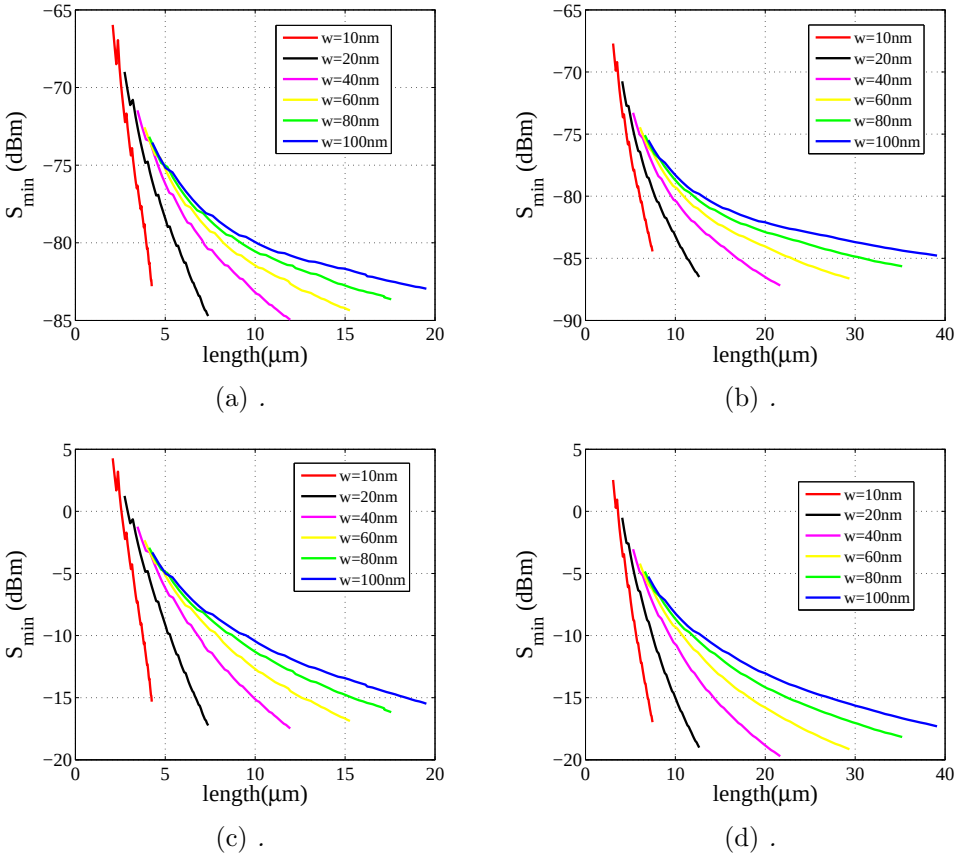

Figure D.5: Minimum detectable power ($Smin$) as a function of stripe length (L) at (a, c) $\lambda_0 = 1310nm$ and (b, d) ($\lambda_0 = 1550nm$) for (a, b) carriers are electrons and (c, d) carriers are holes.The minimum detectable power was acquired from the responsivity data present in figure 4.5.

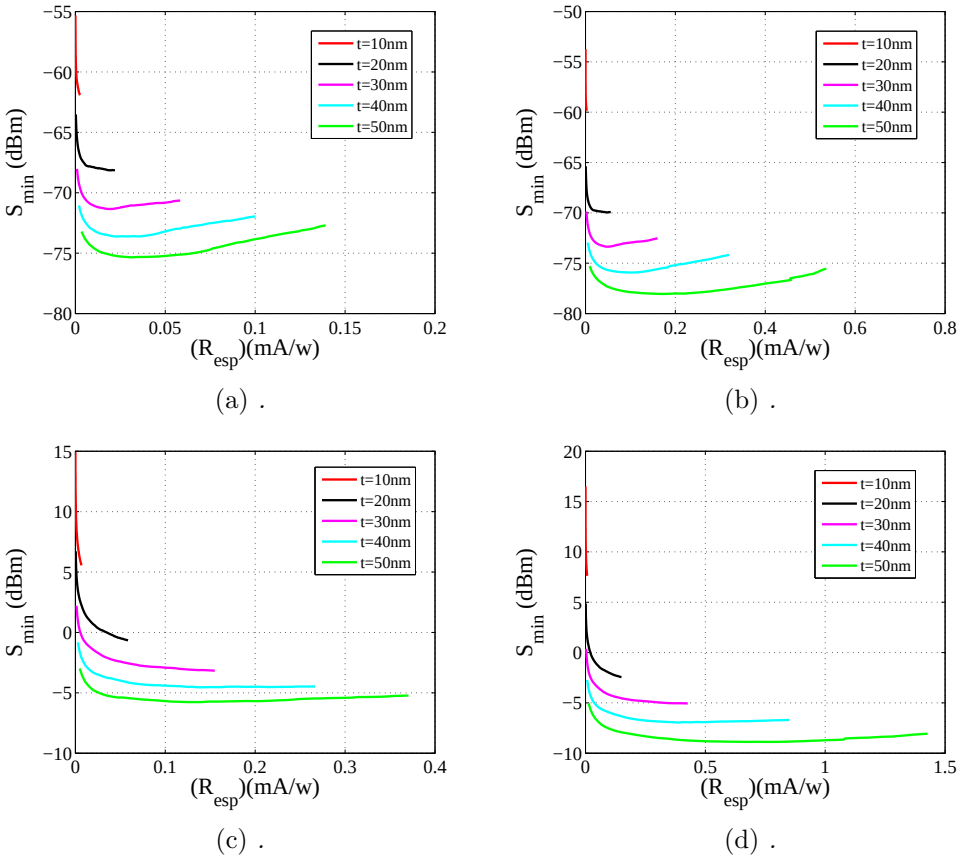

Figure D.6: The minimum detectable power as a function of the device's responsivity at (a, c) $\lambda_0 = 1310nm$ and (b, d) $(\lambda_0 = 1550nm)$ for (a, b) carriers are electrons and (c, d) carriers are holes.The minimum detectable power was acquired using the responsivity data shown on figure 4.8 as a function of stripe width (w) at $(\lambda_0 = 1310nm)$ and $(\lambda_0 = 1550nm)$.And, is plotted against it.

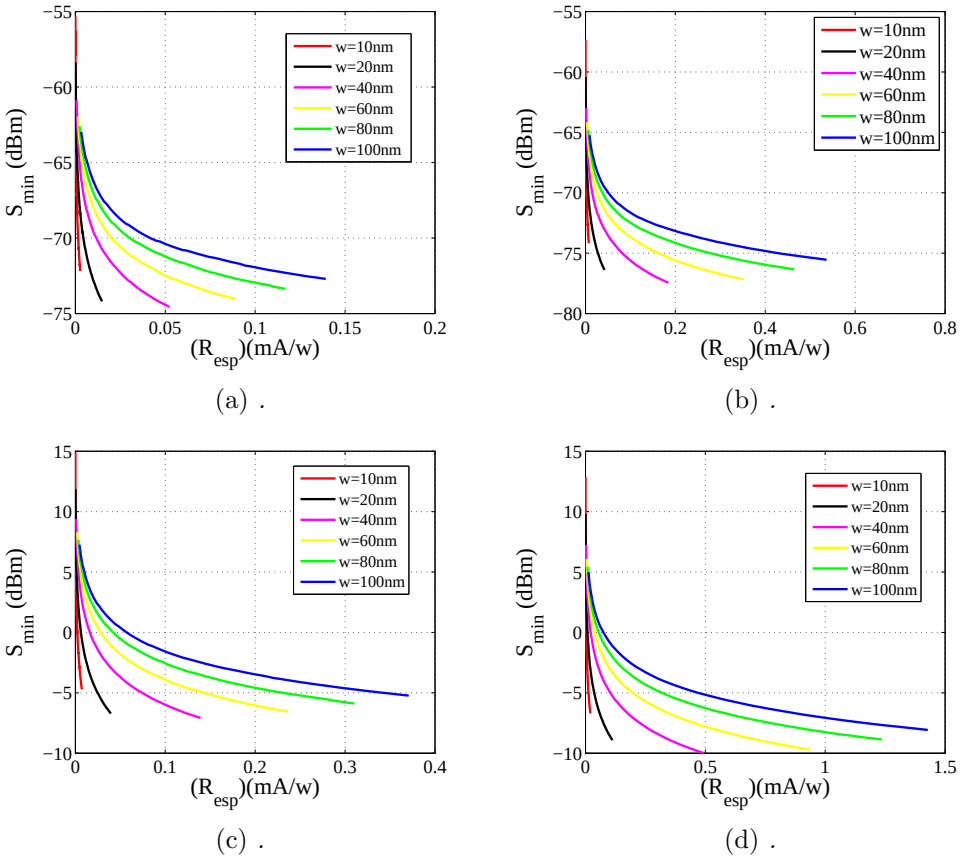

Figure D.7: The minimum detectable power as a function of the device's responsivity at (a, c) $\lambda_0 = 1310nm$ and (b, d) ($\lambda_0 = 1550nm$) for (a, b) carriers are electrons and (c, d) carriers are holes.The minimum detectable power was acquired using the responsivity data shown on figure 4.6 as a function of stripe thickness (t) at $(\lambda_0 = 1310nm)$ and $(\lambda_0 = 1550nm)$.And, is plotted against it.

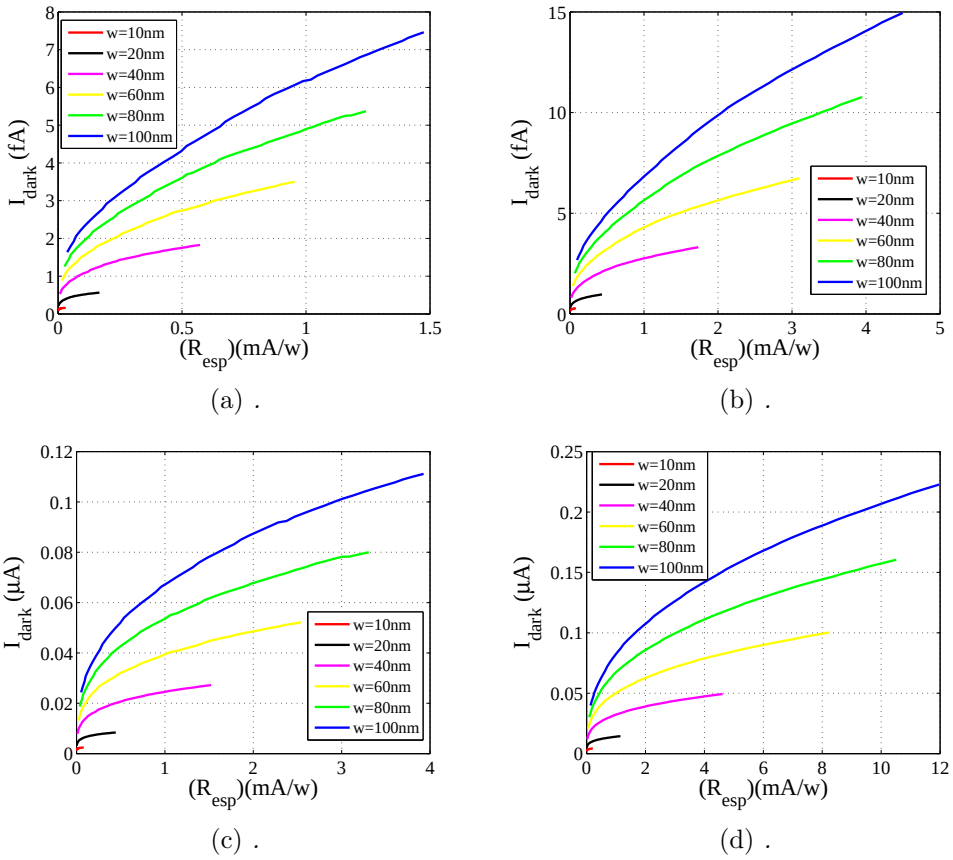

Figure D.8: Dark current ($Idark$) as a function of the device's responsivity (R) at (a, c) $\lambda_0 = 1310nm$ and (b, d) ($\lambda_0 = 1550nm$) for (a, b) carriers are electrons and (c, d) carriers are holes.The responsivity data are present in figure 4.5.

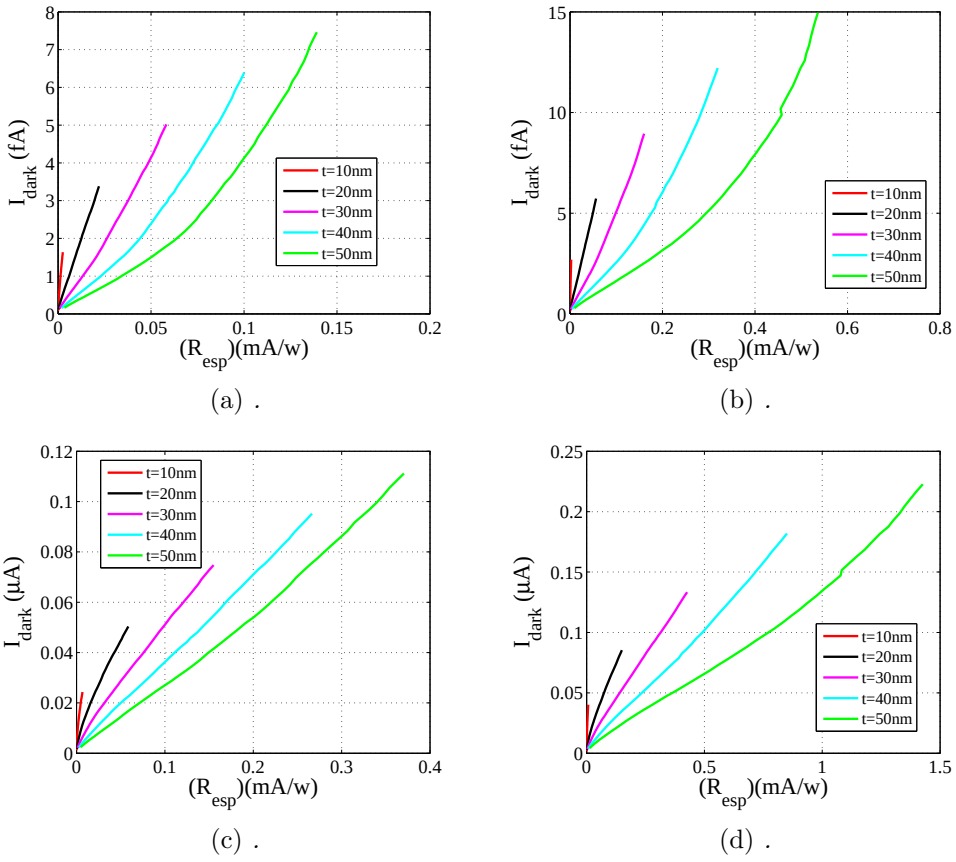

Figure D.9: The dark current ($Idark$) as a function of the device's responsivity at (a, c) $\lambda_0 = 1310nm$ and (b, d) ($\lambda_0 = 1550nm$) for (a, b) carriers are electrons and (c, d) carriers are holes.The responsivity was calculated as a function of stripe width using coupling with a large fiber as seen on figure 4.8 at bothwavelegths ($\lambda_0 = 1310nm$) and ($\lambda_0 = 1550nm$).

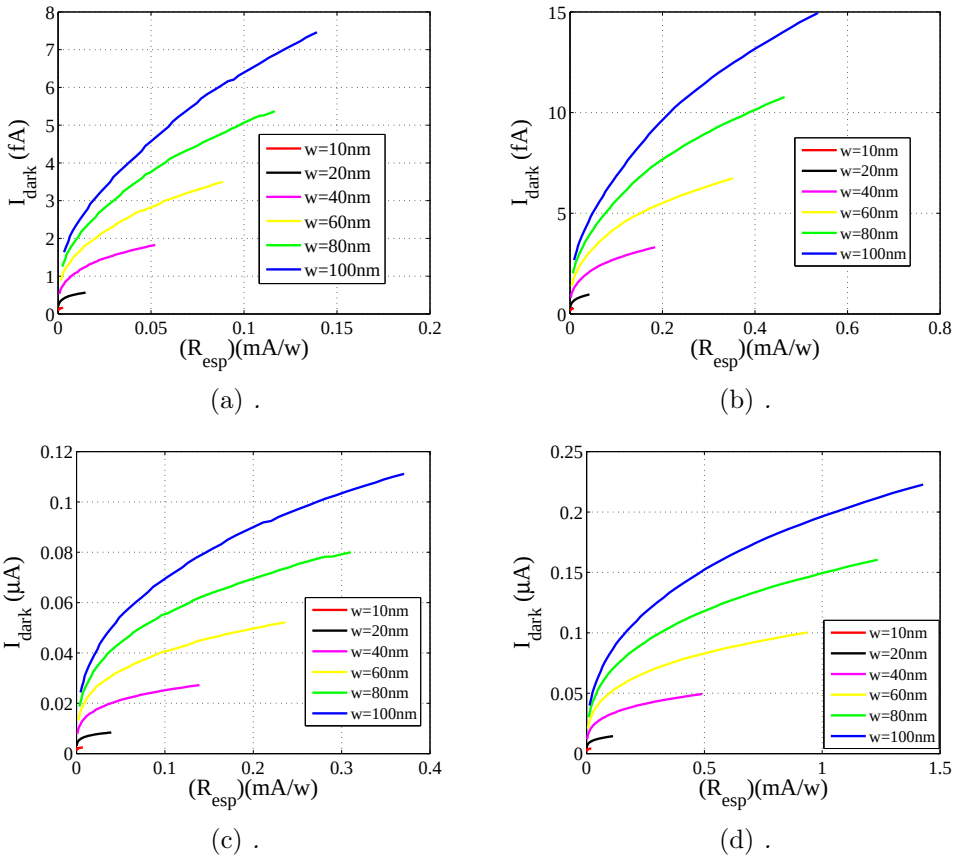

Figure D.10: Dark current ($Idark$) as a function of the device's responsivity (R) at (a, c) $\lambda_0 = 1310nm$ and (b, d) ($\lambda_0 = 1550nm$) for (a, b) carriers are electrons and (c, d) carriers are holes.sweep thickness with big fiber coupling.

Appendix E

Glossary of Terms

SPP_S **Surface Plasmon Polaritons**

$SRSPP_S$ **Short Range Surface Plasmon Polaritons**

$LRSPP_S$ **Long Range Surface Plasmon Polaritons**

η_e **External Quantum Efficiency**

η_i **Internal Quantum Efficiency**

I_{dark} **Dark Current**

S_{min} **Minimum detectable power**

R_{esp} **Responsivity**

γ_c **Coupling Efficiency**

L_e **Attenuation Length for electron carriers**

L_h **Attenuation length for hole carriers**

ϕ_B **The Schottky barrier height**

MPA **Mode Power Attenuation**

FEM **Finite Element Method**

TM **Transverse Magnetic**

TE **Transverse Electric**

IPE **Internal Photo-emission**

EHP **Electron Hole Pairs**

$PM - SMF$ **Polarization-maintaining single mode fiber**

IMI **Insulator-Metal-Insulator**

MIM **Metal-Insulator-Metal**

MSM **Metal-Semiconductor-Metal**

SOI **Silicon on Insulator**

SBH **Schottky Barrier Height**

CNT **Carbon Nano-tube**

PDs **Photo-detectors**

Bibliography

[1] Hyeunseok Choi, David F. Pile, Sunghyun Nam, Guy Bartal, and Xiang Zhang. Compressing surface plasmons for nano-scale optical focusing. *Opt. Express*, 17(9):7519–7524, Apr 2009.

[2] B. Steinberger, A. Hohenau, H. Ditlbacher, A. L. Stepanov, A. Drezet, F. R. Aussenegg, A. Leitner, and J. R. Krenn. Dielectric stripes on gold as surface plasmon waveguides. *Applied Physics Letters*, 88(9):–, 2006.

[3] Ewold Verhagen, Albert Polman, and L. (Kobus) Kuipers. Nanofocusing in laterally tapered plasmonic waveguides. *Opt. Express*, 16(1):45–57, Jan 2008.

[4] Pierre Berini. Surface plasmon photodetectors and their applications. *Laser Photonics Reviews*, 8(2):197–220, 2014.

[5] Ali Akbari. Waveguide integrated surface plasmon photodetector:design,fabrication, and measurment. Master's thesis, University Of Ottawa, 2010.

[6] Mads L. Trolle and Thomas G. Pedersen. Indirect optical absorption in silicon via thin-film surface plasmon. *Journal of Applied Physics*, 112(4):–, 2012.

[7] William L. Barnes, Alain Dereux, and Thomas W Ebbesen. Surface plasmon subwavelength optics. *Nature*, 2003.

[8] Thomas Nikolajsen, Kristjan Leosson, Ildar Salakhutdinov, and S.I. Bozhevolnyi. Polymer-based surface-plasmon-polariton stripe waveguides at telecommunication wavelengths. *Applied Physics Letters*, 82(5):668–670, 2003.

[9] Pierre Berini. Plasmon-polariton waves guided by thin lossy metal films of finite width: Bound modes of symmetric structures. *Phys. Rev. B*, 61:10484–10503, Apr 2000.

[10] R. Gordon. Surface plasmon nanophotonics: A tutorial. *Nanotechnology Magazine, IEEE*, 2(3):12–18, 2008.

[11] Pierre Berini. Plasmon-polariton waves guided by thin lossy metal films of finite width: Bound modes of asymmetric structures. *Phys. Rev. B*, 63:125417, Mar 2001.

[12] Robert Charbonneau, Pierre Berini, Ezio Berolo, and Ewa Lisicka-Shrzek. Experimental observation of plasmon polariton waves supported by a thin metal film of finite width. *Opt. Lett.*, 25(11):844–846, Jun 2000.

[13] Pierre Berini, editor. *Surface plasmon photodetectors*, volume 8771, 2013.

[14] Leilei Yin, Vitali K. Vlasko-Vlasov, John Pearson, Jon M. Hiller, Jiong Hua, Ulrich Welp, Dennis E. Brown, and Clyde W. Kimball. Subwavelength focusing and guiding of surface plasmons. *Nano Letters*, 5(7):1399–1402, 2005. PMID: 16178246.

[15] J.-C. Weeber, J. R. Krenn, A. Dereux, B. Lamprecht, Y. Lacroute, and J. P. Goudonnet. Near-field observation of surface plasmon polariton propagation on thin metal stripes. *Phys. Rev. B*, 64:045411, Jul 2001.

[16] Hocheol Shin and Shanhui Fan. All-angle negative refraction for surface plasmon waves using a metal-dielectric-metal structure. *Phys. Rev. Lett.*, 96:073907, Feb 2006.

[17] A.Bruce Buckman. *Guided-Wave Photonics*. A Harcourt Brace Jovanovich College Publisher, 1992.

[18] Ali Akbari and Pierre Berini. Schottky contact surface-plasmon detector integrated with an asymmetric metal stripe waveguide. *Applied Physics Letters*, 95(2):021104–021104–3, 2009.

[19] C. Scales and Pierre Berini. Thin-film schottky barrier photodetector models. *Quantum Electronics, IEEE Journal of*, 46(5):633–643, 2010.

[20] I. G.Breukelaar. Surface plasmon-polaritons in thin metal stripes and slabs: Waveguiding and mode cutoff. Master's thesis, University Of Ottawa, 2004.

[21] Ben G.Streetman and Sanjay Kumar Banerjee. *Solid State Electronic Devices*. Pearson Prentice Hall, 2006.

[22] Tsutomu Ishi, Junichi Fujikata, Kikuo Makita, Toshio Baba, and Keishi Ohashi. Si nano-photodiode with a surface plasmon antenna. *Japanese Journal of Applied Physics*, 44(12):L364–L366, 2005.

[23] C.Genet and T.W.Ebbesen. Light in tiny holes. *Nature*, 2007.

[24] Chi-Yang Chang, Hsu-Yu Chang, Chia-Yi Chen, Ming-Wei Tsai, Yi-Tsung Chang, Si-Chen Lee, and Shiang-Feng Tang. Wavelength selective quantum dot infrared photodetector with periodic metal hole arrays. *Applied Physics Letters*, 91(16):163107–163107–3, 2007.

[25] Jessie Rosenberg, Rajeev V. Shenoi, Thomas E. Vandervelde, Sanjay Krishna, and Oskar Painter. A multispectral and polarization-selective surface-plasmon resonant midinfrared detector. *Applied Physics Letters*, 95(16):–, 2009.

[26] Zongfu Yu, Georgios Veronis, Shanhui Fan, and Mark L. Brongersma. Design of midinfrared photodetectors enhanced by surface plasmons on grating structures. *Applied Physics Letters*, 89(15):–, 2006.

[27] K. Lance Kelly, Eduardo Coronado, Lin Lin Zhao, and George C. Schatz. The optical properties of metal nanoparticles: the influence of size, shape, and dielectric environment. *The Journal of Physical Chemistry B*, 107(3):668–677, 2003.

[28] Howard R. Stuart and Dennis G. Hall. Island size effects in nanoparticle-enhanced photodetectors. *Applied Physics Letters*, 73(26):3815–3817, 1998.

[29] M. Jestl, I. Maran, A. Köck, W. Beinstingl, and E. Gornik. Polarization-sensitive surface plasmon schottky detectors. *Opt. Lett.*, 14(14):719–721, Jul 1989.

[30] S. R. J. Brueck, V. Diadiuk, T. Jones, and W. Lenth. Enhanced quantum efficiency internal photoemission detectors by grating coupling to surface plasma waves. *Applied Physics Letters*, 46(10):915–917, 1985.

[31] Mohammad Alavirad, Saba Siadat Mousavi, Langis Roy, and Pierre Berini. Schottky-contact plasmonic dipole rectenna concept for biosensing. *Opt. Express*, 21(4):4328–4347, Feb 2013.

[32] Iwijn De Vlaminck, Pol Van Dorpe, Liesbet Lagae, and Gustaaf Borghs. Local electrical detection of single nanoparticle plasmon resonance. *Nano Letters*, 7(3):703–706, 2007. PMID: 17315938.

[33] Salman Latif Ali K. Okyay Dany-Sebastien Ly-Gagnon Krishna C. Saraswat David A. B. Miller Liang Tang, Sukru Ekin Kocabas. Nanometre-scale germanium photodetector enhanced by a near-infrared dipole antenna. *Nature Photonics*, 2008.

[34] Ali Akbari, R. Niall Tait, and Pierre Berini. Surface plasmon waveguide schottky detector. *Opt. Express*, 18(8):8505–8514, Apr 2010.

[35] Anthony Olivieri, Ali Akbari, and Pierre Berini. Surface plasmon waveguide schottky detectors operating near breakdown. *physica status solidi (RRL) Rapid Research Letters*, 4(10):283–285, 2010.

[36] Pierre Berini, Anthony Olivieri, and Chengkun Chen. Thin au surface plasmon waveguide schottky detectors on p-si. *Nanotechnology*, 23(44):444011, 2012.

[37] A Akbari, A Olivieri, and P. Berini. Subbandgap asymmetric surface plasmon waveguide schottky detectors on silicon. *Selected Topics in Quantum Electronics, IEEE Journal of*, 19(3):4600209–4600209, May 2013.

[38] Christine Scales, Ian Breukelaar, Robert Charbonneau, and Pierre Berini. Infrared performance of symmetric surface-plasmon waveguide schottky detectors in si. *J. Lightwave Technol.*, 29(12):1852–1860, Jun 2011.

[39] Christine Scales, Ian Breukelaar, and Pierre Berini. Surface-plasmon schottky contact detector based on a symmetric metal stripe in silicon. *Opt. Lett.*, 35(4):529–531, Feb 2010.

[40] Pieter Neutens. Electrical detection of confined gap plasmons in metal insulator metal waveguides. *Nature Photonics*, 2009.

[41] H. Ditlbacher, F. R. Aussenegg, J. R. Krenn, B. Lamprecht, G. Jakopic, and G. Leising. Organic diodes as monolithically integrated surface plasmon polariton detectors. *Applied Physics Letters*, 89(16):–, 2006.

[42] Shiyang Zhu, G.Q. Lo, and D.L. Kwong. Low-cost and high-speed soi waveguide-based silicide schottky-barrier msm photodetectors for broadband optical communications. *Photonics Technology Letters, IEEE*, 20(16):1396–1398, Aug 2008.

[43] Yanbin An, Ashkan Behnam, Eric Pop, and Ant Ural. Metal-semiconductor-metal photodetectors based on graphene/p-type silicon schottky junctions. *Applied Physics Letters*, 102(1):–, 2013.

[44] C. Scales, I. Breukelaar, R. Charbonneau, and Pierre Berini. Infrared performance of symmetric surface-plasmon waveguide schottky detectors in si. *Lightwave Technology, Journal of*, 29(12):1852–1860, June 2011.

[45] Robert Charbonneau, Nancy Lahoud, Greg Mattiussi, and Pierre Berini. Demonstration of integrated optics elements based on long-ranging surface plasmon polaritons. *Opt. Express*, 13(3):977–984, Feb 2005.

[46] Stefan A.Maier. *Plasmonics: Fundamentals and Applications*. Springer Science+Business Media LLC, 2007.

[47] P. Berini, R. Charbonneau, N. Lahoud, and G. Mattiussi. Characterization of long-range surface-plasmon-polariton waveguides. *Journal of Applied Physics*, 98(4):–, 2005.

[48] R. Buckley and Pierre Berini. Radiation suppressing metallo-dielectric optical waveguides. *Lightwave Technology, Journal of*, 27(14):2800–2808, July 2009.

[49] Pierre Berini. Plasmon-polariton modes guided by a metal film of finite width bounded by different dielectrics. *Opt. Express*, 7(10):329–335, Nov 2000.

[50] Pierre Berini. Plasmon polariton modes guided by a metal film of finite width. *Opt. Lett.*, 24(15):1011–1013, Aug 1999.

[51] Pierre Berini, Robert Charbonneau, and Nancy Lahoud. Long-range surface plasmons on ultrathin membranes. *Nano Letters*, 7(5):1376–1380, 2007. PMID: 17430008.

[52] Robert Charbonneau, Christine Scales, Ian Breukelaar, Simon Fafard, Nancy Lahoud, Greg Mattiussi, and Pierre Berini. Passive integrated optics elements based on long-range surface plasmon polaritons. *J. Lightwave Technol.*, 24(1):477, Jan 2006.

[53] Kholoud Khalid Gazzaz. Biosensing performance of surface plasmon polariton bragg gratings. Master's thesis, University of Ottawa, 2014.

[54] In Edward D. Palik, editor, *Handbook of Optical Constants of Solids*. Academic Press, Orlando,USA, 1985.

[55] Comsol multiphysics. `http://www.comsol.com/`. Accessed: 2013-09-30.

[56] Robin Buckley. Figures of merit and modelling of metallo-dielectric waveguides. Master's thesis, University Of Ottawa, 2008.

[57] Noemi Petra and Matthias K. Gobbert. Performance studies with comsol multiphysics via scripting and batch processing.

[58] Wikipedia. Plagiarism — Wikipedia, the free encyclopedia, 2004. [Online; accessed 22-July-2004].

[59] Walter F. Kosonocky, F.V. Shallcross, T.S. Villani, and J.V. Groppe. 160x244 element ptsi schottky-barrier ir-ccd image sensor. *Electron Devices, IEEE Transactions on*, 32(8):1564–1573, Aug 1985.

[60] M. Casalino, L. Sirleto, L. Moretti, M. Gioffr, G. Coppola, and Ivo Rendina. Silicon resonant cavity enhanced photodetector based on the internal photoemission effect at 1.55m: Fabrication and characterization. *Applied Physics Letters*, 92(25):–, 2008.

[61] Shiyang Zhu, M. B. Yu, G. Q. Lo, and D. L. Kwong. Near-infrared waveguide-based nickel silicide schottky-barrier photodetector for optical communications. *Applied Physics Letters*, 92(8):–, 2008.

[62] M. Casalino, L. Sirleto, M. Iodice, N. Saffioti, M. Gioffr, I. Rendina, and G. Coppola. Cu/p-si schottky barrier-based near infrared photodetector integrated with a silicon-on-insulator waveguide. *Applied Physics Letters*, 96(24):–, 2010.

[63] S. R. J. Brueck, V. Diadiuk, T. Jones, and W. Lenth. Enhanced quantum efficiency internal photoemission detectors by grating coupling to surface plasma waves. *Applied Physics Letters*, 46(10):915–917, 1985.

[64] K. M. Torosian, A. S. Karakashian, and Y. Y. Teng. Surface plasma-enhanced internal photoemission in gallium arsenide schottky diodes. *Appl. Opt.*, 26(13):2650–2652, Jul 1987.

[65] C. Daboo, M.J. Baird, H.P. Hughes, N. Apsley, and M.T. Emeny. Improved surface plasmon enhanced photodetection at an au-gaas schottky junction using a novel molecular beam epitaxy grown otto coupling structure. *Thin Solid Films*, 201(1):9 – 27, 1991.

[66] Raymond T. Tung. The physics and chemistry of the schottky barrier height. *Applied Physics Reviews*, 1(1):–, 2014.

[67] R. H. Fowler. The analysis of photoelectric sensitivity curves for clean metals at various temperatures. *Phys. Rev.*, 38:45–56, Jul 1931.

[68] Yanbin An, Hemant Rao, Gijs Bosman, and Ant Ural. Characterization of carbon nanotube film-silicon schottky barrier photodetectors. *Journal of Vacuum Science and Technology B*, 30(2):–, 2012.

[69] M. Casalino, L. Sirleto, L. Moretti, M. Gioffr, G. Coppola, and Ivo Rendina. Silicon resonant cavity enhanced photodetector based on the internal photoemission effect at 1.55m: Fabrication and characterization. *Applied Physics Letters*, 92(25):–, 2008.

[70] C.K. Chen, B. Nechay, and B-Y Tsaur. Ultraviolet, visible, and infrared response of ptsi schottky-barrier detectors operated in the front-illuminated mode. *Electron Devices, IEEE Transactions on*, 38(5):1094–1103, May 1991.

[71] C.A. Scales and P.S.J. Berini. Schottky barrier photodetectors, Apr 2006. US Patent 7,026,701.

[72] Chris A Mack. *Fundamental Principles of Optical Lithography*. Wiley, 2007.

[73] *The Principles of Quantum Mechanics*. Oxford University Press, 1958.

[74] Jai Kumar Singhal. Why did dirac need delta function.

[75] J.H.Davis. Physics 2460 electricity and magnetism, Fall 2007.

[76] A.I.Lvovsky. Quantum mechanics i.

[77] Hitoshi Murayama. Dirac delta function. Technical report, American Academy of Arts and Sciences, 2001.

[78] David J Griffiths. *Introduction to Electrodynamics*. Prentice-Hall,Inc, 1999.

[79] John A. Peacock. Fourier analysis, 2014.